

Quasilinear Algorithm for Elastodynamic Boundary Integral Equation Method

Dye SK Sato · Ryosuke Ando

Received: date / Accepted: date

Abstract We present a fast algorithm with small memory storage to compute the spatiotemporal boundary integral equation method (ST-BIEM) particularly for the elastodynamic problem. The time complexity of the spatiotemporal convolution and memory consumption to store the integral kernel and convolved variables are originally of $O(N^2M)$ in ST-BIEM for a given number of discretized fault elements N and time steps M . Such huge costs of ST-BIEM are reduced to be of $O(N \log N)$ by our methods, called the fast domain partitioning hierarchical matrices (FDP=H-matrices). FDP=H-matrices are natural extensions of previously proposed two fast algorithms, the fast domain partitioning method (FDPM) and the hierarchical matrices (H-matrices), and are further combined with newly developed two algorithms. After developing new methods, we test the cost and accuracy of FDP=H-matrices both analytically and numerically.

Keywords boundary element · numerical methods · dynamic · elasticity · rupture

1 Introduction

The boundary integral equation method (BIEM) is a versatile method for solving partial differential equations [4, 5]. Examples can be seen in the various research fields such as the electromagnetic modeling [6], heat conductive problems [7], acoustic holography [8], and fracture mechanics [9, 10, 11, 12]. BIEM simplifies the posed problems of the entire spatial volumes into integral equations of the bound-

aries governed by the given boundary conditions. This dimensional reduction helps BIEM to reduce the number of elements [13], numerical dispersions [14], and the spatial discretization errors for handling complex objects [12]. Analytically obtained discretized expressions of the given integral kernel (hereafter called the kernel) also contribute to the accuracy of BIEM [15].

A large issue of BIEM is its numerical cost [13] measured by the memory consumption and time complexity (computation time taken to run a BIEM simulation). They are respectively quantified by the *total* memory consumption to store the kernel and other variables (called the memory cost) and the time (the time complexity) to compute the convolution of the integral equation *once* (called the computation cost). Both the memory and computation costs are of $O(N^2)$ in the original spatial BIEM solving static problems for the given number of elements N . Both are of $O(N^2M)$ in the original spatiotemporal BIEM (ST-BIEM) solving dynamic problems [2] for given N and the number of time steps M . These costs of BIEM are in contrast to memory and computation costs of volume based methods, e.g., the finite difference method and finite element method, being of $O(N_v)$ in both static and dynamic problems, where N_v denotes the number of elements in the volume-based methods. The original BIEM requires greatly larger numerical costs than those of volume-based methods as N and M increase, despite a relation $N_v \gg N$ ascribable to the dimensional reduction of the discretized objects in BIEM.

Note that the computation cost defined earlier does not consider the repetition of the convolution, to reduce the cost concerning which is out of the scope in this study. For example, the time complexity to wholly simulate a dynamic problem is of $O(N_vM)$ in volume-based methods and of $O(N^2M^2)$ in ST-BIEM [2]. The increase of the computation cost due to the repetition in ST-BIEM is simply represented just by multiplying the factor M , and not reducible.

Daisuke Sato
DPRI, Kyoto University, Gokasho, Uji, Kyoto, 6110011 Japan
E-mail: sato.daisuke.6r@kyoto-u.ac.jp

Ryosuke Ando
University of Tokyo, Science Building 1, 7-3-1 Hongo, Bunkyo-ku,
Tokyo 113-0033

Fast and efficient algorithms to resolve such cost problems are well established in spatial BIEM cases, where the memory and computation costs become of almost $O(N)$. Hereafter, the logarithmic factor is described by “almost” for the order evaluation to highlight the dominant factor in this paper. For example, the orthogonal transformation, like the Fourier transform [16, 17] achieves almost $O(N)$ costs in the case of special geometries such as a planar boundary. For more general geometries, the fast multipole method (FMM) [18] and hierarchical matrices (H-matrices, (detailed in §2.2)) [3] can reduce the memory and computation costs to be of almost $O(N)$. Although FMM and H-matrices impose certain approximations, involved errors are normally quite small, since FMM and H-matrices utilize the attenuating natures of kernels proportional to the powers of the source-receiver distance [13, 19]. Moreover, while FMM requires analytic expressions for expanding the kernels, which can be often complicated, H-matrices are easily applicable even to complicated formed kernels by using the purely numerical low-rank approximation, typified by the adaptive cross approximation (ACA) [20].

On the other hand, the cost problem in ST-BIEM is largely unsolved particularly in the transient elastodynamic problems. While FMM-based methods (of both time- and frequency-domains) achieve almost $O(N)$ computation costs (and almost $O(NM)$ time complexities to run the whole simulation) in problems of simple wave equations [21, 22], it is difficult to apply FMM to the complicated formed kernel [19]. For example, the three dimensional elastodynamic kernel comprises dozens of terms [23], to which FMM is still not applied as far as we know. Additionally, FMM-based methods already proposed require the almost $O(NM)$ memory cost [22] to store temporal history of the variables on boundaries.

The cost increase in ST-BIEM is more serious in H-matrices than in FMM. H-matrices require $O(N^2)$ costs due to the difficulty in the low-rank approximation across the impulsive wave front, which contains the singularity as well as the location of the sources [13]. Such cost increase is resulted from the nature of H-matrices that the memory and computation costs are bounded by the number of the discretized kernel components enclosing the singular points of the continuous kernel [19], which amounts to $O(N^2)$ in elastodynamic ST-BIEM [24].

The singularity along the wavefronts has been considered to inevitably lead the difficulty of H-matrices in applying to the hyperbolic partial differential equations, including wave equations involving propagating wave fronts [19]. However, the way to solve it is lightened recently, by the fast domain partitioning method (FDPM) [1, 2] (detailed in §2.3). FDPM is a fast algorithm for ST-BIEM based on the physical properties of the kernel, dividing the time domain of the elastodynamic kernel into three physical domains:

Domain F corresponding to the P and S wavefronts, Domain I in-between P and S waves, and Domain S of the static equilibrium (Domain S). After the domain partitioning, FDPM computes the convolution faster at lower memory by analytically separating the elastodynamic kernel into the space-dependent part and the time-dependent part in Domains I and S. Furthermore, Ando [2] showed that the elastodynamic kernel is possibly regularly attenuating, thus expandable, along Domain F, which corresponds to the $O(N^2)$ components containing the singularities. Along this line, the problem of H-matrices is expected to be resolved. In fact, treating singularities at the wavefronts will be a main issue in this study in incorporating the low rank approximation, and we will develop a novel technique for it.

In this paper, we develop almost $O(N)$ methods called the fast domain partitioning hierarchical matrices (FDP=H-matrices), for elastodynamic ST-BIEM reducing memory and computation costs to be of almost $O(N)$ with keeping high accuracy of ST-BIEM. Combining FDPM, H-matrices, and newly developed two algorithms explained later, FDP=H-matrices overcome the previously encountered difficulties in applying H-matrices to the wave equation. The concept combining FDPM and H-matrices detailed in §3 is originally proposed by Ando [2], and the other two additional algorithms are developed in this study to realize the almost $O(N)$ costs (precisely, the $O(N \log N)$ costs) with keeping the high accuracy. FDP=H-matrices are expected to be applicable to various problems at almost $O(N)$ memory and computation costs.

The newly developed two algorithms are called the quantization method (Quantization) and the averaged reduced time (ART) (both introduced in §3). Quantization is an efficient algorithm reducing the numerical costs for ST-BIEM based on the sparse sampling of the kernel implemented by the quantization in the signal processing [25]. Quantization is applied to Domain I in FDP=H-matrices. ART is a sparse-matrix operation necessary to incorporate H-matrices into wave propagation phenomenon with FDPM, using approximate (averaged) elapsed time since the wave arrival (the reduced time [26]). ART is based on the plane wave approximation, and is applied to respective domains of FDPM in FDP=H-matrices.

In the following sections, first, we briefly describe the previously proposed two algorithms (FDPM and H-matrices) used in FDP=H-matrices, and then outline the relationships between the combined internal algorithms (FDPM, H-matrices, Quantization, and ART). Next, we detail the newly developed two algorithms (Quantization and ART) and present the actual arithmetic processes of FDP=H-matrices. Finally, we demonstrate the cost reductions and computational accuracies.

To guide the reader, we have listed used variables and parameters in Table 1, 2, 3, and 4.

Given problem	
$(\mathbf{x}, \xi) \in \mathbb{R}^{D_v}$	position in $D_v (= 2, 3)$ -dimension
$r \in \mathbb{R}$	distance
$(t, \tau) \in \mathbb{R}$	time
$\mathbf{u}(\mathbf{x}, t) \in \mathbb{R}^{D_v}$	displacement at \mathbf{x} at t
$\rho \in \mathbb{R}$	mass density
$(\lambda, \mu) \in \mathbb{R}$	elastic constants
$\sigma(\mathbf{x}, t) \in \mathbb{R}^{D_v \times D_v}$	stress at \mathbf{x} at t
Γ	boundary area
$\nu(\xi) \in \mathbb{R}^{D_v}$	normal vector at ξ (on Γ)
$T(\xi, \tau) \in \mathbb{R}^{D_v}$	traction at ξ at τ
$\Delta u(\xi, \tau) \in \mathbb{R}^{D_v}$	slip distance at ξ at τ .
$\Delta \dot{u}(\xi, \tau) \in \mathbb{R}^{D_v}$	slip rate at ξ at τ .
$K(\mathbf{x}, \xi, t - \tau) \in \mathbb{R}^{D_v^3}$	kernel connecting $\Delta u(\xi, \tau)$ and $\sigma(\mathbf{x}, t)$
$L \in \mathbb{R}$	characteristic length of the discretized object
Original ST-BIEM	
$N \in \mathbb{N}$	numbers of elements
$M \in \mathbb{N}$	numbers of time steps
$i = 1, \dots, N$	receiver number
$j = 1, \dots, N$	source number
$n = 0, \dots, M - 1$	the latest time step
$m = 0, \dots, M - 1$	elapsed time step
$\Delta x_j \in \mathbb{R}$	spatial discretization widths of j
$\Delta t \in \mathbb{R}$	temporal discretization width
$\mathbf{x}_i \in \mathbb{R}^{D_v}$	spatial collocation point of element i
$\nu_i \in \mathbb{R}^{D_v}$	normal vector of element i
$T_i(t) \in \mathbb{R}$	stress of receiver i at time t
$T_{i,n} \in \mathbb{R}$	stress of receiver i at time step n
$D_j(\tau) \in \mathbb{R}$	slip rate of j at time τ
$D_{j,n-m} \in \mathbb{R}$	slip rate of j at time step $n - m$
$K_{i,j}(t - \tau) \in \mathbb{R}$	kernel connecting $D_j(\tau)$ and $T_i(t)$
$K_{i,j,m} \in \mathbb{R}$	kernel connecting $D_{j,m}$ and $T_{i,n}$
$\mathbf{T}(t) \in \mathbb{R}^N$	vector placing $T_i(t)$ at the i component
$\mathbf{T}_n \in \mathbb{R}^N$	vector placing $T_{i,n}$ at the i component
$\mathbf{D}(\tau) \in \mathbb{R}^N$	vector placing $D_j(\tau)$ at the j component
$\mathbf{D}_{n-m} \in \mathbb{R}^N$	vector placing $D_{j,n-m}$ at the j component
$K(\tau) \in \mathbb{R}^{N \times N}$	matrix placing $K_{i,j}(\tau)$ at the i, j component
$K_m \in \mathbb{R}^{N \times N}$	matrix placing $K_{i,j,m}$ at the i, j component

Table 1 List of variables used in the text. The list contains the spaces to which the variables belong. \mathbb{R} and \mathbb{N} respectively represent the sets of real numbers and natural numbers. Although the spaces to which T , D , and K belong depend on D_v (denoting the dimension of the given problem), such dependencies are abbreviated for simple explanation. In the actual application, the fast algorithms (FDP, H-matrices, Quantization, and FDP=H-matrices) are applied to each component pair of σ and Δu in the given problem.

2 Definitions of Problems and Previous Techniques Used in FDP=H-matrices

In this section, we first define the targeted problem based on the spatiotemporal BIEM (in §2.1). Subsequently, we outline the previously proposed two internal algorithms of FDP=H-matrices: FDP (in §2.2) and H-matrices (in §2.3).

2.1 Spatiotemporal BIEM

Throughout this study, we solve elastodynamic problems, particularly focusing on mixed boundary value problems in an infinite homogeneous isotropic linear elastic medium. Ei-

ther two-dimensional (2D) or three-dimensional (3D) problems are treated hereafter. The equation of motion is written in the medium as

$$\rho \partial_t^2 \mathbf{u}(\mathbf{x}, t) = (\lambda + \mu) \nabla (\nabla \cdot \mathbf{u}(\mathbf{x}, t)) + \mu (\nabla \cdot \nabla) \mathbf{u}(\mathbf{x}, t),$$

where $\mathbf{u}(\mathbf{x}, t)$ is the displacement at the position \mathbf{x} and time t , ρ is the density of mass in the medium, and λ and μ are elastic coefficients; $\partial_t = \partial/(\partial t)$ and $\nabla = (\partial/(\partial x_1), \partial/(\partial x_2), \partial/(\partial x_3))$ respectively denote temporal and spatial partial differential operators.

The boundary conditions are described by the traction $T(\xi, \tau) = \nu(\mathbf{x}, t) \sigma(\xi, \tau)$ and the time partial differential $\Delta \dot{u}(\xi, \tau)$ (called the slip rate) of displacement discontinuity $\Delta u(\xi, \tau)$ (called the slip) on the arbitrarily shaped boundary area(s) Γ (called the fault area), where $\nu(\xi, \tau)$ and $\sigma(\xi, \tau)$ respectively denote the normal vector and the stress at the position ξ located on Γ and time τ . The a, b component of σ is written as $\sigma_{ab} = \lambda \delta_{ab} \partial_c u_c + \mu (\partial_a u_b + \partial_b u_a)$, where ∂_a represents the a th component of ∇ . The boundary condition is arbitrarily given by the traction T and slip rate $\Delta \dot{u}$ with some additional temporally evolving variables such as the slip. An example of the boundary condition will be shown in the numerical experiments of propagating crack problems of §6.2. The fault Γ is assumed to be represented by multiple smooth boundaries, such as a kinked boundary that can be represented by the two smooth boundaries connected at the kink.

The equation to be computed is the non-hypersingular integral equation of stress derived from Betti's representation theorem [26] with the regularization technique [27, 15]. This is formally expressed as

$$\sigma(\mathbf{x}, t) = \int_{\Gamma} d\Sigma(\xi) \int_0^t d\tau K(\mathbf{x}, \xi, t - \tau) \Delta \dot{u}(\xi, \tau), \quad (1)$$

where K denotes the kernel convolved over the fault area Γ and the past time τ . The component indices are abbreviated here for brevity. We assumed quiescent past, $\Delta \dot{u}(\xi, \tau)$ at $\tau < 0$ for simple formulation, although the temporal convolution can be defined to include the infinite past [28].

The kernel K has preferable natures ascribable to those of the Green's function of the medium, later mentioned in §2.2. The explicit forms of K [29] are not relevant for the algorithms proposed in this paper.

We use the discretized expression of Eq. (1) for numerical analyses, as in previous studies for both two-dimensional (2D) problems [28] and three-dimensional (3D) problems [23]. However, note that the spatial discretization and temporal discretization are imposed at different steps of constructing FDP=H-matrices, because the temporal discretization of the kernel is modified from that of the original BIEM so as to fit the approximations of ART. The way of such modification and the accuracy are detailed in §4.3 and §B.

The spatial discretization of the variables is imposed first. We apply the spatial piecewise-constant interpolation to the slip rate, and define the slip rate of the element $j = 1, \dots, N$

FDPM	
$c(=\alpha, \beta) \in \mathbb{R}$	phase speed (of P and S waves)
$t_{ij} \in \mathbb{R}$	travel time for collocation points of the receiver i and source j
$t_{ij}^-, t_{ij}^+ \in \mathbb{R}$	wave arrival time and wave passage completion time for i and j
$\Delta t_j^\pm \in \mathbb{R}$	temporal distance between t_{ij}^\pm and t_{ij}
$m_{ij}^-, m_{ij}^+ \in \mathbb{R}$	time steps respectively experiencing wave arrival and wave passage completion
$K^W(t) \in \mathbb{R}^{N \times N}$	kernel of Domain $W=F$ (Fp, Fs), I, S
$T^W \in \mathbb{R}^N$	stress response of Domain $W=F$ (Fp, Fs), I, S
$\hat{K}^I, \hat{K}^S \in \mathbb{R}^{N \times N}$	matrices respectively representing spatial dependence of $K_{ij}^I(t)$ and $K_{ij}^S(t)$
$h_m^I \in \mathbb{R}$	time step $m = 0, \dots, M-1$ dependent part of the discretized kernel in Domain I.
H-matrices	
$diam \in \mathbb{R}$	ceiling of diameter for the minimum circle covering a given cluster
$dist \in \mathbb{R}$	floor of the minimum distance between given two clusters
$l_{min} \in \mathbb{R}$	parameter bounding the minimum cluster size in admissible leaves
$\eta \in \mathbb{R}$	parameter bounding the maximum ratio of $diam$ to $dist$ in admissible leaves
$a \in \mathbb{N}$	block cluster number
$\epsilon_H, \epsilon_{ACA} \in \mathbb{R}$	parameters for bounding errors of the low-rank approximation (LRA) and ACA
$N_{re,a}, N_{so,a} \in \mathbb{N}$	the numbers respectively of sources and receivers in a block cluster a
$\mathbf{f}_{al} \in \mathbb{R}^{N_{re,a}}$	the l -th vectors of the a -th approximated submatrices for receivers
$\mathbf{g}_{al} \in \mathbb{R}^{N_{so,a}}$	the l -th vectors of the a -th approximated submatrices for sources
l_a^*	rank of submatrices a after LRA

Table 2 List of variables used in the text (continued).

Quantization	
$\epsilon_Q \in \mathbb{R}$	allowed relative error
$\epsilon_{st} \in \mathbb{R}$	allowed absolute error
$q \in \mathbb{N}$	quantization number
$b_q \in \mathbb{N}$	the q -th sampled time step
FDP=H-matrices	
$\hat{K}_{ij}^F \in \mathbb{R}^{N \times N}$	amplitude term of i and j
$h_{ij}^F(t) \in \mathbb{R}$	normalized waveform of i and j
i_*	representative receiver
j_*	representative source
$\delta t_i \in \mathbb{R}$	travel time difference of i
$\bar{t}_j \in \mathbb{R}$	receiver averaged travel time of j
$h_j^F(t) \in \mathbb{R}$	degenerating normalized waveform of j
$c_{ij} \in \mathbb{R}$	approximate acoustic speed of i and j
$\eta_0 \in \mathbb{R}$	η at $\delta r = l_{min}$
$\bar{m}_j^- \in \mathbb{Z}$	receiver averaged travel time step for j
$\Delta m_j \in \mathbb{Z}$	discretized duration of Domain F
$h_{j,m}^F \in \mathbb{R}$	temporally discretized $h_j^F(t)$ at a time step m
$\delta m_i \in \mathbb{Z}$	travel time step difference of the receiver i
$\hat{D}_{j,n}^F \in \mathbb{R}$	convolution of $D_{j,n-m}$ and $h_{j,m}^F$
$T_m \in \mathbb{R}$	reference stress at time step m

Table 3 List of variables used in the text (continued). \mathbb{Z} represents the set of integers.

at the arbitrary time t , denoted by $D_j(t)$. The shape of the boundary element can be arbitrary. Hereafter, The characteristic size of the element j is supposed to be given by Δx_j (specified in §2.2). The traction of the element $i = 1, \dots, N$, denoted by $T_i(t)$, is defined as the traction $T_i(t) := \nu_i \sigma(\mathbf{x}_i, t)$ at a collocation point \mathbf{x}_i , where ν_i is the normal vector of the element i . In this paper, \mathbf{x}_i is set at the center (of mass) of each element as often adopted [1]. The projection of σ onto T by ν is omitted hereafter for simply presenting the algorithms. (The management of this projection is related to the accuracy of FDP=H-matrices, as explained in §E.1.) After

the above spatial discretization, the convolution in Eq. (1) is converted to

$$T_i(t) = \sum_{j=1}^N K_{i,j} * D_j(t), \quad (2)$$

where $*$ denotes temporal convolution and $K_{i,j}$ is the corresponding discretized kernel for the receiver i and the source j . In Eq. (2), the summation $\sum_{j=1}^N$ represents the discretized spatial convolution. Eq. (2) using the spatial symbols of the receiver i and source j is shortened to a matrix-vector representation as

$$\mathbf{T}(t) = \mathbf{K} * \mathbf{D}(t), \quad (3)$$

where $\mathbf{T}(t)$ and $\mathbf{D}(t)$ denote vectors whose components are respectively the tractions and slip rates, of elements at time t as $\mathbf{T}(t) = (T_1(t), T_2(t), \dots, T_N(t))^T$ and $\mathbf{D}(t) = (D_1(t), D_2(t), \dots, D_N(t))^T$, where $()^T$ denotes the transpose. Similarly $K(t)$ denotes the matrix whose i, j component is defined as $(K(t))_{i,j} := K_{i,j}(t)$. We will recall the temporally continuous convolution, Eq. (3) in §4 and §B to introduce the approximations of ART used in FDP=H-matrices.

The temporal discretization is next introduced. The slip rates are discretized by the piecewise constant interpolation within the time interval Δt , and the collocation time is selected at each time step $n = 0, \dots, M-1$, as in many previous studies [27, 28, 1]. Adaptive time steps [17] is out of the scope in this study. We then obtain the spatiotemporally discretized expression of Eq. (1);

$$\mathbf{T}_n = \sum_{m=0}^{M-1} K_m \mathbf{D}_{n-m}, \quad (4)$$

where \mathbf{T}_n and \mathbf{D}_n respectively denote the vector representations of the temporally discretized tractions and slip rates, at

FDP=H-matrices (continued)	
$S^{source} \in \mathbb{R}^{\max[\tilde{m}_j] \times N_{so,a}}$	time shift matrix for sources
$S^{receiver} \in \mathbb{R}^{N_{re,a} \times \max[\delta m_i]}$	time shift matrix for receivers
$\tilde{T}_n \in \mathbb{R}^{\max[\delta m_i + \tilde{m}_j]}$	vector the m -th component of which is \tilde{T}_{n-m} at time step n
$F \in \mathbb{R}^{N_{re,a} \times \max[\delta m_i]}$	sparse matrix embedded with f along nonzero components of $S^{receiver}$
$G \in \mathbb{R}^{\max[\tilde{m}_j] \times N_{so,a}}$	sparse matrix embedded with g along nonzero components of S^{source}
$M \in \mathbb{R}^{\max[\delta m_i + \tilde{m}_j] \times \max[\delta m_i + \tilde{m}_j]}$	matrix the m, m' component of which is $\delta_{m,m'+1}$.

Table 4 List of variables used in the text (continued). The maximums to determine the dimensions of \tilde{T} , S^{source} , $S^{receiver}$, F , G , and M such as $\max[\delta m_i]$ are taken in each leaf a .

a time step n . The K_m is the temporal discretization of $K_{i,j}(t)$ adjusting the temporal discretization of the slip rate.

The summation $\sum_{m=0}^{M-1}$ in Eq. (4) represents the discretized temporal convolution. Hereafter in this paper, n denotes the current time step (corresponding to t in Eq. (1)). Similarly, in the convolution, m is used for expressing the elapsed time step (corresponding to $t - \tau$ in Eq. (1)) since the beginning of the temporal convolution.

We finished obtaining the discretized BIEM as above. Last we show the cost problem of the original ST-BIEM schematically. In Fig. 1 (top left), the original kernel of ST-BIEM (in Eq. (4)) is described by a cuboid rectangular parallelepiped defined in the coordinate spanned by the source number axis i , receiver number axis j , and time step number axis m . Similarly, the slip rate becomes a quadrilateral defined in the coordinate spanned by the source number axis and time step number axis. The volume of the kernel in this figure represents $O(N^2M)$ costs to store it in memory and to convolve it computationally. The area of the slip rate represents the $O(NM)$ memory to store it. This fully discretized ST-BIEM (Eq. (4)) is evaluated by the fast arithmetics of FDP=H-matrices, only using the sparse matrices and vectors of almost $O(N)$, as later overviewed in §5.

Hereafter, for simple order estimates of the cost, the boundary elements are supposed to be closely spaced so that $L/(\beta\Delta t) = O(N^{1/D_b})$ is satisfied, where L is the characteristic size of the fault and $D_b \geq 1$ is the dimension of the fault. It does not mean the fault area is a single plane, as exemplified by the distributed fault planes tested in §4.2.2. Note that our proposition can be applied beyond this assumption (such as excessively distant two fault planes). General cost estimates are shown in §B.5 after FDP=H-matrices are fully developed.

2.2 FDPM

We here outline FDPM [1,2]. We will focus on the incorporated domain partitioning technique, which is especially important in FDP=H-matrices. To simplify the explanation, we consider the case of a linearly aligned same shaped boundary elements in the 3D space, although FDPM is applicable to nonplanar boundaries in both 2D and 3D problems.

Note that the analytic presentations of the kernel in FDPM is briefly explained here since the algorithm of FDP=H-matrices are independent of them. See [1] and [2] for the detail of the analytical aspects of FDPM.

The time domain of the (isotropic homogeneous elastodynamic) integral equation, Eq. (1), is divided into three domains characterized by different stresses. Such division is shown in Fig. 1 (right, labeled as the domain partitioning). The original kernel represents the stress change of the receiver i caused by the motion of the source j . The diagonal cross section illustrated in the box describes the behavior of the kernel. It corresponds to the propagating stress field over the receivers j after the emission from the source i . The colored areas on the cross section represent the three time domains mentioned earlier: that of the wave (red), that of the near-field term (orange), and the static stress (ivory) (hereafter referred to as the stress of the static term). They are respectively called Domain F, Domain I, and Domain S, in FDPM. The gray areas are out of the causality cone, where the kernel takes zero value, and excluded from the convolution.

Domain F is defined as time ranges involving wavefronts of finite widths caused by the spatiotemporal discretization of boundary elements. The time ranges of Domain F are characterized by their durations and the propagation times (called the travel time [26]) of the P- and S-waves radiated from a source collocation point propagated to a receiver collocation point. The travel time of source and receiver collocation points, t_{ij} , is given by

$$t_{ij} := r_{ij}/c, \quad (5)$$

where r_{ij} is the distance between collocation points of the source (j) and the receiver (i); c represents the phase velocity of P-waves (denoted by α) or S-waves (denoted by β). Hereafter, the travel time between source-receiver collocation points is briefly called the travel time. The travel times of P and S waves are respectively denoted by $t_{ij}^\alpha := r_{ij}/\alpha$ and $t_{ij}^\beta := r_{ij}/\beta$. The duration of Domains F is characterized by the temporal distances of the travel times to the leading and trailing edges, respectively denoted by Δt_j^{c-} and Δt_j^{c+} ($c = \alpha$ and β respectively in the case of F=FP and Fs). The time range involving wavefronts of P-waves (called Domain

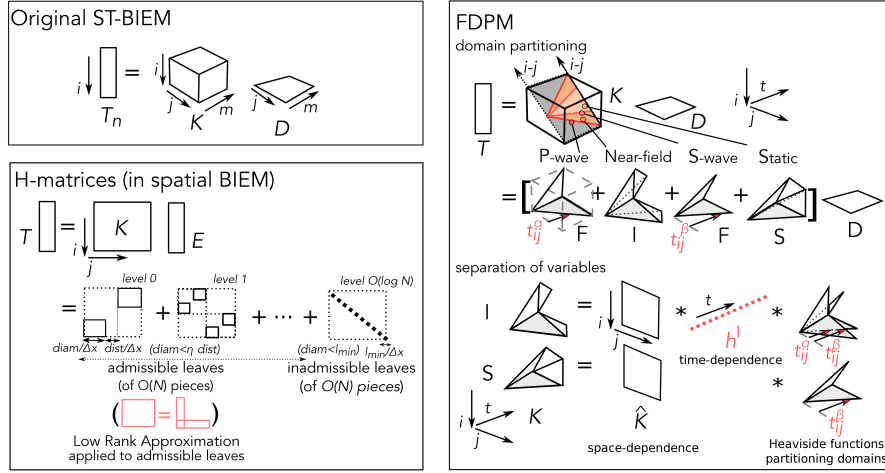


Fig. 1 Schematic diagrams of the original ST-BIEM, FDPM, and H-matrices. (Top left) The original ST-BIEM convolving K and D to evaluate T . The kernel K is represented by the parallelepiped spanned by the vectors of the receiver ($i = 1, \dots, N$), source ($j = 1, \dots, N$), and time step ($m = 0, \dots, M - 1$). The volume of the rectangular parallelepiped expresses the memory and computation cost of $O(N^2M)$. (Bottom left) Schematics of H-matrices exemplified by a 2D linear boundary case of spatial BIEM. The kernel matrix is divided into submatrices representing interactions between pairs of source clusters and receiver clusters. Cluster pairs are selected so that the receiver cluster and source cluster are sufficiently distant (in the case of admissible leaves) or clusters are excessively small (in the case of inadmissible leaves). Further applying low rank approximations to the kernel of admissible leaves, the cost is reduced. Two measures of the clustering, $dist$ and $diam$, are written in the matrix in the panel after divided by the element length Δx ($\forall j, \Delta x_j = \Delta x$ in this example). The parameters η and l_{min} are also described. (Right) Schematics of FDPM exemplified by a 3D linear boundary. The kernel is partitioned into Domain F, the union of Domains Fp and Fs respectively enclosing the P or S wave speed (the red parts), Domain I in-between Fp and Fs only enclosing near-field terms (the orange parts), and Domain S after Fs only enclosing static terms (the ivory part). Domains Fp and Fs are determined by using the propagation times of the P and S waves (the travel times) between the collocation points of the receiver i and the source j . The cost is reduced by the separation of spatiotemporal variables in the kernels of Domains I and S, where the kernel is separated into the spatial parts depending only i and j , the temporal parts depending only m , and the Heaviside functions determining the time steps of the starts and the ends of Domains I and S only depending i and j .

Fp) and that of S waves (called Domain Fs) are respectively defined as $t - \tau$ (in Eq. (1)) fulfilling $-\Delta t_j^{\alpha-} < (t - \tau) - t_j^{\alpha} < \Delta t_j^{\alpha+}$ and $-\Delta t_j^{\beta-} < (t - \tau) - t_j^{\beta} < \Delta t_j^{\beta+}$. Domain F is given as the union of Domains Fp and Fs.

The duration of Domain F is rather arbitrary as long as Domain F involves the exact duration of the wavefront. In 3D problems, when we adopt $T_{i,n} = T_i((n+1)\Delta t)$ and $D_j(t) = \sum_m D_{j,m}[H(m\Delta t - t) - H((m+1)\Delta t - t)]$, Δt_j^{\pm} of the wavefronts can be evaluated as the following forms [2] depending on the characteristic length Δx_j of the source j , the temporal discretization width Δt , and c :

$$\Delta t_j^{c+} = \Delta x_j / (2c) + \Delta t \quad (6)$$

$$\Delta t_j^{c-} = \Delta x_j / (2c). \quad (7)$$

We here set Δx_j at twice the maximum distance between the collocation point and the position within the element j . $\Delta x_j / (2c)$ corresponds to the maximum duration expected from the fault element geometry, and Δt is the safe coefficient for treating the time discretization in Eqs. (6) and (7). In 2D problems, Δt_j^{c+} is set again as a parameter so as to suppress the error caused by the spatiotemporal separation of the kernel in Domains I and S, since line (2D) seismic sources cause long temporal tails of wavefronts [1]. After the temporal discretization, the discretized Domain Fp

and Fs are respectively defined as the time steps m fulfilling $m_{ij}^{\alpha-} \leq m < m_{ij}^{\alpha+}$ and $m_{ij}^{\beta-} \leq m < m_{ij}^{\beta+}$, where the time steps m_{ij}^{c-} and $m_{ij}^{c+} - 1$ are respectively defined as time steps enclosing the collocation time minus $t_{ij}^{c-} := t_{ij}^c - \Delta t_j^{c-}$ and $t_{ij}^{c+} := t_{ij}^c + \Delta t_j^{c+}$.

Definitions of Domain I and Domain S are straightforward as respectively located in-between Domains Fp and Fs and after Domain Fs. Hereafter, K^W (called the kernel of Domain W) and T^W (called the stress response of Domain W) respectively denote the kernels corresponding to Domains $W = F$ (Fp, Fs), I, S and the convolutions of those kernels with slip rates.

The kernels of Domains I and S are separated into their space-dependent parts (respectively denoted by \hat{K}^I and \hat{K}^S) and their time-dependent parts (respectively denoted by h^I and 1), except for Heaviside functions representing their domain partitions [1,2]. This is illustrated in Fig. 1 (right, labeled as separation of variables). This separation does not deteriorate the accuracy in 3D problems due to the finiteness of the wavefront phases, while they do so to some extent in 2D problems due to the abovementioned long tails of them [2].

The memory consumption and time complexity of the convolution in FDPM are much smaller than those of the

original ST-BIEM. The memory consumption of FDPM is of $O(N^2 + L/(\beta\Delta t)) = O(N^2)$, due to the separation of variables in the kernels of Domains I and S [2], where L is the spatial length of the object (usually of $L/(\beta\Delta t) \leq M$). Regarding the time complexity of the convolution, it is of $O(N^2)$ in Domain F from the beginning, since the time length of Domain F is of $O(1)$ for each source-receiver pair. The time complexity in Domain S becomes of $O(N^2)$, by using the stored sum of the slip rate D_{n-m} in Domain S ($m \geq m_{ij}^{\beta+}$) [2]. The time complexity in Domain I becomes of $O(N^2 + NL/(\beta\Delta t)) = O(N^2)$ by first evaluating the temporal convolution $\hat{D}_{j,m}^I := \sum_{m'=1}^{m-1} h_{m'} D_{n-m'}$ of the slip rate and h^I at each time step n with $O(NL/(\beta\Delta t))$ costs; the stress of Domain I for all receivers i is then evaluable as $T_{i,n}^I := \sum_j \hat{K}_{i,j}^I [\hat{D}_{j,m_{ij}^{\beta-}}^I - \hat{D}_{j,m_{ij}^{\alpha+}}^I]$ at $O(N^2)$ costs.

2.3 H-matrices

H-matrices hierarchically divide the kernel matrix into submatrices with different sizes by considering the distances between sources and receivers (as shown in Fig. 1 (bottom left)) and apply the low rank approximation (LRA) to the kernel submatrices. Below, we briefly describe the techniques (to store the kernel and to convolve it) and notations of H-matrices used throughout this paper, following [19].

We here consider spatial BIEM computing the stress at the boundary given as $T_i = \sum_j K_{i,j} E_j$ (illustrated in Fig. 1 (bottom left)), where T_i and E_j respectively denote the traction of the receiver i and the slip of the source j ; $K_{i,j}$ denotes the kernel matrix component connecting T_i and E_j . For the sake of simple explanations, the case of a planar boundary source of a 2D problem is considered and the boundary elements are numbered sequentially from one end to the other here without contradicting the generality of H-matrices applicable to nonplanar faults in 2D and 3D problems.

The kernel matrix is first divided into the set of submatrices. The division is frequently implemented by using the box bounding the space containing the elements (called the bounding box [19]). Following the division of a bounding box, the set of boundary elements enclosed within the bounding box are divided into sub-sets (called clusters [19]) such that neighboring elements are gathered. As receivers and sources are divided, the row and column of the kernel matrix are also divided into submatrices. The division of a submatrix is continued until one of the stop conditions are satisfied by the pair of receiver clusters and source clusters (called a block cluster [19]) corresponding to the submatrix; examples of the stop conditions are given as

$$diam < \eta \cdot dist \quad (8)$$

$$diam < l_{min}, \quad (9)$$

where $diam$ is the maximum distance between the boundary elements contained in each cluster, $dist$ is the shortest distance between the boundary elements contained in the receiver cluster and those contained in the source cluster, where the distance between two elements are defined by the shortest distance of a location on one element and a position on the other element; η and l_{min} are the accuracy controlling parameters of the clustering. In the case of linearly aligned same-shaped elements, as shown in Fig. 1 (bottom left), $diam$ and $dist$ can be related to the sizes of individual sub-matrices and separations between certain two sub-matrices, after divided by the boundary element length $\Delta x_j = \Delta x$. Since the specific definitions of these conditions are largely arbitrary, in §4.2, we define the conditions used in this paper in detail. (It is extended in §4.2.2 to evaluate the effect of chosen conditions to FDP=H-matrices.) The condition, Eq. (8) is for evaluating a sufficiently distant cluster pair, and is called the admissibility condition. The condition, Eq. (9) is for evaluating clusters that are too small, and is called the inadmissibility condition. A pair of the source cluster and receiver cluster that satisfies one of the stop conditions, Eqs. (8) and (9), is a leaf of the graph (called the block cluster tree [19]) formed by this clustering process. A pair that satisfies Eq. (8) is called an admissible leaf. A pair that satisfies Eq. (9) is called an inadmissible leaf. After the construction of the block-cluster tree, the kernel is divided into the partial kernels as $K = \sum_a K_a$ (Fig. 1 (bottom left)), where a denotes the leaf number and K_a is the corresponding a -th partial kernel. The size of each submatrix is characterized in the block cluster tree by the number of divisions (called level) performed until the submatrix is obtained.

Based on the obtained block cluster tree, the kernel is approximated and convolved. A kernel submatrix, K_a , of an admissible leaf a is approximated to a low-rank kernel, $K_{a,LRA} := \sum_{l=0}^{l_a^*-1} \mathbf{f}_{a,l} \otimes \mathbf{g}_{a,l}$ ($K_a \approx K_{a,LRA}$, illustrated by a red square and two bars in Fig. 1 (bottom left)), where l_a^* is the rank of $K_{a,LRA}$, $\mathbf{f}_{a,l}$ and $\mathbf{g}_{a,l}$ respectively denote the column and row vectors, corresponding to the l -th largest singular value of K_a , and \otimes represents a tensor product. The accuracy of LRA, $K_a \approx K_{a,LRA}$, is controlled to satisfy the relative error condition $|K_a - K_{a,LRA}| < \epsilon_H |K_a|$ in each leaf, where $\epsilon_H < 1$ is a given constant and $|K|$ denotes the Frobenius norm of a matrix K . The approximation is commonly implemented with fast approximate algorithms of the singular value decomposition, such as the adaptive cross approximation (ACA) [20]. After LRA, the convolution of above-mentioned spatial BIEM is evaluated as

$$T_i = \sum_{a \in A_{adm}, l} f_{a,l,i} \sum_j g_{a,l,j} D_j + \sum_{a \in A_{inadm}} K_{a,i,j} D_j, \quad (10)$$

where A_{adm} and A_{inadm} respectively denote the sets of admissible leaves and inadmissible leaves. Note that, in conventional terminology, the above kernel approximation methods (including the above clustering and convolution tech-

nique) are referred to as H-matrices, and the approximated matrix is referred to as an H-matrix [19].

The memory and computation costs of H-matrices are estimated as below. See [19] for details. The costs of admissible leaves, originally of $O(\sum_a N_a^2)$, become of $O(\sum_a 2N_a l_a^*)$ by LRA, where N_a denotes the number of source and receiver elements in the leaf a . The rank l_a^* is normally of $O(1)$ attained by a preferable nature of the value of the static kernels that their values are proportional to the power of the source-receiver distance [19]. In addition, in each level c , the number of block cluster and a number of source (or receiver) elements in a block cluster are respectively of $O(2^c)$ and $O(N/2^c)$. (See Fig. 1 (bottom left).) The maximum of the level is of $O(\log N)$. Because of these, the costs of admissible leaves are estimated to be of $O(\sum_a 2N_a l_a^*) = O(\sum_a N_a) = O(N \log N)$. On the other hand, the costs of diagonally distributed inadmissible leaves are strictly of $O(N)$. Since the costs of the admissible leaves and inadmissible leaves are respectively of $O(N \log N)$ and of $O(N)$, the $O(N^2)$ costs of spatial BIEM are eventually reduced to be of $O(N \log N)$ by H-matrices.

3 Overview of New Method

3.1 Outline and Relationship of Internal Algorithms in FDP=H-matrices

To begin proposing FDP=H-matrices, we explain the relation among the internal algorithms.

Fig. 2 provides the view of FDP=H-matrices, comprising FDPM (§2.2), H-matrices (§2.3), the quantization method (Quantization) (§3.2.3), and the averaged reduced time (ART) (§4.2). Quantization and ART are developed later in this study. FDPM (§2.2) first divides the integral kernel of the stress computation (called the kernel) into three domains: Domain F representing wavefronts of finite widths (the red part in Fig. 2 (top left)), Domain I representing near-field terms (the orange parts), and Domain S representing static terms (the ivory part). In order to care the different properties of respective domains, left internal algorithms are combined in three ways in those domains (Fig. 2 (center)).

In Domain F, 1) FDPM converts the time variable t of the real coordinate (\mathbf{x}_{ij}, t) into the reduced time $t - r_{ij}/c$ (detailed in §3.2.1), where c denotes the phase velocity; $\mathbf{x}_{ij} = \mathbf{x}_i - \mathbf{x}_j$ and $r_{ij} = |\mathbf{x}_{ij}|$ respectively denote the relative position and distance between the receiver i and the source j . 2) An H-matrix is introduced along the wavefronts described by the coordinate $(\mathbf{x}_{ij}, t_{ij})$ (§4.1), where $t_{ij} := r_{ij}/c$ denotes the travel time [26] for the collocation points. Hereinafter, the superscript c appeared in FDPM (in §2.2) is abbreviated unless necessary. The travel time represents the time taken for a wave radiated from the collocation point of the source j to reach that of the receiver i . 3) ART is introduced to deal with

the natures of the kernels and slip rate history depending not only on space \mathbf{x} but also on time t for the spatiotemporal convolutions (detailed in §4.2).

In Domain I, 1) FDPM separates the kernel into a time-dependent function represented by a vector and a space-dependent function represented by a matrix (§2.2). 2) An H-matrix is introduced along the spatial \mathbf{x} direction. 3) Quantization approximates the kernel in the temporal t direction (§3.2.3). 4) ART is introduced similarly to Domain F. ART works in Domain I to separate the receiver i and source j dependence of the travel time partitioning the domains.

In Domain S, 1) FDPM reduces the kernel to a space-dependent function represented by a matrix (§2.2). 2) An H-matrix is introduced along \mathbf{x} direction (§3.2.2). 3) ART is introduced as in Domain I.

Those steps are essential to treat respective domains. Information on these points are supplemented below.

Supplemental on essential points in Domain F Three essential points of Domain F are further explained. The first is transforming the original time t into the elapsed time $t - r_{ij}/c$ from the wave arrival (the reduced time) for each pair of the receiver i and source j . The origin of the transformed time is the wave arrival time determined by the travel time $t_{ij} = r_{ij}/c$ defined in §2.2. The kernel for a certain fixed reduced time shows the decay in proportion to the powers of source-receiver distance (the geometrical spreading) [2]. The second is to apply H-matrices along the wavefronts (detailed in §4.1). H-matrices successfully approximate the matrix representing the (geometrically spreading) kernel for a certain fixed reduced time. This avoids the difficulty, arising from crossing the wave front singularities for applying H-matrices [19, 24]. The third is to use ART (Fig. 2 (bottom right)) for performing the sparse matrix arithmetic described in §5. ART reduces the travel time t_{ij} to $t_{ij} \approx \delta t_i + \bar{t}_j$ (Eq. (19), travel time separation) and separates the dependence of the travel time on the receiver i and the source j ; δt_i denotes a travel time difference (the receiver-dependent travel time difference) between the receiver position i (\mathbf{x}_i) and the average position of multiple receivers in the vicinity (\mathbf{x}_{i_*}), where i_* denotes a virtual receiver located at \mathbf{x}_{i_*} ; \bar{t}_j denotes the travel time between i_* and the source j (the receiver-averaged travel time). ART is based on the plane wave approximation described in §4.2. In addition, ART eliminates the source dependence of the temporal change in the kernel of Domain F caused by the finite size and orientation of the source element. Such source dependence of the kernel of Domain F is illustrated by the variations in wavefront widths in Fig. 2 (bottom right).

Supplemental on essential points in Domains I and S Three essential points shared by Domains I and S are here supplemented. The first is that the kernel is separated by FDPM

into a space-dependent part and a time-dependent part in these domains [2]. Note that the time dependence of the kernel in Domain S is remarkably different between in 2D problems and in 3D problems. The time dependence of the kernel in Domain S is asymptotically eliminated in 2D problems, whereas the kernel in Domain S is exactly time-independent from the time in 3D problems [1, 2]. The second is H-matrices applied to the receiver-source dependent matrix representing the space dependence of the kernel (along the spatial direction x_{ij}). The details of the procedure are described in §3.2.2. The third is to apply ART for performing the sparse matrix arithmetics described in §B.1 and §B.2, which is concerning the travel time separation for the Heaviside functions partitioning the domains.

The fourth solely for Domain I is to apply Quantization to approximate the kernel temporally (Fig. 2 (top right)). Quantization is based on an sparse sampling of the near-field term (detailed in §3.2.3). Quantization is combined with ART in FDP=H-matrices (detailed in §B.2).

We finished describing the relations between the internal algorithms of FDP=H-matrices as above. The individual internal algorithms and the approximations used therein are outlined in the next §3.2.

3.2 Procedures to Lower the Order of Memory Consumption and Time Complexity

We overviewed the relations between FDPM, H-matrices, Quantization, and ART in FDP=H-matrices in §3.1. Below, we show how H-matrices, Quantization, and FDPM are combined in order to reduce the order of the numerical cost being of $O(N^2M)$ in the original ST-BIEM to be of almost $O(N)$ in FDP=H-matrices. The approximation method used in ART and a technique for applying H-matrices to Domain F are briefly mentioned in §3.2.1 (detailed in §4). Only the admissible leaves are treated hereafter, and the computations in the inadmissible leaves are mentioned in §C.

To apply FDP=H-matrices to ST-BIEM, we hereafter assume constant time interval in the temporal discretization, as introduced in §2.1, while the spatial grid size can be element dependent.

3.2.1 H-matrices Applied to Wavefronts Depending on Space and Time in Domain F

As mentioned in §1, the discretized kernel of ST-BIEM includes $O(N^2)$ components containing the singular points of the continuous kernel aligned along the wavefronts [13]. The number N^2 is caused by the number of the combinations of the source of $O(N)$ radiating the singular (impulsive) wave and the receiver of $O(N)$. These components of $O(N^2)$ prevent H-matrices from achieving $O(N)$ costs [19], because a singular point in the continuous kernel remains as an abrupt

change (not distinguished from a singular point hereafter) even after the discretization of the kernel.

To overcome this difficulty, FDP=H-matrices apply H-matrices along the wavefronts, as proposed originally by Ando [2]. This novel idea enables us to avoid applying H-matrices across $O(N^2)$ singular points and achieve almost $O(N)$ costs in Domain F, as a natural extension of FDPM.

We first present the schematic view of applying H-matrices to Domain F, the detail of which is shown later in §4. Originally, the kernel in Domain F is described by the receiver number i , source number j , and time t (Fig. 3, top left panel). The continuous (undiscretized) time t is used instead of the discretized time step here for ART introduced later. The Domain F kernel is redefined so that the time variable to express the time-dependence of the Domain F kernel is converted from the (real) time (t) to the elapsed time from the wave arrival ($t - m_{ij}^- \Delta t$, called the reduced time) for each receiver i and the source j (Fig. 3, bottom left panel); m_{ij}^- denotes the discretized time step experiencing the wave arrival for the receiver i and source j and corresponds to t_{ij}^- . As the real time axis is shifted in this way, the kernel in Domain F simply obeys the geometrical spreading depending solely on space for a given reduced time (detailed in §4.1). This time-shifted kernel, simply evaluated by using the analytic expression of the conventional ST-BIEM kernel (detailed in §4.3), is approximated by H-matrices in the spatial direction alone, not in the temporal direction (detailed in §4.3). The approximated spatial part of the kernel is represented by a sum of submatrices of $O(1)$ ranks.

The memory required to store the Domain F kernel is then reduced. The memory cost of FDPM in Domain F is originally on the order of $O(N^2)$, that is the product of the number of sources and the number of receivers, (Fig. 3, top right panel). This is because the discretized wavefront width ($m_{ij}^+ - m_{ij}^-$) is always of $O(1)$, meaning independent of the distance between the source and receiver; m_{ij}^+ denotes a time step the interval of which encloses the continuous time of the wave passage completion, t_{ij}^+ . The $O(N^2)$ memory, to store the matrix structure representing the source-receiver dependence of the Domain F kernel, is reduced to be of almost $O(N)$ by H-matrices along wavefronts (Fig. 3, bottom right panel).

As later introduced, the following three additional procedures are considered for the above approximations in Domain F (detailed in §4). 1) The Domain F kernel, K^F , is separated into the time-independent amplitude term (defined as the time integral of the Domain F kernel $\hat{K}^F := \int dt K^F$) and the normalized time-dependent term (called the normalized waveform, defined as $h_{ij}^F := K_{ij}^F / \hat{K}_{ij}^F$) (detailed in §4.1). Such \hat{K}^F is extracted by the temporal integration of the kernel over Domain F, and approximated by H-matrices as in the static problems. This separation removes the impulsive time dependence contaminated in the geometrically spread-

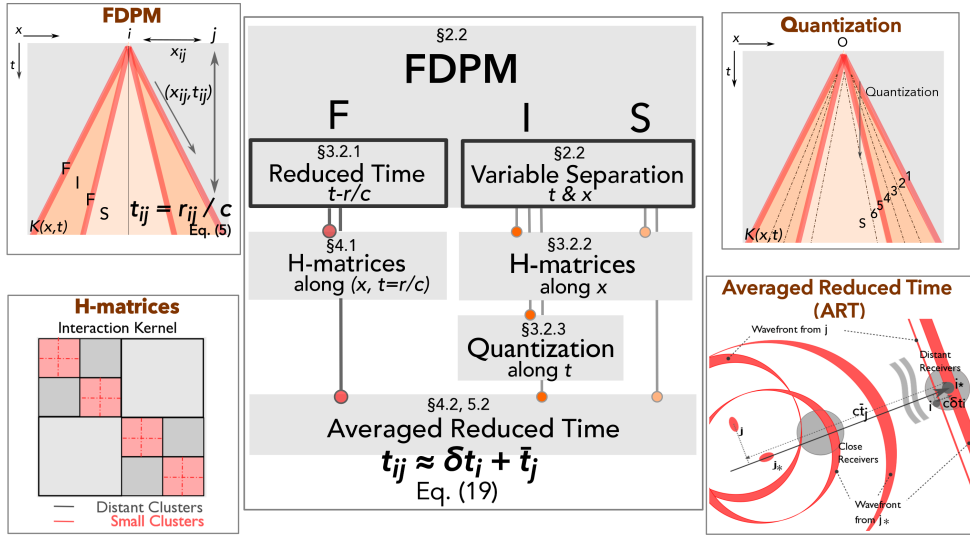


Fig. 2 The outline and relation of the internal algorithms, explained in §3.1. (Center) Cost reduction procedures in FDP=H-matrices. Items hanging under each Domain (F, I, and S) of FDPM shown in the top stage correspond to the cost reduction procedures of each. Numbers attached above each item are the section numbers of the corresponding explanation. (Top left) FDPM. The triangle schematically represents the spatiotemporal change in the stress wave radiated from the source j (called the causality cone). As detailed in Fig. 1 and §2.2, the time range of the integral equation is divided into Domain F (the red parts), Domain I (the orange parts), and Domain S (the ivory part) around the travel time t_{ij} , which is defined as the ratio of the source(j)-receiver(i) distance r_{ij} to the phase velocity c ($t_{ij} = r_{ij}/c$). The cost is reduced by the spatiotemporal separation of variables of the kernels in Domains I and S. (Bottom left) H-matrices. H-matrices divide the kernel into pairs of source clusters and receiver clusters where the receivers and sources are sufficiently distant (called admissible leaves) and cluster pairs whose clusters are excessively small (called inadmissible leaves). The cost is reduced by applying low rank approximations to the kernel of admissible leaves, as detailed in Fig. 1 and §2.3. (Top right) Quantization. Quantization performs the cost reduction by sparsely sampling the near-field term along the black dotted lines in §3.2.3. (Bottom right) The averaged reduced time (ART). By applying the plane-wave approximation to the wavefront radiated from the sources, ART separates the travel time t_{ij} into the receiver i dependent travel time difference δt_i and the source j dependent receiver-averaged travel time \bar{t}_j in §4.2. ART performs the sparse matrix operation described in §5.2.

ing nature of the Domain F kernel, in order to care the low rank approximation in H-matrices. 2) ART reduces t_{ij} and h_{ij}^F respectively to $t_{ij} \rightarrow \delta t_i + \bar{t}_j$, $h_{ij}^F \rightarrow h_j^F$ for each pair of the receiver i and source j (detailed in §4.2). 3) The discretized time definition range of Domain F is modified as $m_{ij}^\pm \approx \delta m_i + \bar{m}_j^\pm$ (detailed in §4.3).

3.2.2 H-matrices Applied to the Spatial Part of the Kernel in Domains I and S

In-between the P wavefronts and S wavefronts, the Domain I kernel, K^I , is separated into the space-dependent term and the time-dependent term by FDPM (Fig. 4, bottom left panel). After the S wave passage completion, the kernel of Domain S, K^S , is represented by a space dependent term only (Fig. 4, bottom left panel). The spatial dependent terms of K^I and K^S are represented by matrices depending on the receiver i and source j . These matrices representing space-dependences of the kernels are separated by H-matrices into the receiver i dependent vectors and source j dependent vectors (Fig. 4, top right panel). Consequently, the memory storage of K^I and K^S , which are of $O(N^2 + M)$ in FDPM, is reduced to be of almost $O(N)$ (Fig. 4, bottom right panel).

The $O(N^2)$ time complexity of Domain I is reduced to be of almost $O(N)$ by using ART and H-matrices. The Domain I kernel is originally convolved over the sources and the time steps for respective receivers and takes the $O(N^2)$ computation time. When H-matrices and ART separates the source-receiver dependence of the kernel, the time taken to compute the stress response of Domain I is reduced to be of $O(N)$ (detailed in §B.2).

The time complexity of Domain S becomes of almost $O(N)$ by using H-matrices and ART. The independence from the factor M is resulted from the time independence of the kernel in Domain S (detailed in §B.1).

3.2.3 Cost Reduction of Time Integral in Domain I by Quantization

The memory consumption required to evaluate the stress in Domain I is reduced to be of almost $O(N)$ by Quantization in FDP=H-matrices (detailed in §B.2.3). As outlined below, Quantization can reduce the memory consumption and time complexity based on the temporally sparse sampling of the kernel. Theoretical and numerical details of Quantization are shown in §A.

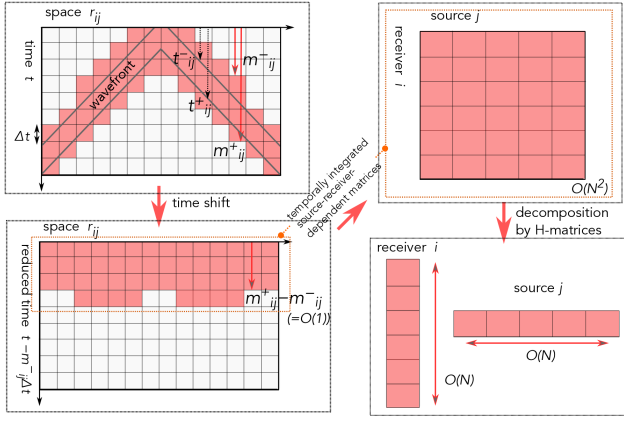


Fig. 3 Diagrams of the approximation procedure in Domain F. (Top left) Spatiotemporal area belonging to Domain F. The start point and the end point of Domain F in the continuous time are respectively the wave arrival time, t_{ij}^- , and the wave passage completion time, t_{ij}^+ ; the corresponding time steps, m_{ij}^- and m_{ij}^+ are respectively defined as the time steps enclosing t_{ij}^- and t_{ij}^+ . Note that the values of t_{ij}^\pm are precisely approximated in §4.3 related to ART. (Bottom left) Spatiotemporal configuration of time-shifted Domain F. The kernel is densely aligned to the spatial direction. The width in the temporal direction $m_{ij}^+ - m_{ij}^-$ is of $O(1)$. (Top right) A matrix structure representing source-receiver dependency made by the kernel temporally integrated over Domain F. The number of components in this matrix is of $O(N^2)$. (Bottom right) Schematic of an approximate (sub)matrix by H-matrices. The matrix representing the source and receiver dependency is separated into a vector representing the source dependency and a vector representing the receiver dependency. The number of elements to express the kernel is expected to be of almost $O(N)$. Precise procedure to apply H-matrices are detailed in §4.1.

Quantization (without FDPM) sparsely samples the kernel values in Domains I and S by enlarging the sampling interval as the elapsed time step m increases (Fig. 5, left panel). After the sampling, the original kernel is replaced with several step functions described by sparsely sampled values and sampling intervals (Fig. 5, right panel). The accuracy of the replacement is regulated by the relative error upper bound ϵ_Q (and that for the absolute error ϵ_{st}). As the elapsed time step increases, the sampling intervals gradually become sparse, since the temporal rate of change in the kernel decreases due to the proportional relation between the terms included in the kernel and the power of the elapsed time (detailed in §A).

In the time range using the same (q -th) sampling value \hat{K}_q , ($b_q \leq m < b_{q+1}$), a temporal convolution, $\sum_{m=b_q}^{b_{q+1}-1} K_m D_m$ becomes the product of \hat{K}_q and a slip \hat{D}_q :

$$\sum_{m=b_q}^{b_{q+1}-1} K_m D_m \rightarrow \hat{K}_q \sum_{m=b_q}^{b_{q+1}-1} D_m = \hat{K}_q \hat{D}_q, \quad (11)$$

where q is the quantization number, and we do not show the trivial suffixes. By storing this slip \hat{D}_q and updating \hat{D}_q by computing only the increment of \hat{D}_q at each time step, we

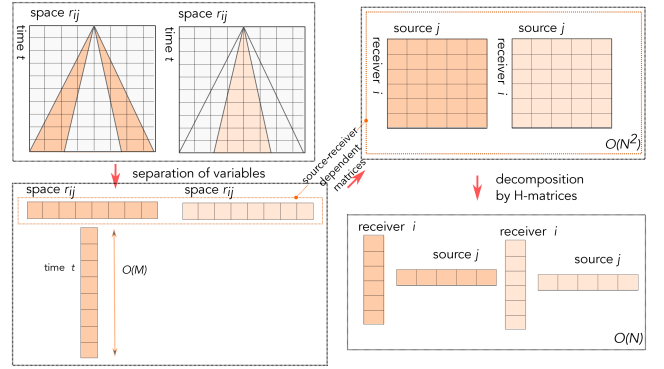


Fig. 4 Diagrams of the approximation procedure in Domains I and S. (Top left) Spatiotemporal area belonging to Domains I and S. (Bottom left) Spatiotemporal separation of the kernel by FDPM. The kernel in Domain I is separated into a matrix representing the space dependence and a vector representing the time dependence of the kernel. The kernel in Domain S is represented only by the space dependence by using a matrix. (Top right) Matrix structures representing the space dependencies of the kernels of Domains I and S. They are dense matrices, the numbers of whose elements are of $O(N^2)$. (Bottom right) Schematic diagram of the kernel approximated by H-matrices. The matrix representing the source and receiver dependency is separated into a vector representing the source dependency and a vector representing the receiver dependency. The number of elements to express the kernel becomes of almost $O(N)$.

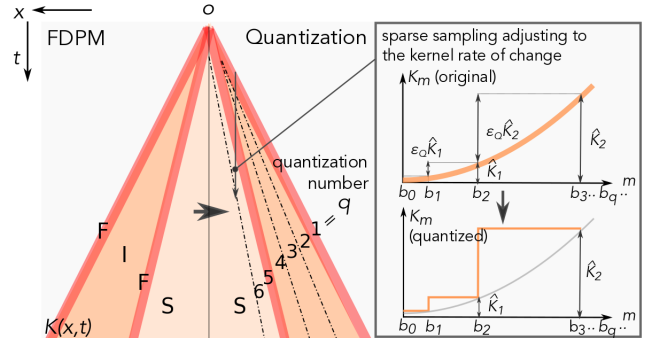


Fig. 5 Schematic of the quantization method (Quantization). (Left) Comparison between FDPM and Quantization. FDPM separates the integration area into Domains F, I, F, and S. Quantization divides the time range into multiple time segments based on given error conditions until the replacement of the kernel with the static term becomes possible. (Right) Quantization based on the relative error condition. The illustrated kernel corresponds to that in Domain I. The time range is divided so that the relative error between the kernel K and its representative value \hat{K} in each interval falls within ϵ_Q approximately. \hat{K} is K at the end of each sampling interval in the panel. The kernel within each interval is replaced by the representative value \hat{K} .

can make the temporal integration of the slip rate over the (q -th) time range unnecessary (detailed in §A.1). By quantizing the kernel and computing \hat{D}_q incrementally, Quantization makes the time complexity to convolve $\sum_{m=b_q}^{b_{q+1}-1} K_m D_m$ independent of the sampling interval ($b_{q+1} - b_q$). This situ-

ation is the same as Domain S in 3D problems whose kernel is time-independent.

The number of sampling becomes the logarithm of the temporal integration range to be quantized, as long as the time-dependent parts of the kernel are separated into power functions of time, like in the kernel in Domain I. The memory in FDP=H-matrices thus becomes safely of almost $O(N)$ by Quantization.

4 Approximations Used in FDP=H-matrices

The overview of the FDP=H-matrices were presented in §3. In this section, we derive the discretized form of the boundary integral equations and key approximations required for constructing the algorithm of FDP=H-matrices introduced later.

We first separate Eq (3) into the convolutions over Domains Fp, I, Fs, and S in continuous time. We focus on the convolution over Domain F(=Fp,Fs) (shown in Eq. (16)), since it contains the novel central idea of this study. The convolution over Domain F is approximated step by step and finally reduced to Eq. (33) in this section. See §B for the approximations applied to Domains I and S in an admissible leaf. The approximations applied to inadmissible leaves, only in 2D problems, are referred to in §D.

4.1 Procedure for Accurately Constructing Domain F Kernel

As introduced in §3.2.1, the kernel obeys the geometrical spreading along the wavefront. Here we detail the way to extract the spreading properties from the kernel of Domain F in order to apply H-matrices. Such extraction is introduced in order to avoid the accuracy deterioration in LRA of H-matrices, and plays a role in separating the temporally rapidly evolving part from the kernel.

A simple analytic expansion exemplifies the separation of the kernel (Fig. 6, top panel) into a smoothly geometrically spreading term and a rapidly evolving term. We here treat Green's function, $G(\mathbf{x}, t) = \delta(t - r/c)/(4\pi r)$, of the 3D wave equation ($\partial_t^2 G = c^{-2}(\nabla \cdot \nabla)G + \delta(t)\delta(r)$) in an infinite homogeneous isotropic medium, where $\delta(\cdot)$ represents the Dirac δ function. The geometrically spreading part ($1/4\pi r$ in G) is approximated by H-matrices efficiently, as done to the spatial BIEM kernel. The rapidly time-evolving part ($\delta(t - r/c)$ in G) exactly becomes $\int \delta(t - r/c)dt|_{r=ct} = 1$ after integrated near $t = r/c$ (that is represented by the multiplication of the infinitesimal time dt to G). With the infinitesimally small time dt , Gdt may be compared with an impulse, the time integral of a temporally varying force. The geometrically spreading part can be regarded as the impulse of the stress response. By considering the geometri-

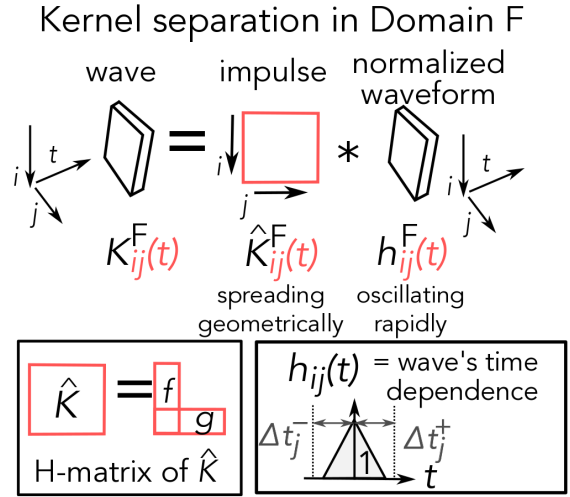


Fig. 6 Diagram representing the kernel separation in Domain F. (Top) Analogy of the kernel separation. The kernel ($K_{ij}(t)$) (corresponding to a wave) is separated into its geometrically spreading part ($\hat{K}_{ij}(t)$) (corresponding to an impulse) and its time oscillating part ($h_{ij}(t)$) (called the normalized waveform) for each source i and receiver j over time t . (Bottom left) H-matrices applied to \hat{K} (whose ij component is \hat{K}_{ij}). \hat{K} is geometrically spreading and is well approximated H-matrices. (Bottom right) Dynamic behaviors of the normalized waveform. It represents the time dependence of the kernel (the wave). Its time integral is set at 1. The area where the normalized waveform takes nonzero values is enclosed in Domain F.

cally spreading part and rapidly time-evolving part in such different ways, we expand G in the vicinity of the reference point \mathbf{x}_0 , as

$$G(\mathbf{x}, t)|_{r=ct} = G(\mathbf{x}_0, t)dt|_{|\mathbf{x}_0|=ct}(1 + O(|\mathbf{x} - \mathbf{x}_0|/r)). \quad (12)$$

These features are generally kept after discretization although the delta-function is modulated into more oscillatory functions due to the finiteness of the source sizes. Like an impulse Gdt , we introduce the time integral of the kernel (\hat{K} , called the amplitude term) over Domain F (= F_p, F_s):

$$\hat{K}_{i,j}^F := \int dt K_{i,j}^F(t). \quad (13)$$

It is important that, while the original discretized kernel $K_{i,j}^F(t)$ rapidly oscillates over time (t) and space (i and j), the time integral $\hat{K}_{i,j}^F$ is smooth over space as the kernel of spatial BIEM. Thus the matrix \hat{K}^F whose ij components is $\hat{K}_{i,j}^F$ is efficiently approximated by H-matrices as

$$\hat{K}^F \simeq \sum_a \sum_l \mathbf{f}_{al}^F \otimes \mathbf{g}_{al}^F. \quad (14)$$

This approximation corresponds to the expansion along the wavefront in Domain F (Fig. 6, left panel). The rank of the approximated kernel is expected to be of $O(1)$. Accompanying the amplitude term \hat{K}^F , the normalized kernel h^F is defined as

$$h_{ij}^F(t) := K_{i,j}^F(t + t_{ij}^c)/\hat{K}_{i,j}^F. \quad (15)$$

where the time origin of $h_{ij}^F(t)$ is shifted by t_{ij}^c from that of $K(t)$. We call $h_{ij}^F(t)$ the normalized waveform. The normalized waveform fulfills the normalization condition $\int dt h_{ij}^F(t) = 1$ and describes the time dependence of the kernel (Fig. 6, bottom right panel). Note that the time origin of the normalized waveform is shifted by the travel time from that of the kernel, in order for preparing the approximations of ART shown in §4.2. The maximum duration for h_{ij} to take non-zero value corresponds to the duration of Domain F, $\Delta t_j^+ + \Delta t_j^-$ for a receiver j .

After LRA of \hat{K} , the stress response of Domain F denoted by $T_i^F(t)$ at the location of the receiver i at time t , is expressed as

$$T_i^F(t) := \sum_j K_{i,j}^F * D_j \approx f_i^F \sum_j g_j^F h_{ij}^F * D_j, \quad (16)$$

where $*$ denotes the temporal convolution and we omitted the rank numbers from f_i, g_j for simple presentation.

The separation of the remaining i and j dependences of $h_{ij}^F(t)$ is further required for the efficient computation. Since $h_{ij}^F(t)$ is a rapidly oscillating function over space and time, we treat it another way than LRA techniques for the smooth functions in H-matrices, in the next §4.2.

4.2 Averaged Reduced Time (ART)

Some variables in Eq. (16) still depend on both the source and receiver. They can be observed from the explicitly rewritten form of the temporal convolution;

$$T_i^F(t) = f_i^F \sum_j g_j^F \int_{-\Delta t_j^-}^{\Delta t_j^+} d\tau h_{ij}^F(\tau) D_j(t - t_{ij} - \tau). \quad (17)$$

where the superscript c in $\Delta t_j^{c\pm}$ of FDPM is abbreviated hereafter as in t_{ij} . In addition to h_{ij}^F , the travel time t_{ij} (defined in Eq. (5) to set the temporal range of Domain F) is also shown to depend on both the receiver i and source j . Such source and receiver dependencies are separated by the approximations of ART in order to achieve almost $\mathcal{O}(N)$ costs.

Below, we first show the approximation process of ART in §4.2.1. Subsequently, two schemes with different accuracies are proposed in §4.2.2.

4.2.1 Plane Wave Approximation and Clustering of Elements

The receiver (i) source (j) dependencies of t_{ij} and h_{ij}^F in Eq. (17) are approximately separated by ART. Below, the approximations of ART are first geometrically explained (Fig. 7, left panel). Second, variables concerning the approximation are expressed based on the clustering of H-matrices.

Fig. 7 (left) shows a set of the interactions between sources and receivers corresponding to the kernel of Domain F describing the waves radiated from the sources propagating to

the receivers. Sources and receivers, illustrated in the figure, correspond to a certain pair of a source cluster and a receiver cluster considered in H-matrices. Below, the set of the interactions is approximated by ART, which is based on a property of the wave propagation, depending on the ratio of the (source and receiver) cluster diameters to the (source-receiver) cluster distance.

When the receiver and source clusters are close compared to the cluster diameters, it is clearly observed that both t_{ij} and h_{ij} depend on the locations of receiver i and source j (close cluster in Fig. 7 (left)). The receiver i and the source j dependence of the travel time t_{ij} is geometrically illustrated as the source-receiver distance r_{ij} after multiplied by the wave speed c . The source-receiver distance r_{ij} obviously depends on the source j and receiver i . The receiver i and the source j dependence of the normalized waveform h_{ij}^F is expressed in the finite duration of the wavefront where h_{ij}^F takes nonzero values (Fig. 7 (left)). The wavefront duration (the varying width (divided by c) of the circles) depends on the relative orientation of the source element j from the receiver point i .

These i and j dependencies of t_{ij} and h_{ij} are asymptotically separated at a large distance compared with the diameters of the source cluster and receiver cluster (distant cluster in Fig. 7 (left)) because the wavefront becomes flat approximately as the source and the receiver separated each other. It is known as the plane wave approximation [26]. As the wavefront becomes flat, the width of the wavefront becomes independent of the receiver locations. Hence, the normalized waveform h_{ij}^F loses the receiver i dependence, and is expressed by that for the representative i_* of the neighboring receivers:

$$h_{ij}^F(\tau) \approx h_j^F(\tau) := h_{i_*j}^F(\tau). \quad (18)$$

We call the asymptotic function h_j^F the degenerating normalized waveform in FDP=H-matrices. Besides, the ray paths connecting the sources and receivers degenerate to one straight line connecting i_* and the representative j_* of the neighboring sources (the thick arrow in Fig. 7). We call it the degenerating ray path (DRP). By projecting the relative locations of the sources and receivers to DRP, ART separates the receiver-source dependence of the travel time. Consequently, the travel time is separated to be

$$t_{ij} \approx \delta t_i + \bar{t}_j \quad (19)$$

where $\bar{t}_j (= cr_{i_*j})$ describes the travel time from the source j to a certain representative receiver point i_* , and $\delta t_i (= \mathbf{x}_{i_*}/c \cdot \mathbf{x}_{i_*j_*}/r_{i_*j_*})$ describes the travel time for the distance of the receiver i from the representative one i_* projected onto DRP. We call \bar{t}_j the receiver-averaged travel time and δt_i the receiver-dependent travel time difference. As shown below, the distance δr orthogonal to DRP, related to the error of the plane wave approximation, becomes much smaller than

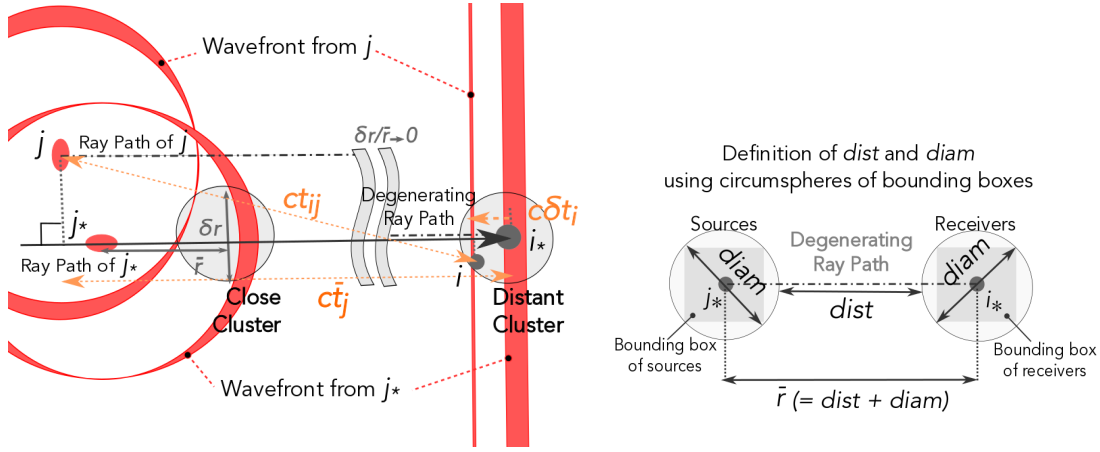


Fig. 7 Outline of ART. (Left) Diagram to illustrate the plane wave approximation. An admissible leaf and its Domain F interaction (a set of wavefronts) are described. After multiplied by the wave speed c , the distance of the collocation points of the receiver i and source j and the wavefront width respectively correspond to the (collocation point) travel time t_{ij} and the duration (the range of t) where the normalized waveform $h_{ij}(t)$ takes nonzero values. Both are receiver and source dependent in the case of two close clusters. On the other hand, in the case of two distant clusters, the wavefront becomes flat and the width becomes independent of the receiver i . The ray paths (lines perpendicular to the wavefronts) also become independent of the receivers and sources, and degenerate to a ray path connecting the representative source j_* to the representative receiver i_* (degenerating ray path). Based on the relative position of the receiver from the source projected onto the degenerating ray path, the source-receiver dependence of the travel time is separated; after the separation, the travel time multiplied by the wave speed c is approximately represented by the magnitude of the sum of a vector from j to i_* (the receiver-averaged travel time \bar{t}_j multiplied by c) and a vector from i_* to i (the receiver-dependent travel time difference δt_i multiplied by c). The approximation errors of them are represented by the ratio of the cluster size δr (vertical to the degenerating ray path) to the distance \bar{r} between source-receiver representatives (i_* and j_*). (Right) Parameters to evaluate the approximation errors of ART. The maximum diagonal length of a bounding box (plus the maximum length of the discretized elements enclosed in two bounding boxes, not illustrated) is used as $diam$ of H-matrices; $diam$ defined in this rule is the upper bound of the maximum distance of two points located on the boundary region occupied by the source (receiver) elements. The center distance of circumscribed spheres minus $diam$ is used as $dist$ of H-matrices; $dist$ defined in this way is actually the lower bound of the bounding box distance, which is the ordinary definition of $dist$ [19]. Representatives i_* and j_* are set at the centers of the clusters and their distance \bar{r} satisfies $diam = \bar{r} - dist$ and gives a relation $\delta r/\bar{r} < 1/(1+1/\eta)$.

the source-receiver distance in the case of sufficiently distant clusters.

The approximations of ART and the representative points of the source and receiver clusters (i_* , j_*) are defined based on the clustering of H-matrices (Fig. 7 (right)). The clustering and parameterization of ART is carried out by using bounding boxes [19] in this paper. We initially set a cuboid so as to enclose all the collocation points of boundary elements. The cuboid is partitioned sequentially by equally dividing their longest two sides. Each cuboid makes a subset of boundary elements whose collocation points are enclosed in the RP. To the pair of cuboids divided the same times (squares in Fig. 7 (right)), $diam$ and $dist$ of H-matrices are defined. The value of $diam$ is given as the maximum diagonal length of cuboids plus the maximum length of the boundary elements enclosed in the cuboids. (Note that the maximum diagonal lengths of cuboids at the same levels (which are cuboids divided the same times) are the same, as shown in Fig. 7.) The value of $dist$ is given as the distance \bar{r} between the centers of the source and receiver RPs subtracted by $diam$ ($dist = \bar{r} - diam$) (See Fig. 7 (right)). Last, the representative points i_* and j_* are respectively set at the centers of the receiver and source cuboids. The above

variables are defined to respective admissible leaves. ART is not applied to inadmissible leaves, which contains close (i, j) pairs (See §C).

These definitions of $diam$ and $dist$ are respectively the upper bound of $diam$ and lower bound of $dist$ in the ordinary definitions without the boundary discretization. (Ordinarily, $diam$ is defined as the longest distance of two points on the boundaries enclosed in each RP, and the maximum between the $diam$ values of source and receiver clusters is used as $diam$ for the block cluster; $dist$ is defined as the shortest distance of two points on the boundaries enclosed in the source and receiver RPs [19].) Therefore, the ordinary admissibility and inadmissibility conditions are satisfied when the admissibility condition we provide (detailed in §4.2.2) is satisfied.

Substituting Eqs. (18) and (19) to Eq. (17), we obtain

$$T_i^F(t + \delta t_i) \approx f_i^F \sum_j g_j^F \int_{-\Delta t_j^-}^{\Delta t_j^+} d\tau h_j^F(\tau) D_j(t - \bar{t}_j - \tau). \quad (20)$$

The source and receiver dependencies are fully separated in this convolution. After temporally discretized in §4.3, this enables us to construct an almost $O(N)$ arithmetic for Domain F, described in §5.

We next detail the approximation errors. Under the above definitions of $(diam, dist, i_*, j_*)$, the travel time separation in an admissible leaf is given by the expansion in the vicinity of the receiver-averaged travel time as

$$t_{ij} = \delta t_i + \bar{t}_j + O\left((1 + 1/\eta)^{-2} dist\right) \quad (21)$$

with

$$\delta t_i := (r_{i,j_*} - r_{i,j_*})/c \quad (22)$$

$$\bar{t}_j := r_{i_*,j}/c. \quad (23)$$

We used a relation $diam/dist < \eta$ (See §2.3). The definition of δt_i in Eq. (22) is a bit changed from $\delta t_i = \mathbf{x}_{i,i_*}/c \cdot \mathbf{x}_{i_*,j_*}/r_{i_*,j_*}$ for better accuracy of Eq. (21); the definitions of δt_i and \bar{t}_j may be changed for the simplification of the arithmetics, as explained in §4.3.2 and §B.2.5. $O(N^{3/2} + NL')$ in the constant $\eta^2 dist$ scheme. By neglecting the higher order term in Eq. (21), we can separate the travel time as $t_{ij} \approx \delta t_i + \bar{t}_j$ with ART.

The magnitude of the error involved by neglecting the second order of $diam/(dist + diam)$ corresponds to the cluster diameter δr (and is of $O((\delta r)^2/\bar{r})$) in the direction perpendicular to DRP in Fig. 7 (left). The ratio of the cluster diameter ($diam$) to the distance between cluster centers ($\bar{r} = dist + diam$) is bounded by $(1 + \eta^{-1})^{-1}$ in the error evaluation ($diam/(dist + diam) < (1 + \eta^{-1})^{-1}$). More careful evaluation of the travel time error is described next in §4.2.2.

The normalized waveform is approximated analytically in an admissible leaf and the error of Eq. (18) is as small as the variation in the wavefront width of $O((1 + \eta^{-1})^{-1})$ in a receiver cluster (as long as the kernel is defined for the stress, that is not for the traction, as detailed in §E.1). In the temporal convolution of Eq. (17), additionally, the error of Eq. (18) becomes also on the order of the time variations in the slip rates $\partial_t D_j(\Delta t_j^- + \Delta t_j^+)$ over the time range $(\Delta t_j^- + \Delta t_j^+)$ (defined in Eqs. (6) and (7)) of the convolution in Domain F. This is because the time integral of the normalized waveform is set unity (Eq. (15)). Based on the above two order estimates, the approximation error of the convolution of the normalized waveform and the slip rate is evaluated as

$$\begin{aligned} & \int_{-\Delta t_j^-}^{\Delta t_j^+} d\tau h_{ij}^F(\tau) D_j(t - \tau - t_{ij}) \\ &= \int_{-\Delta t_j^-}^{\Delta t_j^+} d\tau h_{ij}^F(\tau) D_j(t - \tau - t_{ij}) \\ &+ O[(1 + \eta^{-1})^{-1} \partial_t D_j(\Delta t_j^- + \Delta t_j^+)]. \end{aligned} \quad (24)$$

4.2.2 Two Admissibility Conditions Proper for Travel Time Separation

We approximated t_{ij} and h_{ij} in §4.2.1, but the error of t_{ij} in Eq. (21) is of $O((1 + \eta^{-1})^{-2} dist)$ and diverges when $dist \rightarrow \infty$ in constant η cases, so that more careful evaluation on

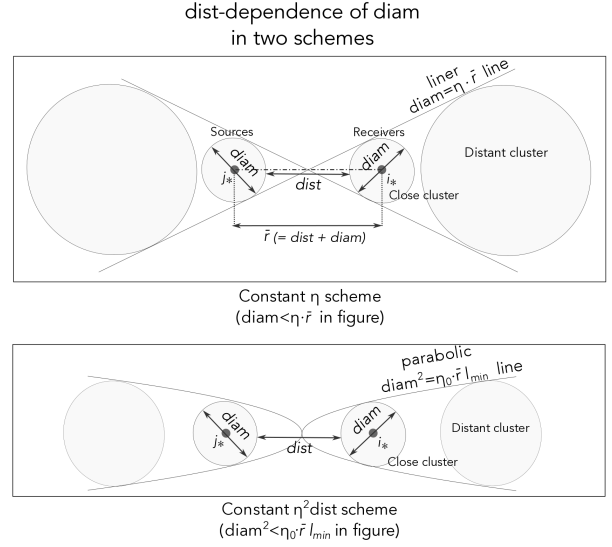


Fig. 8 Scheme dependence of η , where $dist$ is replaced with \bar{r} for simple explanation. (Top panel) Constant η scheme, where the lower bound of $dist$ is a linear function of $diam$. (Bottom panel) Constant $\eta^2 dist$ scheme, where the lower bound of $dist$ becomes a parabolic function of $diam$.

the error is required on the travel time separation, Eq. (21). Based on the characterization of the error caused by the travel time separation, two schemes of FDP=H-matrices are developed. These are expressed by two admissibility conditions of H-matrices (illustrated in Fig. 8), and are called the constant η scheme and the constant $\eta^2 dist$ scheme. Note that all the order estimates except here is for the constant η scheme.

Constant η Scheme We refer to the condition keeping η constant as the constant η scheme. The constant η scheme corresponds to the admissibility condition ordinarily adopted in H-matrices [19]. The constant η scheme achieves the almost $O(N)$ costs, as later shown in §6.

In the constant η scheme, the error of using Eq. (21) is evaluated by the effective wave speed c_{ij} , introduced as

$$c_{ij} := r_{ij}/(\delta t_i + \bar{t}_j) \quad (25)$$

to each pair of a receiver i and a source j . The constant η scheme keeps $diam/dist$ of $O(\eta)$ regardless of the $dist$ value (Fig. 8, top panel). Consequently, the order of the error of an effective speed, that is the ratio of the distance to the travel time error in Eq. (21) of $O((1 + \eta^{-1})^{-2} dist)$, is kept finite without divergence. The error of the effective wave speed is shown to be

$$|c_{ij}/c - 1| < \frac{1}{4}(1 + \eta^{-1})^{-2} + O((1 + \eta^{-1})^{-3}), \quad (26)$$

where c denotes the un-approximated wave speed. Eq. (26) is obtained by the comparison of Eq. (21) with the summation of Eqs. (22) and (23) with the perturbation concerning

$1/(1 + 1/\eta)$. Based on the error estimate of Eq. (26), the use of Eq. (21) in the constant η scheme is regarded as an approximation ignoring the wave speed error of $O((1 + \eta^{-1})^{-2})$.

It might be worth mentioning that the dispersity (wave-length dependence) of the effective wave speed is negligible in the constant η scheme. The wave speed approximation has been well verified in volume-based methods applied to elastodynamic problems [14,30], even where the acoustic speed is dispersive by depending on the wavelength and the Courant-Friedrichs-Lewy (CFL) parameter [31]. In the constant η scheme of FDP=H-matrices, the wave speed error shown in Eq. (26) is just depending on η but independent of $dist$, meaning negligible dispersity. This negligible dispersity in the constant η scheme is examined numerically in §6.3.2.

Constant $\eta^2 dist$ Scheme We refer to the condition keeping $\eta^2 dist$ constant as the constant $\eta^2 dist$ scheme. The constant $\eta^2 dist$ scheme is given by an admissibility condition:

$$diam < \sqrt{\eta_0 l_{min} dist}, \quad (27)$$

where η_0 is the maximum value of η bounding the ratio $diam/dist$ ($diam/dist < \eta := \sqrt{\eta_0 l_{min}/dist}$). The value of η is maximized ($\eta = \eta_0$, $diam < \eta_0 dist$) when the value of $diam$ is its minimum in admissible leaves, $diam = l_{min}$. The total computation cost of the constant $\eta^2 dist$ scheme is estimated to be of almost $O(N^{3/2})$, as considered in the next (Fig. 9).

The constant $\eta^2 dist$ scheme (Eq. (27)) keeps the travel time error of $O((1 + 1/\eta)^{-2} dist)$ in Eq. (21) constant. This is because η decreases in inverse proportion to the square root of $dist$ ($\eta \propto 1/\sqrt{dist}$). Geometrically, $dist$ is roughly proportional to square of $diam$ (Fig. 8, bottom panel). The travel time error in the constant $\eta^2 dist$ scheme is evaluated as

$$|\delta t_i + \bar{t}_j - t_{ij}| < \frac{1}{4} \eta_0 l_{min}/c + \dots \quad (28)$$

This is obtained by the substitution of $\eta = \sqrt{\eta_0 l_{min}/dist}$ ($\leq \eta_0$) to the inequality Eq. (26) for the constant η scheme. The higher order term in Eq. (28) is of $O((1 + 1/\eta)^{-3})$ as in Eq. (26). Eq. (28) shows the independence of the travel time error from $dist$ in the lowest order term.

The accuracy of the constant $\eta^2 dist$ scheme is characterized by the following three features. First, the constant $\eta^2 dist$ scheme introduces the characteristic length of the travel-time error, $\delta x := \eta_0 l_{min}/4$ (See Eq. (28)). When $\delta x \leq \Delta x_j/2$ for any sources j , the travel time error of ART becomes smaller than that caused by the spatial stress collocation (defined in §2.1). Second, the travel time approximation in this scheme appearing in the temporal convolution in Eq. (24) is regarded as an approximate time shift by $\delta x/c$ in convolved slip-rates. The resulting error is of $O(\partial_t D \delta x/c)$.

Third, the constant $\eta^2 dist$ scheme decreases the approximation error of h of $(1 + \eta^{-1})^{-1}$ in Eq. (24). The decreased error of h is estimated to be of $O((1 + \eta^{-1})^{-1}) \sim O(1/\sqrt{dist})$ when $\eta \ll 1$.

Typical Costs of Two Schemes We proposed the constant η and constant $\eta^2 dist$ scheme by changing η of the admissibility conditions. Finally, we test N dependencies of their numerical costs for typical elastodynamic problems by constructing the block cluster tree (the structure to divide the kernel matrix, detailed in §2.3).

As long as LRA satisfactory works to reduce the rank of the kernel in each block cluster to be of $O(1)$, the numerical cost order concerning N is independent from the concrete form of the kernel. Therefore, we here do not specify the kernel, and check only the block cluster tree for given distributions of boundary elements. More careful evaluation by considering the original kernel is shown in §6.1.1 and §6.3 in terms of both the rank and accuracy.

Since the spatial integration and temporal integration is fully separated in an admissible leaf in FDP=H-matrices, the typical (rank-independent) costs for admissible leaves are characterized by the costs of time integration and the spatial integration. Both are characterized by the lengths of the integral. The spatial costs then correspond to the sum of boundary elements ($\sum(N_f + N_r)$) (representing the sum of spatial lengths) in admissible leaves, where N_f and N_r respectively denote the number of sources and that of receivers. The temporal costs the sum of \bar{r} (representing the sum of temporal lengths), $\sum \bar{r}$ (on the order of $\sum dist$) in admissible leaves. The costs of inadmissible leaves is of $O(N)$ (after the temporal approximation described in §C) and so we do not treat them here. Two sums $\sum(N_f + N_r)$ and $\sum \bar{r}$ in admissible leaves, expected to be of almost $O(N)$ in the constant η scheme, determine the leading order of the costs of FDP=H-matrices concerning N and M , as long as the rank of the approximated kernel is of $O(1)$.

We here do not consider M dependence of the cost, since the time integration range can be suppressed on the order of $O(N)$ or below. This is due to a property of FDPM where the length of the temporal integration is reduced to be on the order of $L/(\beta \Delta t) = O(N^{1/D_b}) \leq O(N)$ even for large $M \geq L/(\beta \Delta t)$.

Throughout this cost evaluation, we adopted the following ways to set the arrangement of the boundary elements and the admissibility condition. To clarify the dimension dependence of the block cluster tree, we studied one and two dimensional boundary geometries: one-dimensional (1D) arrangement of linearly aligned elements and 2D arrangement of elements randomly and uniformly dispersed in a square. We here use $diam < \eta \bar{r}$ and $diam < \sqrt{\eta_0 l_{min} \bar{r}}$ ($\bar{r} := dist + diam$) instead of Eqs. (8) and (27) as alternatives respectively of the constant η scheme and constant $\eta^2 dist$ scheme.

These changes are in order to rapidly check the asymptotic size dependence of the cost indicators ($\sum(N_f + N_r)$, $\sum \bar{r}$). These changes does not affect the general cost scaling.

Fig. 9 (left) shows the obtained submatrix distribution of the H-matrices, where D_b denotes the fault dimension. The block cluster trees of the constant η scheme simply showed fractal sieves in both dimensions. The block cluster trees of the constant $\eta^2 \text{dist}$ scheme showed a linear form in the 1D fault arrangement and a quite scattered form in the 2D fault arrangement.

Fig. 9 (right) shows the cost indicators of admissible leaves, $\sum(N_f + N_r)$ and $\sum \bar{r}$. In the constant η scheme cases, the cost is shown to be of almost $O(N)$. The cost indicator $\sum(N_f + N_r)$ of the spatial integration is on the same order of H-matrices in the spatial BIEM. The cost indicator $\sum \bar{r}$ of the temporal integration is also of almost $O(N)$. This is natural since dist/diam is roughly a constant of $O(\eta)$. In the constant $\eta^2 \text{dist}$ scheme cases, $\sum(N_f + N_r)$ and $\sum \bar{r}$ were respectively shown to be of almost $O(N^{3/2})$ and $O(NL)$, where L is the characteristic length of the system. These scalings are consistent with scale analysis results shown in §E.2. Total of them means almost $O(N^{3/2})$ costs of the constant $\eta^2 \text{dist}$ scheme in 2D and 3D problems where the constant $\eta^2 \text{dist}$ scheme can be required to deal with the travel time separation errors. 1D is a special case where $t_{ij} = \delta t_i + \bar{t}_j$ is exactly met, as supplemented in §6.1.2.

4.3 Temporal Discretization of Stress Response Integrated over Domain F

Eq. (20) is obtained by the analytic approximations of ART separating the source receiver dependencies of the travel time and normalized waveforms. We here temporally discretize Eq. (20) that contains the continuous time shifts in the collocated stress by $(t + \delta t_i)$ and in the convolved slip rate by $(t - \bar{t}_j - \tau)$. In §4.3.1, we temporally discretize the right hand side of Eq. (20), based on the piecewise-constant temporal interpolation of the slip rate. In §4.3.2, we treat δt_i (the receiver-dependent travel time difference) as the correction factor of the time collocation point.

We hereafter suppose $D_j(t)$ is interpolated as $D_j(t) = \sum_m D_{j,m} [H(m\Delta t) - H((m+1)\Delta t)]$ and the stress collocation time (in Eq. (20)) is located at $t = (n+1)\Delta t$ for each time step n . A shift of the collocation time from $(n+1)\Delta t$ to $(n+\epsilon_t)\Delta t$ is dealt with by changing δt_i to $\delta t_i + (\epsilon_t - 1)\Delta t$ for a given constant ϵ_t , which is ordinarily supposed to satisfy $0 < \epsilon_t < 1$ [28].

4.3.1 Temporal Discretization of the Kernel after Travel Time Separation in Continuous Time

The time range in Eq. (20) to convolve the slip rate is shifted by \bar{t}_j from the original time range in Eq. (4) (as $D_j(t - \tau) \rightarrow$

$D_j(t - \bar{t}_j - \tau)$). This time shift in the slip rate is dealt with in the discretization process of the time definition range of Domain F. This time shift also affects the amplitude term \hat{K} defined in the continuous time, as later added.

The temporal discretization procedure is summarized as follows (See §E.3 for the detail). To show the result, we first define some quantities. Δt_j^\pm are given by Eqs. (6) and (7) as in FDPM (or more simply $\Delta t_j^\pm = \Delta x_j / (2c)$), which are rather arbitrary, as long as $\Delta t_j^\pm \geq \Delta x_j / (2c)$ as in FDPM. Then we define $\bar{t}_j^\pm = \bar{t}_j \pm \Delta t_j^\pm$, which are respectively the (continuous) time of the wave arrival and wave passage completion (when $\bar{t}_j = cr_{i^*j}$); $\lfloor \cdot \rfloor$ and $\lceil \cdot \rceil$ respectively denote the floor and ceiling functions. Last, corresponding discretizations, $\bar{m}_j^- := \lfloor \bar{t}_j^- / \Delta t \rfloor$ and $\Delta m_j := \lceil \bar{t}_j^+ / \Delta t \rceil - \bar{m}_j^-$ are defined. \bar{m}_j^- and $\bar{m}_j^- + \Delta m_j + 1$ are respectively defined as time steps experiencing the wave arrival and the wave passage completion for the source j and receiver i^* . Δm_j is the time step width of Domain F in FDP=H-matrices. Note that \bar{m}_j^- , Δm_j inherit the c -dependence abbreviated, from \bar{t}_j^\pm .

Next, substituting $t = (n+1)\Delta t$, $D_j(t) = \sum_m D_{j,m} [H(m\Delta t) - H((m+1)\Delta t)]$ to Eq. (20), we obtain

$$T_i^F((n+1)\Delta t + \delta t_i) \approx f_i^F \sum_j g_j^F \sum_{m=0}^{\Delta m_j - 1} h_{j,m}^F D_{j,n-(m+\bar{m}_j^-)}, \quad (29)$$

with

$$h_{j,m}^F := \frac{1}{\hat{K}_{i^*,j}^F} \int_{\max[(m+\bar{m}_j^-)\Delta t + (t_{i^*,j} - \bar{t}_j), \bar{t}_{i^*,j}^-]}^{\min[(m+1+\bar{m}_j^-)\Delta t + (t_{i^*,j} - \bar{t}_j), \bar{t}_{i^*,j}^+]} d\tau K_{i^*,j}(\tau). \quad (30)$$

The term $h_{j,m}$ is the temporally discretized form of the normalized waveform (given by Eq. (14)). Eq. (30) holds in general cases even when the difference is introduced between \bar{t}_j and $t_{i^*,j}$, related to §B.5; this definition of the normalized waveform can be further simplified by using the arbitrariness of Δt_j^\pm (detailed in §E.3).

The amplitude term \hat{K}^F defined by Eq. (14) is explicitly given as

$$\hat{K}_{i^*,j}^F = \int_{-\Delta t_j^-}^{\Delta t_j^+} d\tau K_{i^*,j}(\tau + t_{ij}). \quad (31)$$

The integral solutions of Eqs. (31) and (30) are already obtained for both 2D [28] and 3D [23] problems and we can use already obtained analytic constituent functions of kernels describing the response to the Heaviside function.

4.3.2 Time Shift of the Collocation Point for Evaluating the Stress Response of Domain F

The left hand side of the continuous time BIE (Eq. (29)) is to evaluate the stress in continuous time. For example, when we select $t = (n+1)\Delta t$, the left hand side is the stress of the continuous time $T_i((n+1)\Delta t + \delta t_i)$.

Below, it is connected to the stress of discretized time step n , $T_i((n+1)\Delta t)$. The simplest approximation is to use

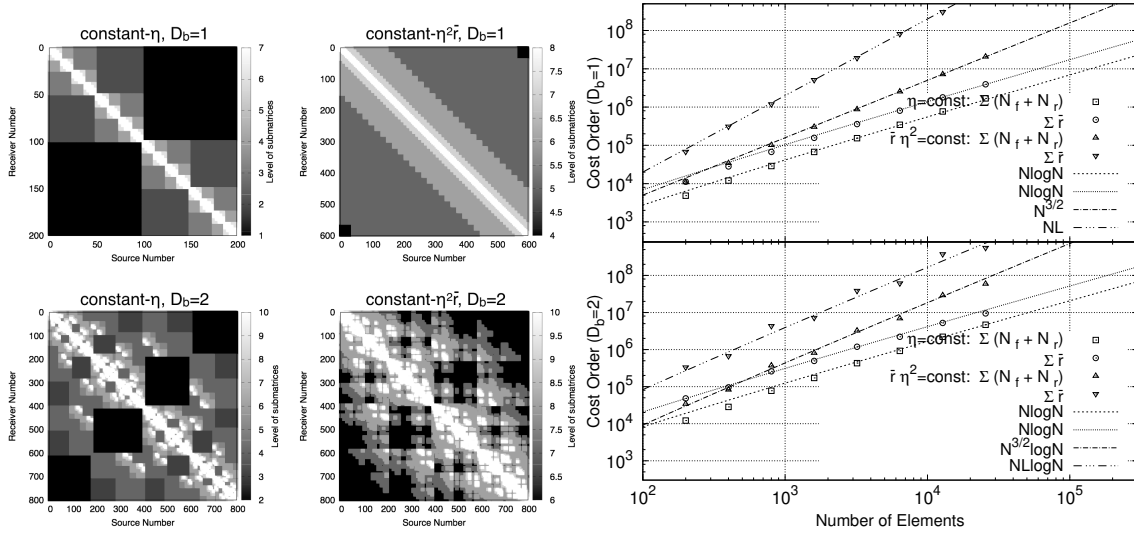


Fig. 9 Scheme dependence of the submatrix distribution and the numerical cost estimates of FDP=H-matrices. One-dimensional (1D) fault arrangement of linearly aligned elements and 2D fault arrangement of elements randomly and uniformly dispersed in a square with the number density per area $N/(L/(\Delta x/2))^2 = 0.08$, where L is the length of the sides of the square. In the panels, D_b denotes the fault dimension. (Left) Submatrix distributions of H-matrices. The specified scheme and dimension are written in the panel. The axes express the assigned element numbers. The color bar represents the number of rectangle division to get the corresponding rectangle (the level, which is different from the rank of LRA shown in §6.1.1). Parameter values of H-matrices are set at $(\eta_0, l_{min}/\Delta x) = (1, 5)$ for the 1D fault arrangement in the constant η scheme and $(0.85, 2.5)$ for the others. (Right) Typical numerical cost estimates of admissible leaves. Top and bottom graphs respectively show the results of 1D and 2D fault arrangements. See §4.2.2 for the definitions of the variables. Conditions are the same as the left panel except parameters of H-matrices set at $(\eta_0, l_{min}/\Delta x) = (0.85, 5)$.

an appropriate discretized time step δm_i (called the receiver-dependent travel time step difference). The discretized time step δm_i discontinuously approximate continuous-time receiver-dependent travel time difference δt_i , and gives $T_{i,n+\delta m_i} = T_i((n+1+\delta m_i)\Delta t) \approx T_i((n+1)\Delta t + \delta t_i)$. The δm_i value corresponds to the integer part of $\delta t_i/\Delta t$:

$$\delta m_i = \lfloor \delta t_i/\Delta t \rfloor. \quad (32)$$

The discarded $O(\Delta t)$ travel time error by this approximation is regarded as a small fraction in the travel time separation in Eq. (21), which means using $\delta t_i = \lfloor (r_{i,j_s} - r_{i,j_r})/\Delta t \rfloor \Delta t$ instead of Eq. (21); it is satisfactory for the constant η scheme, since $O(\Delta t)$ change in the travel time separation is negligible in the error of the effective wave speed (26). Consequently, we obtained fully discretized form of Eq. (29) given as

$$T_{i,n+\delta m_i}^F \approx f_i^F \sum_j g_j^F \sum_{m=0}^{\Delta m_j-1} h_{j,m}^F D_{j,n-(m+\bar{m}_j^-)}. \quad (33)$$

The rounding condition is largely arbitrary. For example, although we adopted the rounding-down in (32), rounding-off may help to avoid the systematic errors in approximating the travel time in some cases. More accurate time interpolation is given by $T_i((n+1+\delta m_i)\Delta t) \approx T_i((n+1)\Delta t + \delta t_i)(1 - \delta t'_i/\Delta t) + T_i(n\Delta t + \delta t_i)\delta t'_i/\Delta t$, where $\delta t'_i/\Delta t$ is the decimal part of $\delta t_i/\Delta t$. When this higher order interpolation is used, the error is of $O(\partial_t^2 T_i(\Delta t)^2)$. These interpolations are related to the aliasing errors concerning the initial spatiotemporal

discretization, we here adopted rather stable rounding-down condition; it is out of the scope in this study to comprehensively study the properties of those interpolations.

5 Arithmetics of FDP=H-matrices in Domain F

The stress response (Eq. (16)) of Domain F is reduced to Eq. (33) in §4, to separate the source and receiver dependencies in the variables contained in the convolution. The arithmetic to compute Eq. (33) is here explained. First, we decompose Eq. (33) into three formulae (§5.1) representing three processes independent of one another. Second, we explain an almost $O(N)$ arithmetic to compute these formulae (§5.2).

5.1 Three Independent Formulae to Evaluate the Stress Response of Domain F in FDP=H-matrices

Eq. (33) of Domain F is here decomposed into three simple formulae. First, we introduce the convolution of D and h_j^F :

$$\hat{D}_{j,n}^F := \sum_{m=0}^{\Delta m_j-1} h_{j,m}^F D_{j,n-m}. \quad (34)$$

This is the first formula of FDP=H-matrices, converting D to \hat{D}^F , which is independent of i . By using \hat{D}^F , we simplify

Eq. (33) to

$$T_{i,n+\delta m_i}^F \approx f_i^F \sum_j g_j^F \hat{D}_{j,n-\bar{m}_j}^F. \quad (35)$$

Eq. (35) can be comparable to the formula $\mathbf{T} = \mathbf{K}\mathbf{E} \approx \mathbf{f}[\mathbf{g} \cdot \mathbf{E}]$ of H-matrices in static problems (Fig. 10, top panel), further decomposed into two formulae. In H-matrices, as detailed in §2.3, $\mathbf{T} \approx \mathbf{f}[\mathbf{g} \cdot \mathbf{E}]$ is separated into receiver-independent computation $\bar{\mathbf{T}} := [\mathbf{g} \cdot \mathbf{E}]$ and source-independent computation $\mathbf{T} \approx \mathbf{f}\bar{\mathbf{T}}$. The scalar \bar{T} in H-matrices can be regarded as the stress at the reference receiver position. Note that \bar{T} is given to each rank and each admissible leaf. In FDP=H-matrices, we call \bar{T} the reference stress, and introduce its time step m dependent value \bar{T}_m :

$$\bar{T}_m := \sum_j g_j \hat{D}_{j,m-\bar{m}_j}, \quad (36)$$

where \bar{T}_m is defined for arbitrary m independent of the current time step n . This is the second formula of FDP=H-matrices, converting \hat{D} to \bar{T} ; hereinafter, the superscript F in this section is abbreviated in equations for notational simplicity. The time history of \bar{T} is stored as a vector in FDP=H-matrices, although \bar{T} can be stored as a scalar in H-matrices. The length of the vector representing the set of \bar{T}_m substantially becomes on the order of the approximated travel time step $(\delta m_i + \bar{m}_j)$, as detailed in §5.2.1. The reference stress gives a simple representation of the stress:

$$T_{i,n} = f_i \bar{T}_{n-\delta m_i}. \quad (37)$$

This is the third formula of FDP=H-matrices, converting \bar{T} to T .

The formulae converting \hat{D} to \bar{T} (Eq. (36)) and \bar{T} to T (Eq. (37)) include time shifts, giving a different arithmetic of FDP=H-matrices from that of H-matrices. In Eq. (36) converting \hat{D} to \bar{T} , \bar{T} at the time step m is contributed from the source (j) motions in the past by \bar{m}_j (called the receiver-averaged travel time step). The delay of the interaction in FDP=H-matrices is caused by the wave propagation, unlike the static case of the original H-matrices, assuming the instantaneous interactions. Similarly, the formula converting \bar{T} to $T_{i,n}$, Eq. (37) refers to the reference stress of past by δm_i (the receiver-dependent travel time step difference) for computing the stress $T_{i,n}$, due to the difference between receivers in the travel times.

These time shifts are expressed by matrices in the arithmetics of FDP=H-matrices. By using the receiver-averaged travel time step \bar{m}_j , we define the time shift matrix for the sources (j),

$$S_{m,j}^{source} := \delta_{m,-\bar{m}_j}, \quad (38)$$

with the Kronecker delta $\delta_{m,-\bar{m}_j} (= 1$ if $m = -\bar{m}_j$ otherwise $= 0)$. The receiver-averaged travel time step \bar{m}_j connects the source j and the reference receiver i_* . Similarly, by using

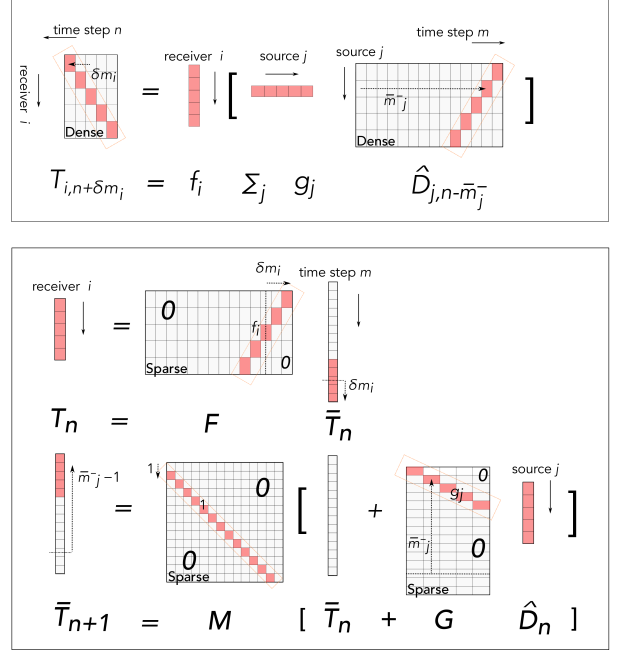


Fig. 10 Diagrams to illustrate the computations in Domain F of FDP=H-matrices converting \hat{D} to T , detailed in §5. Panels contain the computed equations and the diagrams of them. The illustrated matrix is the example in the case of a line fault and a superscript F is abbreviated in the figure. Diagrams are made of squares and bars, respectively representing the matrices and vectors. The arrows express the axes of the coordinates where variables locate or the motions along the axes by δm_i or \bar{m}_j . (Top) A process converting \hat{D} to T without \bar{T} (Eq. (35)). Convolved variables are redly colored, and the nonzero components in M . Eq. (35) includes time shifts in T and \hat{D} . Spatiotemporally dense histories of T and \hat{D} are required to evaluate Eq. (35). (Bottom) Processes converting \hat{D} to T with \bar{T} (Eqs. (41) and (44)). Required variables are sparse matrices (F , G , and M) and vectors (T , \bar{T} and \hat{D}) only. In F , G , and M , red parts respectively store f , g , and 1, and others take 0 values.

the receiver-dependent travel time step difference δm_i , we define the time shift matrix for the receivers (i),

$$S_{m,i}^{receiver} := \delta_{m,\delta m_i}. \quad (39)$$

The receiver-dependent travel time step difference δm_i connects the receiver i and the reference receiver i_* . These matrices are utilized by the arithmetic of FDP=H-matrices in Domain F as explained in the next §5.2.

5.2 Computations for Stress Response of Domain F in FDP=H-matrices

In §5.1, the stress response of Domain F is found to be computable by the successive use of the three formulae. Eqs. (34), (36), and (37) respectively convert D to \hat{D} , \hat{D} to \bar{T} , and \bar{T} to T . We here show a procedure to compute Eqs. (36) and (37) by employing the time shift matrices Eqs. (38) and (39).

5.2.1 Definition of Reference Stress Vector

To compute formulae Eqs. (36) and (37), we first define a vector $\bar{\mathbf{T}}_n := (\dots, \bar{T}_{n+1}, \bar{T}_n, \bar{T}_{n-1}, \dots)^T$, storing T_{n-m} at the m -th component. As seen later, $\bar{\mathbf{T}}_n$ is substantially represented by a vector whose length is $\max_{i,j}(\delta m_i + \bar{m}_j)$, starting with the $-\max_j \bar{m}_j + 1$ component. This is seen in Fig. 10, where the time range of the reference stress used in Eqs. (41) and (44) later defined is enclosed in $n - \max_i \delta m_i \leq n - m < n + \max_j \bar{m}_j$. The vector $\bar{\mathbf{T}}_n$ defined in this way simplifies the arithmetic of FDP=H-matrices in Domain F shown next in §5.2.2.

5.2.2 Sparse-Matrix Representation of Computations in Domain F

The computation of $\bar{T} \rightarrow T$ (Eq. (37)) in FDP=H-matrices becomes efficient with the introduction of a spatiotemporal sparse matrix F , in which the vector \mathbf{f} is embedded as

$$F_{i,m} := f_i S_{m,i}^{\text{receiver}}. \quad (40)$$

Using the matrix F and the reference stress vector $\bar{\mathbf{T}}_n$, the computation of the present stress \mathbf{T}_n is simplified to

$$\mathbf{T}_n = F \bar{\mathbf{T}}_n. \quad (41)$$

The procedure to compute this equation is a vector-to-vector projection by a sparse matrix (Fig. 10, bottom), while the corresponding procedure is a scalar-to-vector decompression in H-matrices. The matrix F is independent of the current time step (n), because we defined the vector \bar{T} so that its 0 th component corresponds to \bar{T} at the current time step n .

Although Eq. (36) is computable with $O(N)$ computation costs, the required time history of the slip rate is amounting to be of $O(NL)$ (detailed in §5.2.3). $O(NL)$ history of the slip rate becomes unnecessary in a way computing \bar{T} incrementally as below. We first introduce a tentative reference stress vector denoted by $\bar{\mathbf{T}}'_n$, substituting 0 to slip rates at the current time step n or later. The m -th component of $\bar{\mathbf{T}}'_n$ denoted by $\bar{T}'_{n,m}$ ($\bar{\mathbf{T}}'_n := (\dots, \bar{T}'_{n+1}, \bar{T}'_n, \bar{T}'_{n-1}, \dots)^T$) is defined as $\bar{T}'_{n,m} := \sum_{j|m+\bar{m}_j^- > 0} g_j \hat{D}_{j,m-(m+\bar{m}_j^-)}$, where $\sum_{j|m+\bar{m}_j^- > 0}$ represents the conditional summation over j that satisfies $m + \bar{m}_j^- > 0$. \bar{T}' eventually converges with \bar{T} ($\bar{T}'_{n,m} \rightarrow \bar{T}_{n-m}$).

Since \bar{T}' is affected only by the receiver motions until the present time step n , we can compute \bar{T}' incrementally. The following matrix \mathcal{M} (called the marching matrix) whose m, m' -component is useful;

$$\mathcal{M}_{m,m'} := \delta_{m,m'+1}. \quad (42)$$

Multiplying $\bar{\mathbf{T}}_n$ by \mathcal{M} represents the evolution of the time step by 1 (time marching, $\bar{\mathbf{T}}_{n+1} = \mathcal{M} \bar{\mathbf{T}}_n$). In contrast to the \bar{T} cases, for $\bar{\mathbf{T}}'_n$, the difference $\bar{\mathbf{T}}'_{n+1} - \mathcal{M} \bar{\mathbf{T}}'_n$ represents an incremental nonzero contribution of $\hat{\mathbf{D}}_n$ to $\bar{\mathbf{T}}_n$ at the current time step n . The difference ($\bar{\mathbf{T}}'_{n+1} - \mathcal{M} \bar{\mathbf{T}}'_n$) is described

by an equation similar to Eq. (41) (Fig. 10, bottom panel). Defining a spatiotemporal sparse matrix G with constituting vector \mathbf{g} as

$$G_{m,j} := g_j S_{m,j}^{\text{source}}, \quad (43)$$

the time evolution of \bar{T}' is expressed by

$$\bar{\mathbf{T}}'_{n+1} = \mathcal{M} [\bar{\mathbf{T}}'_n + G \hat{\mathbf{D}}_n]. \quad (44)$$

The derivation of Eq. (44) is detailed in §E.4. This equation represents adding the contribution of the current slip rate contribution $\bar{\mathbf{T}}'_n$ the origin of which temporally evolves. All the quantities of the right hand side are of the current time step, and the history of \mathbf{D}_{n-m} is unnecessary except for $0 \leq m < \max \Delta m_j$.

The component of $\bar{\mathbf{T}}'_n$ completing the summation over the entire time history exactly coincides with that of the reference stress, written mathematically as

$$\forall m > -\min_j \bar{m}_j^-, \quad \bar{T}'_{n,m} = \bar{T}_{n,m}, \quad (45)$$

where $T_{n,m}$ and $T'_{n,m}$ respectively denote the m -th component of $\bar{\mathbf{T}}_n$ and $\bar{\mathbf{T}}'_n$. Because of this conditional identity, we can substitute $\bar{\mathbf{T}}'_n$ with $\bar{\mathbf{T}}_n$ when evaluating Eq. (41). Eqs. (44) and (45) allow us to discard the past history of slip rates. We later omit the prime from \bar{T}' and do not distinguish between \bar{T}' and the reference stress \bar{T} .

As described above, we constructed a way to compute Eq. (35) comprising Eqs. (41) and (44). Combination of this with \hat{D} computation (Eq. (34)) is the arithmetic of FDP=H-matrices in Domain F (Eq. (33)). It computes the stress step by step by converting $D \rightarrow \hat{D}$ (Eq. (34)), $\hat{D} \rightarrow \bar{T}$ (Eq. (41)), and $\bar{T} \rightarrow T$ (Eq. (44)). The memory and computation costs to evaluate Eqs. (41) and (44) are on the order of the number of elements in a block cluster and $dist$, so that the costs becomes of $O(N \log N)$, as explained related to Fig.9. In the computation of \hat{D} , the time length of the required slip history becomes of $O((\Delta t_j^- + \Delta t_j^+)/\Delta t) = O(1)$, so that the costs to evaluate Eq. (34) is also of $O(N \log N)$. Consequently, all the costs to compute and store the required quantities in the arithmetic in Domain F are of almost $O(N)$.

5.2.3 Computations for $\hat{D} \rightarrow \bar{T}$ at Almost $O(NL)$ Memory Cost

We here briefly refer to another way to evaluate \bar{T} . Evaluation of \mathbf{T}_n by Eq. (41) at time step n requires \bar{T}_{n-m} in the range of $-\max \delta m_i \leq m \leq -\min \delta m_i$. In these required \bar{T} history, the newly required variable is $\bar{T}_{n-\max \delta m_i}$ only, as long as \bar{T}_{n-1-m} of $-\max \delta m_i \leq m \leq -\min \delta m_i$ is stored at the time step $n-1$ (one step before n). Therefore, by computing Eq. (36) for $m = n - \max \delta m_i$ and storing the history $-\max \delta m_i \leq m \leq -\min \delta m_i$, the time complexity to evaluate \bar{T} in each step is reduced to be of almost $O(N)$, without using Eq. (44). On the other hand, the computation of Eq. (36)

requires $O(N \max \bar{m}_j) = O(NL)$ history of the slip rate without thinning. It is larger than almost $O(N)$. $O(NL)$ memory may be not problematic in some cases when considering the output cost of the slip rate, although the consideration on the problem-dependent output cost is out of the scope in this study.

6 Numerical Experiments

We have developed FDP=H-matrices to simulate ST-BIEM at almost $O(N)$ cost. In this section, we implement FDP=H-matrices and confirm their properties numerically.

As the simplest application of FDP=H-matrices, we solve 2D anti-plane problems. In 2D problems, the numerical cost is low and the kernel becomes simple, which makes it possible to compare the current implementation thoroughly with the original BIEM implementation. Although Domain I does not exist in the anti-plane problem, the accuracy and cost of Quantization can be examined in Domain S in 2D problems (shown in §D.1, §B.3). In §D, we supplement the additional handling of truncation errors specific to 2D for replacing the kernel in Domain S to the asymptote, which does not exist in 3D [2], primarily intended application of FDP=H-matrices.

The units and the space-time discretization are set as follows. We normalized the stress by the self-interaction (the radiation damping term), and adopted $\Delta t = \beta = 1$. The value of the CFL parameter was $\beta \Delta t / \Delta x = 1/2$. The figures of dynamic rupture solutions are thinned out for visibility.

This section is organized as follows. In §6.1, we separately examined the accuracy of each approximation included in FDP=H-matrices. In §6.2, we examined the accuracy and cost of FDP=H-matrices combining whole approximations, by simulating crack problems. In §6.3, the approximate parameter dependence used in Domain F is examined.

6.1 Numerical Evaluation of Error and Cost Reduction in Domain F

We here evaluate the cost and accuracy of approximations detailed in §4. The results of H-matrices applied to each domain are in §6.1.1, and the results of ART are in §6.1.2.

6.1.1 H-matrices along Wavefronts in Domain F

We showed the way to apply H-matrices along the ray path of Domain F in §4.1. Below, we test its accuracy and cost. Basically, the results of the constant η scheme are shown below. The results of the constant $\eta^2 dist$ scheme, which are more advanced, are mentioned briefly in the last. Used parameters are listed in the caption of Fig. 11. A planar fault is chosen as an example of the application.

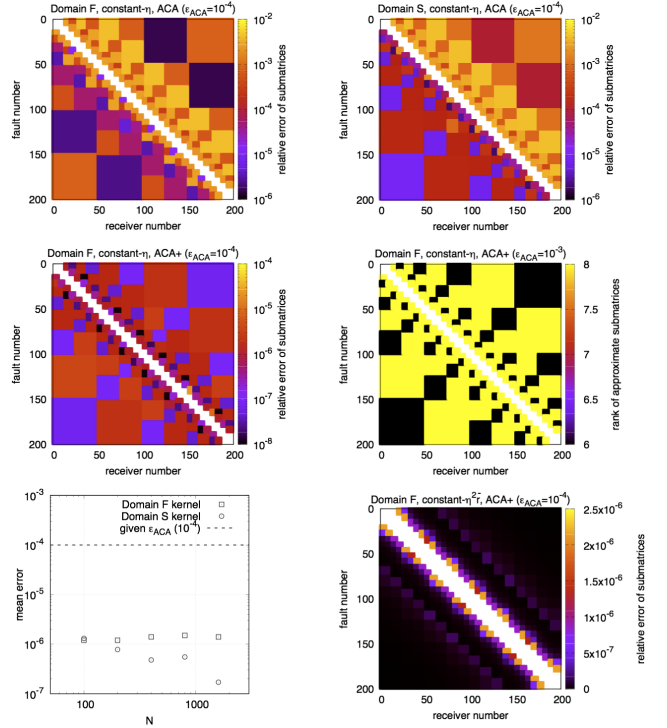


Fig. 11 Error and rank distributions of submatrices with ACA or ACA+, explained in §6.1.1, of $\eta_0 = 2$, $l_{min} = 14$ ($7\Delta x$). Domain F is broadened by $3\Delta x/\beta$ (detailed in §D). The required error value ϵ_{ACA} is written in the panel. The axes express the assigned element numbers. Color bars represent the relative errors or ranks of approximated submatrices. (Top left) Error distribution in \hat{K}^F with ACA for constant η . (Top right) Error distribution in \hat{K}^S with ACA for constant η . (Center left) Error distribution in \hat{K}^F with ACA+ for constant η . (Center right) Rank distribution in \hat{K}^F with ACA+ for constant η . (Bottom left) Mean error of ACA+ (over submatrices, defined in §6.1.2) versus the number of element N . (Bottom right) Errors in \hat{K}^F with ACA+ for constant $\eta^2 dist$.

We first briefly summarize the way of LRA in H-matrices. As mentioned in §2.3, LRA is performed so as to regulate the relative error quantified in the Frobenius norm below the given value ϵ_H in H-matrices. Since exact LRA requires large numerical costs of $O(N^3)$, a fast approximation technique of almost $O(N)$ costs is often used [19]. A typical approximation is the partially pivoting ACA (hereafter simply called ACA) [20]. The parameter of ACA, ϵ_{ACA} , works as ϵ_H as long as ACA works sufficiently [19]. Although ACA does not satisfy the imposed error conditions in some cases, ACA+ is proposed to fix such a problem in the partial pivoting ACA [32]. ACA+ improves the accuracy by using a randomly selected point as an additional candidate of the partial pivoting point.

In the partial pivot of partial pivoting ACA and ACA+, the error condition is weakened to $|K_{a,LRA,l} - K_{a,LRA,l+1}| / |K_{a,LRA,l+1}| < \epsilon_{ACA}$ by commuting $K_{a,LRA,l+1}$ of higher rank by one to the original kernel K , where $K_{a,LRA,l}$ is the approximated low rank kernel of the rank l in the block clus-

ter a . Although this weakened condition is originally for $K_{a,LRA,l}$, we adopted $K_{a,LRA,l+1}$ as the approximated kernel in this paper when the above condition is satisfied; the substantial error for $K_{a,LRA,l+1}$ ($|K_{a,LRA,l+1} - K_a| / |K_a|$) ordinarily has the decreasing tendency compared with that for $K_{LRA,l}$ ($|K_{LRA,l} - K_a| / |K_a|$).

ACA+ is used throughout this paper. To compare ACA+ with (partially pivoting) ACA standardly used in H-matrices, we also show some examples of ACA here in §6.1.1.

The accuracy was evaluated as to whether each approximated submatrix generated by LRA satisfy the required accuracy using $\epsilon_H = \epsilon_{ACA}$. For the accuracy evaluation, if LRA is not converged as sometimes occurring in ACA cases, LRA is terminated when the rank exceeds the original rank of each submatrix. To clarify the degree of the convergence, no modifications are made for the approximated matrices obtained by ACA here in §6.1.1.

The cost was evaluated by the rank of each submatrix. If the approximation works well, the rank of an approximate matrix is expected to be of $O(1)$ and independent of the number of submatrix components. These are essential for the cost of H-matrices to be of $N \log N$.

Constant η scheme The result of the constant η scheme is shown below.

When (partial pivoting) ACA is applied, LRA did not satisfy the required accuracy in some cases (Fig. 11, top left panel). Even when ϵ_{ACA} was set at 10^{-4} , the approximate matrix contained errors (corresponding to ϵ_H) on the order of 10^{-3} to 10^{-2} . The observed accuracy problem is consistent with many previous studies of H-matrices in spatial BIEM cases [19,32]. Indeed, this accuracy degradation was also observed in the asymptotic kernel in Domain S (static kernel) (Fig. 11, top right panel). This accuracy degradation is thus the problem of LRA when using partial pivoting ACA. The accuracy was asymmetric to the increase / decrease of the difference between the source number and receiver number. This suggested that ACA erroneously terminated the approximation if the gradient of the kernel value along the source / receiver element number was large at the initial pivoting point, as previously pointed out [32]; the initial pivoting point is set at the 1, 1 element of the submatrix in this paper.

When ACA+ was used, the accuracy greatly improved in Domain F (Fig. 11, center left panel), as in the case of the static kernel [19], corresponding to the kernel in Domain S. ACA+ worked for all the kernel used in this paper (shown in §6.3.1, Table 5).

In the cost evaluation, the ranks of the approximated submatrices were independent from the number of submatrix elements (Fig. 11, center right panel). The ranks were almost constant and of $O(1)$. This suggested that the cost in the

spatial direction of FDP=H-matrices becomes of $O(N \log N)$ with ACA+.

Additionally, in all the panels of Fig. 11 of the constant η scheme, the accuracy and rank showed fractal patterns from the center to the top right / bottom left end. This is made by the (hierarchically repeating) accuracy variations depending on the value of $diam/dist$ at each level of submatrices, since LRA of the kernel is substantially an expansion about the similarity ratio of $diam/dist$ varying within $\eta/2 < diam/dist < \eta$. Note that these vibrations did not become big problems. This is because the accuracy was always much lower than ϵ_{ACA} , and the rank was of $O(1)$ in the case of ACA+.

The size dependence of the error is shown in Fig. 11 (bottom left). The accuracy of ACA was measured by the average of the relative error norm (called the mean error) representing the mean error of LRA. The errors was summed over submatrices of admissible leaves and weighted with the number of the included matrix component in the averaging process. The parameter values were unchanged from the above experiments except for N . The mean errors of the kernels were smaller than the specified ϵ_{ACA} value ($\epsilon_{ACA} = 10^{-4}$) in the studied N range. The error of the asymptotic Domain S kernel (corresponding to the spatial BIEM kernel) showed the decreasing tendency as N increases. The error of the Domain F kernel were roughly independent of N . By considering that the studied fault size ($N \geq 100\Delta x$) is much larger than $l_{min}(= 7\Delta x)$ and Δx in Fig. 11 (bottom left), these observed tendencies are expected to be maintained in the larger N . The accuracy of approximated matrices will be much smaller than the specified error values ϵ_{ACA} in larger N cases.

It is not obvious why the difference in the size dependence arises between Domains F and S kernels, but the reason should be ascribable to the difference of them. A possibly unique difference of both the kernels is in the attenuating properties that Domain F one is less attenuated at a distant point. The reason of different size dependence of the two kernels will be such difference in attenuating properties.

As above, as far as we studied, ACA+ was capable of suppressing such an error below ϵ_{ACA} even when ACA did not satisfy the required error condition. In addition, in ACA+, the rank was independent from the number of submatrix elements. By considering these, we use ACA+ hereafter.

Constant $\eta^2 dist$ scheme We briefly mention the result of the constant $\eta^2 dist$ scheme. ACA+ worked successfully in the case of the constant $\eta^2 dist$ scheme, as in the case of the constant η scheme (Fig. 11, bottom right panel). In addition, the accuracy was improved as $dist$ increased when the constant $\eta^2 dist$ scheme was adopted. This is because the $diam/dist$ ($= O(\eta)$) ratio (that is the small parameter of analytically expanding the kernel) becomes smaller as $dist$ increases in

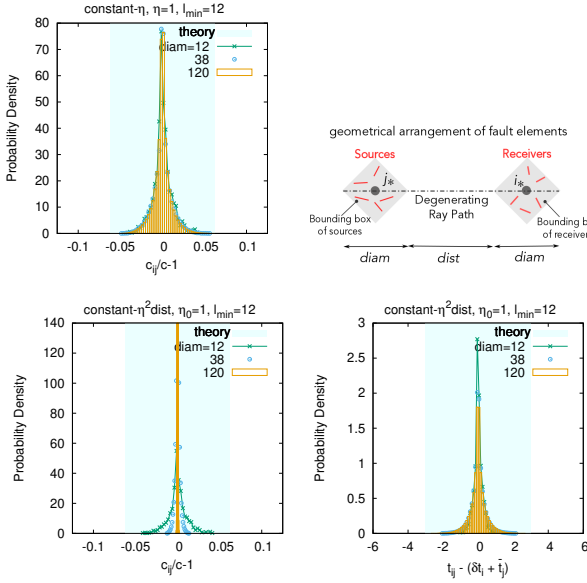


Fig. 12 Error distributions of the effective wave speeds and travel times in ART. The source and receiver clusters are arranged so that the accuracy becomes the worst in the same admissibility condition. Faults are uniformly distributed in the bounding boxes (with number density = 1/4). In all figures, the theoretical error upper bounds (Eqs. (26) and (28)) are plotted (indicated in the colored region called theory in the figure). (Top right) Simulated geometry. The degenerating ray path overlaps diagonal lines of bounding boxes and $diam = \eta dist$. (Top left) Error distributions of the effective wave speeds in the constant η scheme, independent of $diam$. (Bottom left) Error distributions of the effective wave speeds in the constant $\eta^2 dist$ scheme, becoming impulsive as $diam$ increases. (Bottom right) Error distributions of the effective travel time in the constant $\eta^2 dist$ scheme, independent of $diam$.

the constant $\eta^2 dist$ scheme cases. The small perturbation parameter means the rapid convergence. LRA is thus safely applied to the constant $\eta^2 dist$ scheme cases than to the constant η scheme cases.

6.1.2 ART

We formulated the approximations of ART in §4.2.2. To clarify the detail of the approximation errors, we here investigate the error distribution in the case of a specific example.

We here focus on evaluating errors caused by the travel time separation, Eq. (21). The separation of the travel time, Eq. (21), is regarded as different approximations in the constant η and constant $\eta^2 dist$ scheme. The constant η scheme regards Eq. (21) as the approximation of wave speeds, Eq. (25), bounded by Eq. (26). The constant $\eta^2 dist$ scheme regards Eq. (21) as the approximation of travel times, bounded by Eq. (28). The approximation of the normalized waveform (Eq. (24)) is later evaluated in the crack problem treated in §6.2, because its accuracy depends on the temporal change rate in the slip rate.

As the arrangement of the source / receiver clusters to be examined, we chose the most demanding situation for the accuracy in the same admissibility condition (Fig. 12, top right panel); in this situation, $diam/dist = \eta$ and the degenerating ray path overlaps the diagonal lines of bounding boxes. The fault elements were supposed to be distributed uniformly within the 2D bounding box (with the number density = 1/4). Since the parameter values do not influence the approximation qualitatively, we here investigated the case of a parameter value set: ($\eta_0 = 1$, $l_{min} = 12$). As can be seen from Eq. (21), the error of the travel time separation is determined by the ratio of $diam$ to $dist$. We changed this ratio to evaluate the $diam/dist$ dependence of the accuracy.

Note that we here did not consider the case of cracks aligned along a straight line, despite of its geometrical simplicity. This is because such a case cannot test the approximation accuracy, due to the exact travel time separation into the receiver-averaged travel time and the receiver-dependent travel time difference (Eq. (21)). This exact separation corresponds to that δr in Fig. 7 becomes zero in a line fault.

In the case of the constant η scheme, the error distributions of the effective wave speeds (Eq. (25)) obeyed almost the same distribution independent of $dist$ (Fig. 12, top left panel). In this figure, the value of $diam$ was initially set at $\eta_0 l_{min}$ and changed by the factors of $\sqrt{10}$ and 10. This figure suggests that the travel time separation suppresses the effective wave speed errors to small values independent of $dist$ in the constant η scheme, as described in §4.2.2. The numerical dispersion is thus expected to be negligible in the constant η scheme. Most of the errors were suppressed to less than the theoretical approximate upper bound $\eta^2/4$ given by Eq. (26) shown in blue green frame in the figure. It was also noticed that most of the errors were much smaller than the upper bound value. This means that the majority of the effective wave speeds in ART is much more accurate than the estimates given by the upper bound.

In the case of the constant $\eta^2 dist$ scheme, the error of effective wave speeds disappeared at distant points (Fig. 12, bottom left panel). The distribution of effective wave speeds became delta functional as $dist$ increases, and the errors almost disappeared. In addition, the errors of travel times were suppressed to less than the approximate upper bound value $\eta_0 l_{min}/(4c)$ given by Eq. (28). The errors of the travel times were suppressed to a finite value even at distant points (Fig. 12, bottom right panel).

As above, the error upper bounds of ART were well evaluated analytically by Eqs. (26) and (28). It was also found that most of the errors in the distributions of them were much smaller than their analytical upper bounds. These suggest that FDP=H-matrices can be highly accurate even in nonplanar faults, a demanding example of which is the distributed cracks analyzed here.

6.2 Crack Problems

Here we investigate the cost and accuracy of FDP=H-matrices in actual crack problems. In this section, first, the cost is evaluated in §6.2.1. Subsequently, the solution accuracy is outlined in §6.2.2.

The simulation was performed under the following settings. We investigated the crack problem in an infinite homogeneous isotropic linear elastic medium. The slip rate was assumed to be 0 until the shear traction on the fault reached the yielding value T_{th} . After the shear traction reaches to the yielding value, the stress was assumed to follow the slip weakening friction law [33]. As the specific function of the slip weakening friction law, we adopted an exponential function in the transient yielding zone; it gives the shear traction T_{shear} as $T_{shear} = (T_{th} - T_{dy}) \exp(-\Delta u / D_c) + T_{dy}$, where T_{dy} denotes the shear traction in the fully yielding zone, and D_c denotes a characteristic slip-weakening distance. The initial stress condition is detailed in §6.2.2 where physical setting becomes important. Used parameters are listed in the captions, for reproducibility of obtained results; parameters concerning 2D specific approximations are defined in §D. Note that the figures of dynamic rupture solutions are thinned out for visibility.

Hereafter, the implementation of ACA+ was modified (except for the ACA test done in §6.3.1). We replaced the approximate matrix with the original matrix when the rank of the approximated submatrix exceeds the original rank. Such exception handling is occasionally required in the neighboring clusters, particularly in the cases of nonplanar faults.

6.2.1 Cost Scaling

As described in §4.2.2, the cost of FDP=H-matrices is ideally of almost $O(N)$ ($O(N \log N)$) in the constant η scheme. Here we investigated whether this cost scaling is actually realized in a crack problem.

During this verification, we quantified the memory consumption and the time complexity of the convolution in the following ways. The memory consumption is evaluated by the total memory consumption. To demonstrate the geometry independent aspects, the memory cost of the original implementation is evaluated without using the translational symmetry of faults in planar problems. In order to evaluate the time-complexity, we measured the computation time to complete a whole simulation in single thread divided by the number of time steps (referred to as the computation time per time step). We evaluated the time on a laptop (MacBook Pro MF839). We here deal with a planar fault simply, because the cost scaling does not depend on the fault geometry qualitatively. The adopted values of approximation parameters are described in the caption.

The cost of FDP=H-matrices was compared to that of the original ST-BIEM in Fig. 13. Both the total memory consumption and computation time per time step are of $O(N^2 M)$ in the original ST-BIEM. As expected, both of them showed the almost $O(N)$ scaling in the case of FDP=H-matrices. The cost reduction was huge.

More precisely, the cost of FDP=H-matrices well fitted to the $N \log(N/N_*)$ scaling with a constant N_* . In this case, $N_* \sim 10$ (detailed in §6.3.2). FDP=H-matrices have $O(N)$ costs of inadmissible leaves and $O(N \log N)$ costs of admissible leaves. The total costs thus become of $N \log N / N_*$, which converges to $N \log N$ when N is sufficiently larger than N_* .

6.2.2 Spatiotemporal Pattern of Solution Accuracy

Here we investigated the spatiotemporal characteristics of the solution of FDP=H-matrices, by solving 2D anti-plane problems. We simulated the examples of a planar fault and a nonplanar fault. The following analyses consistently use the constant η scheme. The value of η used here is near 1, which is on the order of η values frequently used in H-matrices. For example, $\eta = 2$ is used in a previous study [34] of a three-dimensional static elastic problem.

Accuracy in Planar Problems First, we investigated solution errors of FDP=H-matrices by solving the planar fault problem being the simplest fault arrangement. Since the solution characteristics of FDP=H-matrices do not depend on the problem settings largely, we investigated the following initial stress condition as an example. Initially, the homogeneous background shear traction T_{bg} exists. The rupture is next initiated by a quasistatic elliptic single force of a radius L_{init} such that the maximum amplitude of the single force is at the value exactly nucleating the spontaneous rupture.

Fig. 14 (top left) shows the spatiotemporal evolution of slip rates in the original ST-BIEM. Adopted parameter values are enumerated in the figure and caption. The rupture propagated to the left and right on the fault from the initial crack position. Fig. 14 (top right) shows the solution obtained with FDP=H-matrices. It was shown that the solution of FDP=H-matrices well reproduced the original solution.

To visualize the error quantitatively, we compared the snapshots of specified times (Fig. 14, bottom left panel). The error of the approximate solution ($D_{i,n}^{approx}$) over the element positions i at each time step n was measured by the relative error of the Euclidean norm $[\sum_i (D_{i,n}^{approx} - D_{i,n}^{orig})^2 / \sum_i (D_{i,n}^{orig})^2]^{1/2}$, where $D_{i,n}^{orig}$ denotes the original solution. Error values are shown in brackets at the end of the legend of FDP=H-matrices.

The errors were suppressed below 0.4% even after approximately 1000 steps when $\eta = 1/2$ (Fig. 14, bottom right panel). These values are very small, although the errors of

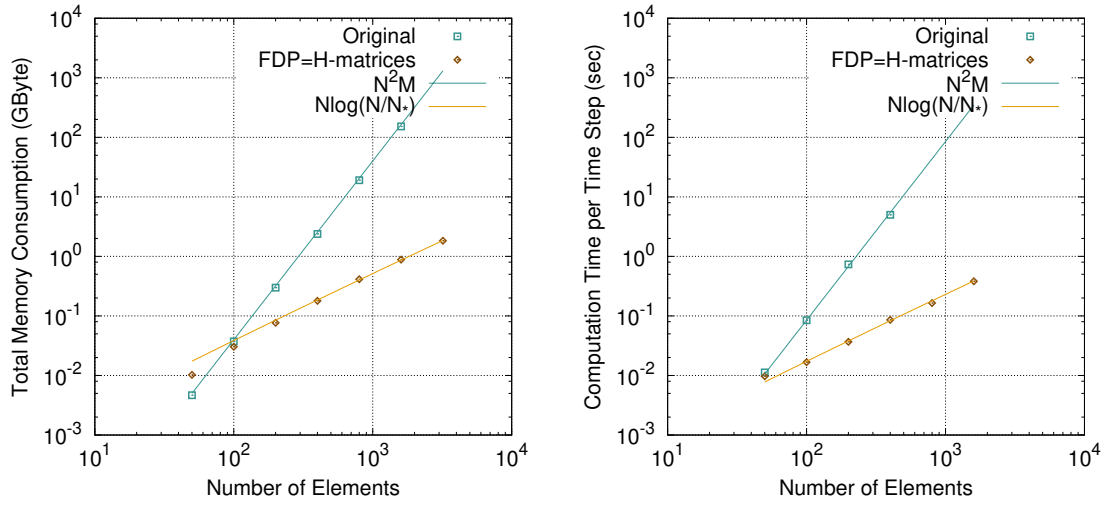


Fig. 13 Measured costs of FDP=H-matrices of almost $O(N)$, compared with the original ST-BIEM ones of $O(N^2M)$. The plotted results are of a planar problem detailed in §6.2.2. The parameter values are set at $M = 5N$, $\epsilon_Q = \epsilon_{st} = \epsilon_{ACA} = 10^{-2}$, $l_{min}/\Delta x = 5$, and $\eta = 2$, and Domain F is broadened by $3\Delta x/\beta$. (Left) The total memory consumption. (Right) The computation time per time step (the ratio between the total computation time to complete the total time evolution and the number of the total time steps).

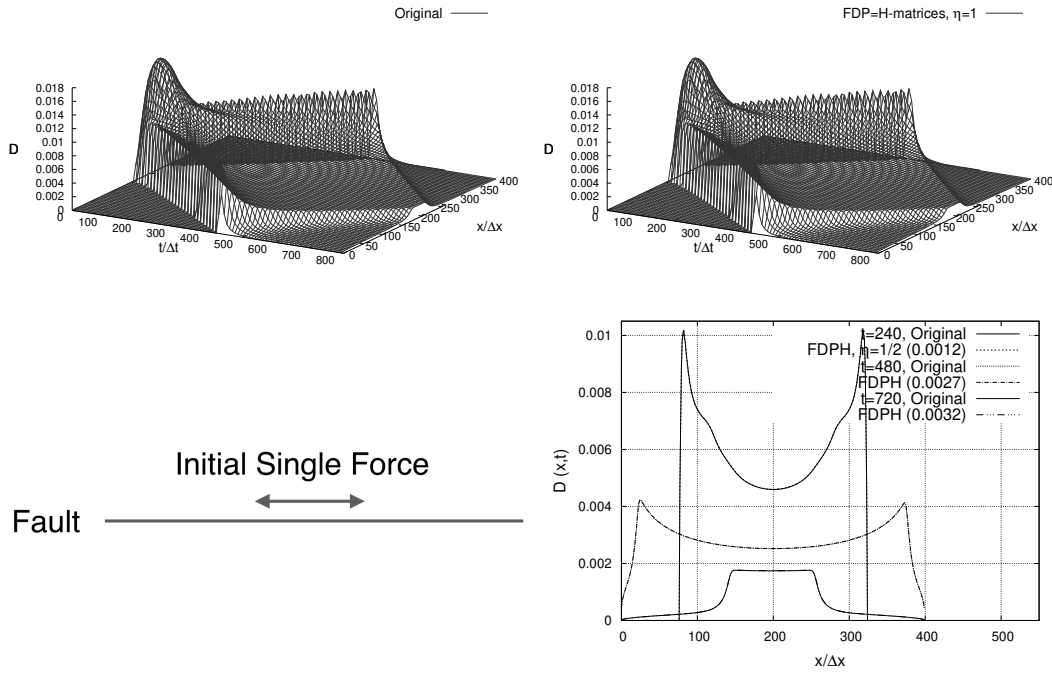


Fig. 14 Simulated dynamic rupture on a planar fault. Parameters of the given problem are set at $(T_{th}, T_{bg}/T_{th}, T_{dy}/T_{th}, D_c/(\Delta x/2), L_{init}/\Delta x) = (10^{-2}, 0.35, 0, 0.1, 50)$. The parameters of FDP=H-matrices are set at $(l_{min}/\Delta x, \epsilon_{ACA}, \epsilon_Q, \epsilon_{st}) = (5, 10^{-3}, 10^{-3}, 10^{-6})$, and Domain F is broadened by $10\Delta x/\beta$. (Top left) The original solution of the slip rate D evolving over space x and time t . (Top right) D simulated by FDP=H-matrices evolving over space x and time t . (Bottom left) Simulated planar geometry, detailed in §6.2.2. The length L of the fault is set as $L = N\Delta x$. (Bottom right) Snapshots of top panels at given time t , where FDP=H-matrices are abbreviated as FDPH. The value at the end of the legend of FDP=H-matrices represents the error from the original solution in the snapshot, evaluated by the ratio of the Euclidean norm of the error to the Euclidean norm of the original solution.

FDP=H-matrices were temporally accumulated in each snapshot as in FDPM [1] applied to 2D problems. 0.4% is about 0.1 times smaller than the absolute value of the short-wavelength specific errors are detailed in §D. numerical oscillation frequently observed due to given numerical conditions and rounding errors of kernel evaluation [28, 14]; for example see Fig. 3 shown by Tada and Madariaga in [28]). In addition, there were no observable errors in the rupture propagation speed that is frequently studied in the dynamic rupture problems as a significant quantity [31]. These observations suggest that the error caused by FDP=H-matrices will be within the allowable range in many cases.

Accuracy in Nonplanar Problems Subsequently, we examined the accuracy of FDP=H-matrices in the case of a nonplanar fault configuration. We dealt with a fault shown in Fig. 15 (bottom left), a line fault kinked at $5/8$ length by $\pi/4$. Initially, the shear traction is assumed to be a homogeneous value T_{bg} . An elliptical slip of a radius L_{init} is next introduced such that the maximum slip is equal to E_{init} .

Fig. 15 (top left) and Fig. 15 (top right) respectively show the spatiotemporal evolution of slip rates simulated by the original ST-BIEM and FDP=H-matrices. In the original result, the rupture first propagated on a plane up to the time step $t/\Delta t \sim 100$. The rupture subsequently extended to the whole fault region beyond the kink (located between the elements of $i = 249$ and 250). The result of FDP=H-matrices reproduced the original solution well.

The snapshot showed that the FDP=H-matrices accurately reproduced the original solution even in this nonplanar fault geometry (Fig. 15, bottom right panel). The error was shown to be temporally cumulative as in the case of the planar problem. The magnitude of the error was roughly the same as in the planar problem. This suggests that FDP=H-matrices are applicable to nonplanar geometries keeping their high resolution. The relationship between the numerical accuracy and cost is detailed in next §6.3.

6.3 Parameter Dependence of Cost and Accuracy

In §6.1 and §6.2, it was shown that FDP=H-matrices are almost $O(N)$ methods applicable to nonplanar problems. However, since FDP=H-matrices contain multiple parameters, the parameter dependencies of the solution accuracy and cost are not simple. For this reason, focusing on the constant η scheme, which can achieve almost $O(N)$ costs, we investigate the parameter dependencies of the cost and accuracy in FDP=H-matrices.

We here particularly investigate the influence of the characteristic approximations used in FDP=H-matrices described in §4. First, we study the influence of ϵ_{ACA} (the approximate value of the allowable error in the low rank approximation of H-matrices). Second, we study the influence of η (upper

bound of $diam/dist$) determining the approximation accuracy of ART. Parameters dependencies in handling of 2D

6.3.1 ϵ_{ACA} Dependence

As mentioned in §2.3, H-matrices approximate the submatrix K_a of the admissible leaf a to a low rank kernel $K_{a,LRA}$. The error criteria is given by $(|K_a - K_{a,LRA}| < \epsilon_H |K_a|)$ for a given constant ϵ_H . ACA (of the partially pivoting) and ACA+ rapidly compute $K_{a,LRA}$ by weakening the error criterion [19]. If ACA (or ACA+) works, $(|K_a - K_{a,LRA}| \lesssim \epsilon_{ACA} |K_a|)$ is expected for a given constant ϵ_{ACA} . We here examined the ϵ_{ACA} dependencies of the accuracy and cost in FDP=H-matrices, by using a planar problem.

In our implementation using ACA+, ϵ_{ACA} was not a relevant parameter for the solution accuracy. Indeed, the solution error (quantified in the same way as that in §6.2.2) was unchanged when we changed ϵ_{ACA} (Table 5, errors in solutions, abbreviated to soln). This suggests that the accuracy with ACA+ is much better than that expected from the value of ϵ_{ACA} , as shown in Fig. 11.

In order to study the influence of ACA in detail, we investigated the accuracy and the cost of LRA, which are directly affected by ϵ_{ACA} . This is a frequently adopted way in the previous studies of H-matrices [19]. The accuracy of ACA was measured by the average of the relative error norm (the mean error, introduced in §6.1.1). The cost of ACA was measured by the average of the rank (called mean rank) linearly proportional to the cost of FDP=H-matrices. The errors and ranks of a submatrix were summed over submatrices of admissible leaves and weighted with the number of the included matrix component in the averaging process. Since the variances of the accuracy and rank were secondary as shown in Fig. 11, we here excluded them from the examination.

We investigated the average of the relative error norm of ACA $(|K_a - K_{a,LRA}|/|K_a|)$, and the average rank.

Table 5 shows the ϵ_{ACA} dependence of the mean error and average rank. Indices, F, S, and tr respectively correspond to the Domain F kernel, and (asymptotic) Domain S kernel, transient kernel in Domain S (introduced in §D.1). The parameters are set at the same values as those in Fig. 11.

The mean error was 10^{-2} times smaller than ϵ_{ACA} in the range of $\epsilon_{ACA} = 10^{-2} \sim 10^{-5}$ (mean error in Table 5). It was consistent with that the accuracy of the solution seemed much better than ϵ_{ACA} in Fig. 11. In addition, the mean error was roughly in proportion to ϵ_{ACA} .

The mean rank increased in proportion to $\log \epsilon_{ACA}$ (mean rank in Table 5). This ϵ_{ACA} dependence of the rank is consistent with the theoretical estimates of ACA costs [20]. Since the rank does not change so much even when ϵ_{ACA} is increased, ϵ_{ACA} has little impact on the numerical costs after the kernel matrices are approximated.

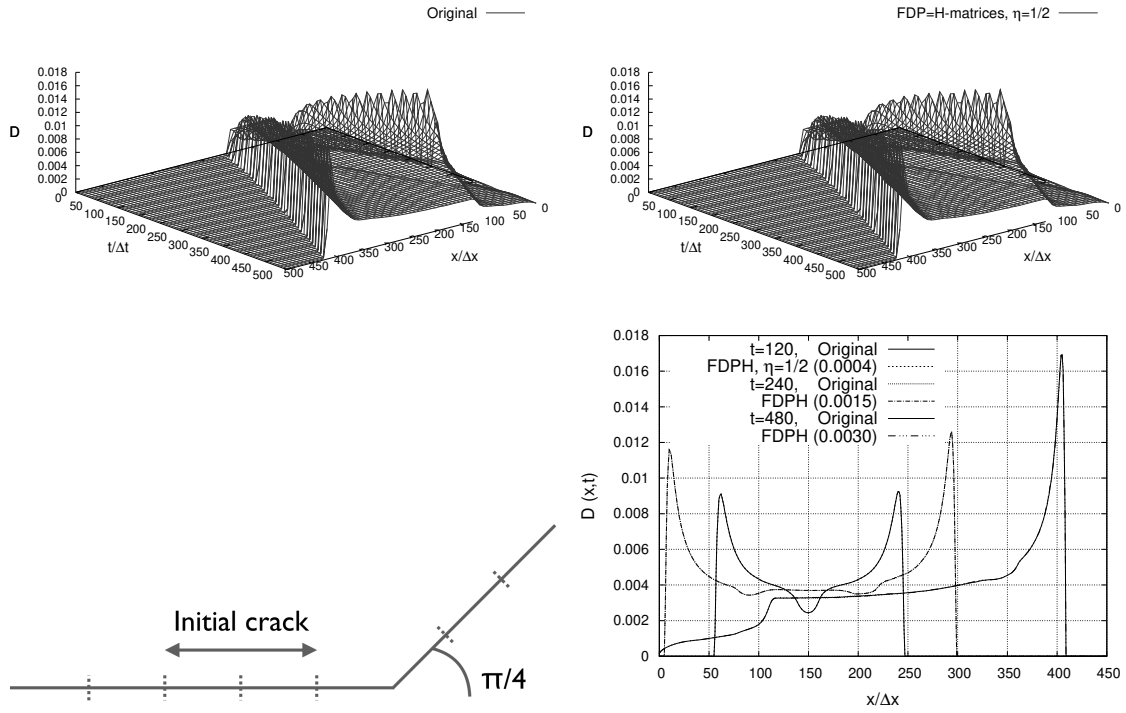


Fig. 15 Simulated dynamic rupture on a nonplanar fault. The parameters are $(T_{th}, T_{bg}/T_{th}, T_{dy}/T_{th}, D_c/(\Delta x/2)) = (10^{-2}, 0.35, 0, 0.1)$, $(L_{init}/\Delta x, E_{init}/(\Delta x/2)) = (50, 0.02)$, $(l_{min}/\Delta x, \epsilon_{ACA}, \epsilon_Q, \epsilon_{st}) = (5, 10^{-3}, 10^{-3}, 10^{-6})$, and Domain F is broadened by $10\Delta x/\beta$. (Top left) Original solution of the slip rate D evolving over space x and time t (Top right) D simulated by FDP=H-matrices evolving over space x and time t . (Bottom left) Simulated geometry, detailed in §6.2.2. The kink is located between $x/\Delta x = 249$ and 250. (Bottom right) Snapshots of top panels at given times t , where FDP = H-matrices are abbreviated as FDPH. The value at the end of the legend of FDP=H-matrices represents the error from the original solution defined in the same way as that of the planar fault problem.

ϵ_{ACA}	mean error			mean rank			error
	F	S	tr	F	S	tr	soln
10^{-2}	3×10^{-5}	6×10^{-5}	2×10^{-5}	6.0	6.0	6.0	0.003
10^{-3}	2×10^{-6}	2×10^{-6}	2×10^{-6}	7.3	7.3	7.3	0.003
10^{-4}	1×10^{-6}	7×10^{-7}	5×10^{-7}	8.0	8.0	8.0	0.003
10^{-5}	6×10^{-8}	3×10^{-7}	3×10^{-8}	9.3	9.3	9.3	0.003

Table 5 Mean error and mean rank (and the solution error) versus ϵ_{ACA} . The mean error is the relative error measured by the Frobenius norm averaged over the matrix, and the mean rank is the rank per admissible leaf averaged over the matrix; additionally, we listed the error in the solution, abbreviated as soln in the table, (evaluated at $t = 480$ under the same definition as in Fig. 15 and using the same parameters of Fig. 15 except for ϵ_{ACA}). F, S, tr respectively correspond to the Domain F kernel, Domain S asymptotic kernel, and transient kernel in Domain S (defined in §D.1).

6.3.2 η Dependence

Theoretically, η affects the cost and the approximation accuracy of ART (§4.2) by changing the admissibility condition of H-matrices [19]. We here examined them numerically.

Fig. 16 showed that the solution with FDP=H-matrices converged to the original solution as η became smaller. Especially in the planar case, when η was small, the error ap-

proximately depended linearly on η . This η dependence is ascribable to the error of $O(1/(1/\eta + 1))$ concerning the degenerating normalized waveform (Eq. (24)), since the error depending η arises only from the normalized waveform approximation (Eq. (24)) of ART in a planar fault case. This is due to the exact travel time separation by ART in a 2D planar fault case (as mentioned in §6.1.2). Unlike the planar fault, the error did not change when the value of η is 1 or larger in the nonplanar fault. This is probably because ART also has an approximation error of the effective wave speed in nonplanar fault geometries. On the other hand, the error at $\eta = 1/2$ in the nonplanar problem was roughly the same as that in the planar problem, and the convergence of the solution was confirmed as η decreased as in the planar problem. It suggested that errors of the normalized waveform were more effective than the travel time errors, in the situation that η became sufficiently small.

The η dependence of the cost was fitted roughly to $N \log N/N_*$, by using N_* depending on η (Fig. 16, bottom right panel). Since the total memory consumption and computation time per time step showed the same size dependence in §6.2.1, we here showed only the computation time per time step. Measurements were made on a planar fault with the same setting as the case in §6.2.1 except for η values. Fig. 16

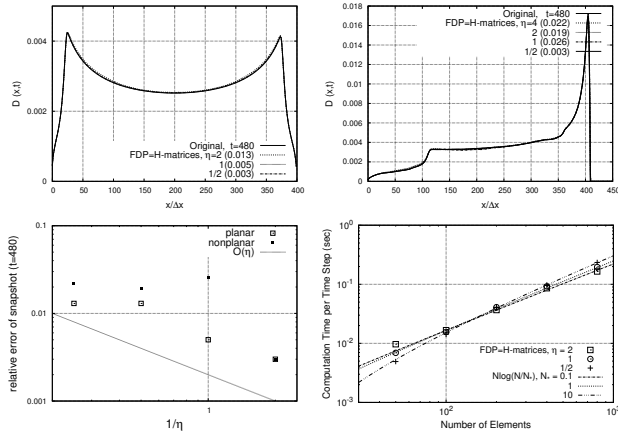


Fig. 16 Error and cost versus η . (Top left) Snapshots of the slip rate $D(x, t)$ at $t = 480$ on a planar fault. Parameter values except for that of η one are the same as in Fig. 14. The bracketed value at the end of the legend of FDP=H-matrices represents the relative error from the original solution defined in the same way as that of §6.2. (Top right) Snapshots of the slip rate $D(x, t)$ at $t = 480$ on a nonplanar fault. Parameter values except for η one are the same as in Fig. 15. The bracketed value at the end of the legend of FDP=H-matrices represents the relative error from the original solution defined in the same way as that of §6.2. (Bottom left) Relative error plotted as a function of η . The settings are the same as in top panels. As η decreases, the solution of FDP=H-matrices converges to the original solution. The relative error is proportional to η when η is small in a planar problem and suggests that the error originates from the normalized waveform approximation of ART (Eq. (24)). Although there is no simple error dependency in a nonplanar problem, the error is also reduced if η is decreased sufficiently as in the case of the planar fault. (Bottom right) The computation time per time step measured in §6.2 plotted as a function of η . Measurements were made on a planar fault with the same setting as the case in §6.2.1 except for η values. $N \log N$ scaling is maintained even if η is changed.

(bottom right) shows that the cost of FDP=H-matrices was of $O(N \log N)$ even if η was changed. The reason why the change in η affects N_* and does not affect $N \log N$ scalings of the costs is that η affects only the balance of the admissible leaves cost of $O(N \log N)$ and inadmissible leaves cost of $O(N)$. In our measurement, N_* showed a tendency proportional to $1/\eta$.

7 Discussion

We have developed FDP=H-matrices to compute ST-BIEM at almost $O(N)$ memory and computation costs. In this section, first, we summarize some practical notes concerning the characteristic approximations of FDP=H-matrices in §7.1. This is also a summary of the numerical / analytical error estimates. We next study the parameter dependence of errors specific to 2D problems (§D) in detail. (The summary of 2D specific approximations is contained in §7.1.) We mention the future works in §7.2.

7.1 Summary Information on Parameter Dependence of FDP=H-matrices

The accuracy of FDP=H-matrices was analytically evaluated in §4 and numerically verified in §6 and §A.3. These clarified the influences of the parameters (ϵ_{ACA} , ϵ_Q , η , l_{min}) on the error and cost. Parameter dependencies of FDP=H-matrices are summarized below. 2D specific treatments detailed in §D are also summarized here.

In ACA, the method selection for LRA became the decisive factor of the accuracy (§6.3.1) over ϵ_{ACA} values. As far as we examined, ACA+ seemed to work better than partially pivoting ACA, which sometimes erroneously worked. As far as we examined, the substantial accuracy (ϵ_H) was much better than we specified (ϵ_{ACA}) (Fig. 11, Table 5) in ACA+ cases. Considering the mean error achieved by ACA+ in our test (Table 5), $\epsilon_{ACA} = 10^{-4}$ seems to ensure the same accuracy as that of the crack problems in this paper.

The errors of the travel time and normalized waveform are controlled by η and l_{min} in the approximations of ART. The constant η scheme suppresses the error of the wave speed below a value of $O(1/(1 + 1/\eta)^2)$ (Eq. (26)) regardless the source receiver distance. It does not depend on l_{min} , and the wave speed error is less than approximately 6% when $\eta = 1$ in Eq. (26). The error of the normalized waveform is on the order of the width of the time definition range of Domain F (Eq. (24)), which is several times the original discretized time interval. As far as we examined, the solution of $\eta = 1/2$ converged to the original solution in a range of about 0.3% relative error (§6.2.2), which is roughly 10 times smaller than the error frequently occurring due to the spatiotemporal discretization [28, 14]. In the constant $\eta^2 dist$ scheme case, η and l_{min} determine the accuracy in a complex manner (Eq. (28)); its error can be smaller than the discretization error of the boundary element.

In Quantization, ϵ_Q (and ϵ_{st} defined later) dumped the solution (§A.3, §D.3). In our evaluation, the solution error was unchanged from 0.3% relative error in the range $\epsilon_Q = 10^{-3} \sim 10^{-1}$ (§A.3) as long as the absolute allowable error (ϵ_{st}) is of 10^{-6} (Fig. D.2); ϵ_{st} requires much small values to deal with 2D specific errors (detailed in §D) and secondarily ϵ_Q becomes irrelevant to the accuracy. Concerning the cost, the absolute allowable error value ϵ_{st} (§D.3) is less dominant than the relative allowable error value ϵ_Q (§A.3). These suggest that the additional absolute error condition reduces the cost of Quantization with keeping the accuracy.

There is an additional 2D specific problem in FDP=H-matrices that the space-time separation of the kernel is not exact. It made the predominant errors in this study. For admissible and inadmissible leaves, we dealt with it by expanding the width of Domain F (detailed in §D) as done in the conventional 2D implementation of FDP [1]. We further improved the accuracy in admissible leaves by adding

LRA of the three-rank tensor (detailed in §D.1, Fig. D.2 (top) (referred to as TCA)). By setting the allowable absolute error (ϵ_{st}) at about 10^{-6} and the additional width of Domain F at about $10\beta\Delta x$, we suppressed the solution error below about 0.3% (Fig. D.2). These modifications did not change the cost largely (Fig. D.2). Our results where 2D specific errors were predominant accuracy controlling factors will suggest that the inherent errors of FDP=H-matrices are small satisfactory.

Throughout the parameter studies, it is demonstrated that FDP=H-matrices are capable of controlling the error with keeping the $N \log N$ cost scaling by tuning the parameters. The parameter dependence of the cost was basically represented by the prefactors of the scaling. Although it is out of our scope to check the further error reduction, FDP=H-matrices will be capable of suppressing the error below given values, as long as the required error bounds are reasonably larger than the initial spatiotemporal discretization errors.

7.2 Potential Implications

We obtained an algorithm for simulating the elastodynamic BIEM at almost $O(N \log N)$ costs both in the time complexity and memory. This allows ST-BIEM to treat the same sized problem with $NM/\log N$ times smaller computational resources, and $NM/\log N$ times larger problems with the same costs, as illustrated in Fig. 17. We here discuss the potential future works and implications of FDP=H-matrices in computations, algorithms, and applications.

While FDP=H-matrices can reduce the memory cost (and the computational complexity) to be of $N \log N/N_*$ for large N (Fig. 17), we did not executed the large scale computation in the numerical experiments in §6 showing the numerical costs. This is in order to avoid considering the other factors concerning the parallelization for evaluating the pure computational complexity and memory cost of this algorithm. The parallel computation of FDP=H-matrices is a future work in the aspect of the computation. Due to the hierarchical divisions to obtain the block cluster tree, computed vectors in FDP=H-matrices have remarkably different sizes ranging from $O(1)$ to $O(N)$ as in H-matrices. Computations of such vectors are known to require careful task assignment to evenly distribute the CPU loads in H-matrices literature [35]. The same consideration will be required in the parallel computation of FDP=H-matrices. It is thus a desirable collaboration to combine FDP=H-matrices with a highly efficient parallel computation library of H-matrices, such as HACApK [36].

Combining adaptive time steps [17] with FDP=H-matrices will be a next step of the algorithm. In addition, in order to eliminate a logarithmic factor from the cost scaling of FDP=H-matrices, FDP=H-matrices may be further combined with some extended H-matrices, such as \mathcal{H}^2 -matrices [37].

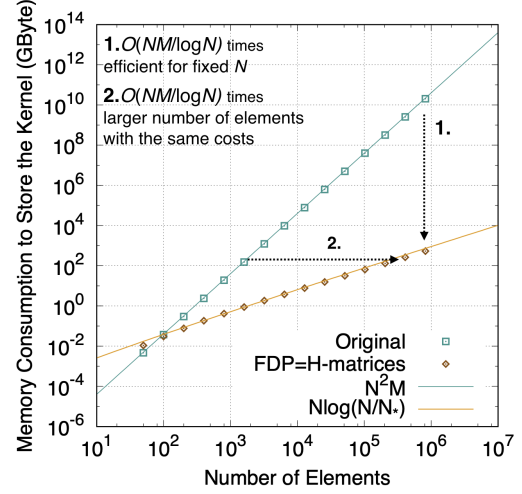


Fig. 17 Memory consumptions to store the kernel in the cases of the original ST-BIEM and of FDP=H-matrices, in the range $10 < N < 10^7$. Numbered arrows represent the cost comparison between the original ST-BIEM and FDP=H-matrices. Parameter values and notations are the same as Fig. 13. Some acceleration techniques, not used in Fig. 13 (introduced for the parameter studies shown in the appendix) are used, so that the cost of FDP=H-matrices is changed by a factor.

Note that ART can reduce the memory cost of the plane-wave time-domain FMM [21] of $O(NM)$ to be of $O(N \log N)$, by using the arithmetic of §5, and can be applied to many particle systems interacting by waves; those will be shown in other places.

FDP=H-matrices have wide applications in realistic (particularly elastodynamic) problems. A simple application of FDP=H-matrices is the 3D dynamic rupture simulation, where the memory storage has been the bottleneck of the modeling [2]. Note that FDP=H-matrices are applicable to BIEM of multi-regions [38] for simulating spatially heterogeneous elastic media. Flexible but high-cost simulations will get broader applications by integrating themselves with FDP=H-matrices of almost $O(N)$ costs.

8 Conclusion

We developed, for the first time, almost $O(N)$ methods for N -elements spatiotemporal boundary integral equation method (ST-BIEM) applicable to transient elastodynamic problems, called the fast domain partitioning hierarchical matrices (FDP=H-matrices). FDP=H-matrices are extensions of the fast domain partitioning method (FDPM) [1, 2] and the hierarchical matrices (H-matrices) [3]. FDP=H-matrices reduce the time complexity of the spatiotemporal convolution and memory consumption to store the integral kernel and convolved variables to be of $O(N \log N)$, while they are of $O(N^2M)$ in the original ST-BIEM. FDP=H-matrices are constructed by combined approximations applied to three domains of FDPM

(detailed in §3). After H-matrices are applied to the source-receiver dependence of the kernel in every domain defined by FDPM, the memory size becomes of $O(N \log N)$ (detailed in §3.2.1 and §3.2.2). After newly extended Quantization is further applied to the kernel, the time complexity becomes of $O(N \log N)$ (detailed in §3.2.3). The approximation by the averaged reduced time (ART) newly extended increases the accuracy of the convolution in FDP=H-matrices (detailed in §4 and §B). Based on these, the arithmetics of FDP=H-matrices were constructed (detailed in §5 and §B). The numerical results in anti-plane crack problems (detailed in §6) demonstrated the significant efficiency and convincing accuracy of FDP=H-matrices as expected from the theoretical evaluation. The parameter dependence of the numerical cost and accuracy were comprehensively studied (detailed in §6, §7, §A.3 and summarized in §7.1).

Acknowledgements We acknowledge helpful discussions with A. Ida, N. Kame, M. Ohtani, and P. Romanet. This study is supported in part by JSPS/MEXT KAKENHI Grant Numbers JP25800253 and JP26109007, and by the “Joint Usage/Research Center for Interdisciplinary Large-scale Information Infrastructures” and “High Performance Computing Infrastructure” in Japan (Project ID: jh180043-NAH).

References

1. R. Ando, N. Kame, T. Yamashita, Earth, planets and space **59**(5), 363 (2007)
2. R. Ando, Geophysical Supplements to the Monthly Notices of the Royal Astronomical Society **207**(2), 833 (2016)
3. W. Hackbusch, Computing **62**(2), 89 (1999)
4. M. Bonnet, Meccanica **34**(4), 301 (1999)
5. C.A. Brebbia, J.C.F. Telles, L.C. Wrobel, *Boundary element techniques: theory and applications in engineering* (Springer Science & Business Media, 2012)
6. M. Fuchs, J. Kastner, M. Wagner, S. Hawes, J.S. Ebersole, Clinical Neurophysiology **113**(5), 702 (2002)
7. A. Sutradhar, G.H. Paulino, L. Gray, Engineering Analysis with Boundary Elements **26**(2), 119 (2002)
8. M.R. Bai, The Journal of the Acoustical Society of America **92**(1), 533 (1992)
9. A. Portela, M. Aliabadi, D. Rooke, International Journal for Numerical Methods in Engineering **33**(6), 1269 (1992)
10. J.R. Rice, Journal of Geophysical Research: Solid Earth **98**(B6), 9885 (1993)
11. H. Aochi, E. Fukuyama, Journal of Geophysical Research: Solid Earth **107**(B2) (2002)
12. R. Ando, K. Imanishi, Y. Panayotopoulos, T. Kobayashi, Earth, Planets and Space **69**(1), 130 (2017)
13. N. Nishimura, Applied mechanics reviews **55**(4), 299 (2002)
14. S.M. Day, L.A. Dalgner, N. Lapusta, Y. Liu, Journal of Geophysical Research: Solid Earth **110**(B12) (2005)
15. T. Tada, T. Yamashita, Geophysical Journal International **130**(2), 269 (1997)
16. G. Perrin, J.R. Rice, G. Zheng, Journal of the Mechanics and Physics of Solids **43**(9), 1461 (1995)
17. N. Lapusta, J.R. Rice, Y. Ben-Zion, G. Zheng, Journal of Geophysical Research: Solid Earth **105**(B10), 23765 (2000)
18. V. Rokhlin, Journal of computational physics **60**(2), 187 (1985)
19. S. Börm, L. Grasedyck, W. Hackbusch, Lecture notes **21**, 2003 (2003)
20. M. Bebendorf, S. Rjasnow, Computing **70**(1), 1 (2003)
21. A.A. Ergin, B. Shanker, E. Michielssen, IEEE Antennas and Propagation Magazine **41**(4), 39 (1999)
22. T. Maruyama, T. Saitoh, T. Bui, S. Hirose, Computer Methods in Applied Mechanics and Engineering **303**, 231 (2016)
23. T. Tada, Geophysical Journal International **164**(3), 653 (2006)
24. H. Yoshikawa, S. Yamamoto, Transactions of the Japan Society for Computational Methods in Engineering **15**, 79 (2015)
25. R.C. Gonzalez, R.E. Woods, Upper Saddle River, NJ (2002)
26. K. Aki, P.G. Richards, *Quantitative seismology* (University Science Books, 2002)
27. A. Cochard, R. Madariaga, pure and applied geophysics **142**(3), 419 (1994)
28. T. Tada, R. Madariaga, International Journal for Numerical Methods in Engineering **50**(1), 227 (2001)
29. T. Tada, E. Fukuyama, R. Madariaga, Computational Mechanics **25**(6), 613 (2000)
30. C. Pelties, J. Puente, J.P. Ampuero, G.B. Brietzke, M. Käser, Journal of Geophysical Research: Solid Earth **117**(B2) (2012)
31. D. Andrews, Journal of Geophysical Research **81**(32), 5679 (1976)
32. L. Grasedyck, Computing **74**(3), 205 (2005)
33. Y. Ida, Journal of Geophysical Research **77**(20), 3796 (1972)
34. M. Ohtani, K. Hirahara, Y. Takahashi, T. Hori, M. Hyodo, H. Nakashima, T. Iwashita, Procedia Computer Science **4**, 1456 (2011)
35. M. Bebendorf, S. Kunis, J. Integral Equations Applications **21**(3), 331 (2009). DOI 10.1216/JIE-2009-21-3-331. URL <http://dx.doi.org/10.1216/JIE-2009-21-3-331>
36. A. Ida, T. Iwashita, T. Mifune, Y. Takahashi, Journal of information processing **22**(4), 642 (2014)
37. W. Hackbusch, S. Börm, Computing **69**(1), 1 (2002)
38. N. Kame, T. Kusakabe, Journal of Applied Mechanics **79**(3), 031017 (2012)
39. I.V. Oseledets, D. Savostianov, E.E. Tyrtshnikov, SIAM Journal on Matrix Analysis and Applications **30**(3), 939 (2008)

A Quantization Method

The quantization method (Quantization) is detailed here. The method implementation is detailed in §A.1. The cost and the accuracy of Quantization is studied in the case that Quantization is singly applied to ST-BIEM in §A.2. The ϵ_Q dependence of FDP=H-matrices is studied to check the effect of Quantization to FDP=H-matrices in §A.3.

A.1 Method Detail

We here suppose to evaluate a temporal convolution T_n in each time step n , where a variable (the slip rate D in this paper) and a kernel K is convolved as

$$T_n = \sum_{m=M_{init}}^{M_{fin}-1} K_m D_{n-m}, \quad (\text{A.1})$$

where $M_{fin}(\leq M)$ is the duration of the original temporal convolution to be quantized; when Quantization is singly used, M_{init} is set at the minimum m making the kernel K_m return a nonzero value, and M_{fin} is the start from which the static approximation is applied at each time step $M_{fin} \leq m < M$. Below, we show the detail of Quantization by applying this simplified convolution.

A.1.1 Implementation

A time range of q ($= 0, 1, 2, \dots$), $b_q \leq m < b_{q+1}$, is recursively determined as the maximum time domain fulfilling the error condition ($|K_m - \hat{K}_q| \leq \epsilon_Q |\hat{K}_q|$ (or $\min[\epsilon_Q |\hat{K}_q|, \epsilon_{st}]$) for arbitrary m in the time range of q), where b_q is the time of the partition of the quantization number q ; ϵ_Q and ϵ_{st} are the parameters of Quantization and \hat{K}_q is the representative value of the kernel in $b_q \leq m < b_{q+1}$. The initial partition position b_0 is set at M_{init} ; At the last time step of the convolution to be quantized, the recursion ends with returning the last time step number M_{fin} as the time step of the last partition of Quantization b_Q , where Q denotes the maximum number of $q + 1$.

The value of \hat{K} is selected largely arbitrary. For example, the kernel K_{b_q} at the start of the (q -th) sampling cluster can be chosen for the representative value, \hat{K}_q ($\hat{K}_q = K_{b_q}$). In this case, we can detect the set of the quantization partitions at the $O(M_{fin} - M_{init})$ time complexity, by defining b_{q+1} as the minimum time step, m , breaking the error condition (that fulfills $|K_m - \hat{K}_q| > \epsilon_Q |\hat{K}_q|$) for each b_q . If \hat{K} is chosen as the kernel at the end of the sampling cluster ($\hat{K}_q = K_{b_{q+1}-1}$), desired clusters can be obtained at the $O(M_{fin} - M_{init})$ complexity by the sequential partition detection starting at the large time step side.

In the anti-plane problem treated in this paper, we defined a \hat{K} value as an approximate kernel average, $\hat{K} = (K_{b_q} + \hat{K}_{b_{q+1}-1})/2$, and set partition b_{q+1} was at the minimum m which satisfies $|K_m - \hat{K}|/2 > \epsilon_Q |\hat{K}_q|$. This approximately satisfies the uniform error condition of Quantization abovementioned, and is compromising the above two partition selection conditions; this satisfies the above two conditions with two times larger ϵ_Q .

A fast efficient computation is achieved by the partial sum, \hat{D} , of the corresponding slip rate D , as in Domain S of FDPM the kernel of which is time independent; q -th slip $\hat{D}_{n,q}$ at the time step n is defined as

$$\hat{D}_{n,q} := \sum_{m=b_q}^{b_{q+1}-1} D_{n-m}. \quad (\text{A.2})$$

Quantization computes the stress convolution as

$$T_n \simeq \sum_{q=0}^{Q-1} \hat{K}_q \hat{D}_{n,q} \quad (\text{A.3})$$

by utilizing the incremental time evolution rule of \hat{D} :

$$\hat{D}_{n,q} = \hat{D}_{n-1,q} + (D_{n-b_q} - D_{n-b_{q+1}}). \quad (\text{A.4})$$

The required memory cost and time complexity for computing T_n and $\hat{D}_{n,q}$ by Eqs. (A.3) and (A.4) are of $O(Q)$.

Additionally, we paid attention to the cumulative errors caused by the time evolution of the quantized slip \hat{D}_q ; the error becomes large particularly when the sampling interval is one ($b_{q+1} - b_q = 1$) when Quantization is applied singly. To reduce the error, we utilized the definition of the q -th slip, Eq. (A.2).

A.1.2 Cost Estimates of Quantization

In the case of the relative error conditions $|K - \hat{K}| < \epsilon_Q |\hat{K}|$, the number of partitions is of $O((a/\epsilon_Q) \log(M_{fin} - M_{init}))$, as long as the kernel is the power-law function $K_m \sim m^a$ of time step m . Note that the absolute error condition becomes asymptotically negligible at distant points, so that the costs become of $O(1)$ when the absolute error condition is solely imposed. When Quantization is singly applied to ST-BIEM of $O(N^2 M)$ costs, the cost becomes of $O(N^2 (a/\epsilon_Q) \log(L))$ by considering the combination of the source and receiver pairs.

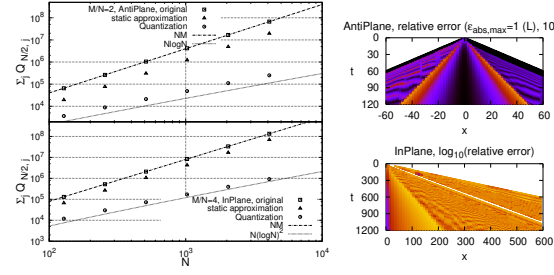


Fig. A.1 Cost scaling and error distribution of Quantization. (Left) The number of elements N versus the number of partitions per receiver in the case of $\epsilon_Q = 0.1$ (10% relative errors), which corresponds to the cost of Quantization divided by the number of elements N . When Quantization is applied, the number of partitions per receiver becomes of almost $O(N)$, which means that the cost becomes of almost $O(N^2)$. (Top right) Anti-plane kernel errors over space x and time t caused by Quantization imposing the relative error condition of $\epsilon_Q = 0.1$ and the absolute error condition (denoted by $\epsilon_{abs,max}$) scaled by $K^{max}_{i,j}$ [1], where $K^{max}_{i,j} := \max_m |K_{i,j,m}|$ denotes the maximum kernel magnitude of an (i, j) pair. A colorbar represents the relative error value. $\epsilon_{abs,max}$ is 1 at $x < 0$ (denoted by L in the figure) and 0.01 at $x > 0$ denoted by R). (Bottom right) In-plane kernel errors over space x and time t when $\epsilon_Q = 0.05$. A colorbar represents the common logarithm of the relative error value.

A.2 Performance Evaluation

The cost reduction and the accuracy of Quantization are investigated below. For simplicity, 2D planar faults are selected as an example. The kernel for the planar fault is written as $K_{i,i,m} = K_{-j,m}$ because of the translational symmetry of the kernel, where we use the same symbol of the kernel between $K_{i,j,m}$ and $K_{-j,m}$.

The unit used in an anti-plane problem studied below is the same as in §6 in the paper. In an in-plane problem studied below, the unit $\beta = 1$ in an anti-plane problem is replaced by $\alpha = 1$ and we set β at $\beta = \alpha/\sqrt{3}$ and the value of the CFL parameter $\alpha \Delta t / \Delta x$ at 1/2.

A.2.1 Cost Reduction

By regarding the original ST-BEIM is a special case of $\epsilon_Q \rightarrow 0$, we can measure the costs of both Quantization and the original BIEM by the number $\sum_{i,j} Q_{i,j}$ of partitions. In the planar fault, the order estimated of the number of partitions is further simplified to $O(N \sum_j Q_{N/2,j})$ due to the translational symmetry abovementioned.

Fig. A.1 (left) shows the number of partitions in the case of $\epsilon_Q = 0.1$. The costs of Quantization, $\sum_{i,j} Q_{i,j}$ times N , was found to be of almost $O(N^2)$ successfully. This is because the time decay of the kernel near the front is the power law function of the elapsed time from the wave arrival in anti-plane cases, where the costs are of $O(N^2 \log N)$. In in-plane cases, the kernel in Domain I is sum of the time-decaying wavefront and the asymptotes in proportion to the powers of the time step. It looks to contribute the additional log factor in the costs $O(N^2 \log^2 N)$ in in-plane cases.

A.2.2 Kernel Accuracy

Fig. A.1 (right) shows the distribution of errors in kernels approximated by Quantization ($|K - \hat{K}|/|K|$). The stripes corresponding to partitions schematically illustrated in Fig. 5 (right). The widths of stripes are broadened as the source-receiver distance increases or the elapsed

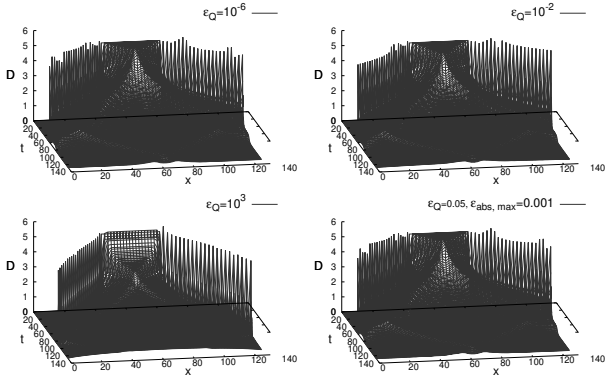


Fig. A.2 Slip rate D evolving over space x and time t solved by Quantization. Approximation parameter values are shown in the figure. The figures of dynamic rupture solutions are thinned out for visualization.

time increases. In the anti-plane problem, Quantization efficiently compresses the enlarged wavefront before the static approximation, corresponding the last partition. In the in-plane problem, Quantization also approximates the nearfield term in Domain I. It is also noteworthy that the relative error is zero around wavefronts. This means Quantization resolves the kernel well even when the temporal change rate in the kernel is large.

A.2.3 Crack Problems

We studied the accuracy of solutions obtained when using Quantization. We here used Crack problems of the simple static-dynamic frictional boundary condition; in this condition, the shear traction is suddenly dropped to the dynamic frictional strength T_{dy} after the shear traction reaches the yielding strength T_{th} . $T_{dy} = 0$ was here set at $T_{dy} = 0$. The initial stress distribution was represented by the single asperity model [27], where the initial stress T_0 is given as the sum of the background stress T_{bg} and a piecewise perturbation such as $T_0(x) = T_{bg} + (T_{th} - T_{bg} + 0)H(x - x_-)H(x_+ - x)$, where $x_+ - x_-$ is a parameter.

Fig. A.2 shows the results obtained when $x_+ - x_- = 40\Delta x$, $T_{th} = 5$, and $T_{bg} = 0$. The increase of ϵ_Q resulted in the decrease of the slip rates at the initially fractured area. In addition, the rupture speed became smaller as ϵ_Q increased. These suggest ϵ_Q damps the solution, as artificial damping does. This is possibly because the solution approaches to the quasi-dynamic approximation (, which replaces the kernel with the sum of the radiation damping term and the static kernel [34],) when ϵ_Q increases; in the quasi-dynamic approximation, the radiated kinetic energy is neglected so that the decrease of the rupture speed and slip rate naturally occur. When the absolute error condition is applied, the solution accuracy increased, even though such absolute error condition becomes gradually negligible as the source and receiver becomes distant.

The maximum slip rates at rupture fronts are almost independent of such damping effect of the kernel quantization. This seems to be understood from the energy balance at the crack tip. The stress drop at the crack tip progresses faster than the strain energy release progressing at the wave speeds, and thus the stress drop balances with the radiation damping not quantized.

A.3 ϵ_Q dependence of FDP=H-matrices

Below, we study how Quantization affects the cost and accuracy of FDP=H-matrices. Because the upper bound of the relative approxima-

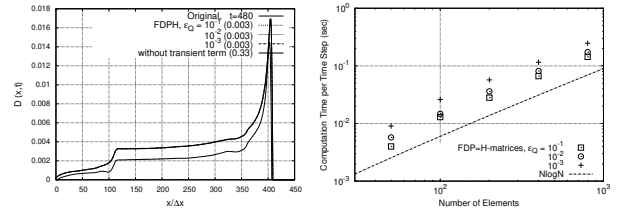


Fig. A.3 Dependencies of accuracy and costs on ϵ_Q in FDP=H-matrices. Parameter values not shown in the figure in the left and right panels are respectively the same as those in the left and right panels in Fig. D.2. (Left) Snapshots of the slip rate D over space x at $t = 480$ in the case of ϵ_Q ranging from 10^{-1} to 10^{-3} or the case without transient term, where FDP = H-matrices are abbreviated as FDPH. The solution accuracy was hardly changed even with ϵ_Q variations. When the transient term is neglected, the error increased markedly. These suggested that the transient term was necessary although ϵ_Q was irrelevant to the accuracy in this case. (Right) Computation costs of FDP=H-matrices is roughly proportional to $1/\epsilon_Q$.

tion error is determined ϵ_Q in Quantization, we investigate the ϵ_Q dependence of the cost and solution accuracy of FDP=H-matrices. In particular, we investigate the effect of Quantization applied to the transient term in Domain S, by using a nonplanar problem studied in §6.2. The same influence of Quantization is expected to the time-dependent part of the Domain I kernel in 3D problems.

Fig. A.3 (left) shows the changes in the snapshots of the slip rate when ϵ_Q varies. Even if ϵ_Q was changed in the range of 0.1 to 0.001, the accuracy degradation was negligible at the first digit of relative errors. It is worth emphasized that the accuracy deterioration seen in Quantization alone (§A.2) does not occur in FDP=H-matrices even when we adopt $\epsilon_Q = 0.1$.

The irrelevance of ϵ_Q apparently seemed largely because the magnitude of the transient term value is suppressed by the increased duration of Domain F, as explained in §D.2. However, when the transient term was ignored, the solution accuracy was greatly deteriorated by 33%, so that the transient term is as large as it contributes to the stress. Probably, the irrelevance of ϵ_Q is caused by the absolute error condition added to the quantization condition (See §D.1). Since ϵ_{st} requires much small values $\epsilon_{st} = 10^{-6}$ to deal with 2D specific errors (detailed in §D), secondarily ϵ_Q would become irrelevant.

The cost showed a roughly linear dependence on $1/\epsilon_Q$ (Fig. A.3, right panel). In the case of Quantization alone, the cost will increase in proportion to $1/\epsilon_Q$ as noted in §A.1. In FDP=H-matrices, the linear dependence of the cost on $1/\epsilon_Q$ is also seen in but weak such that the cost change is three times while ϵ_Q is changed 100 times. This relatively small dependence of the cost on ϵ_Q was probably due to costs of the internal algorithms other than Quantization.

B Arithmetics of FDP=H-matrices in Domains I and S

The arithmetic in Domain F is shown in §5. We here explain the arithmetics in Domains S and I of almost $O(N)$ costs (respectively in §B.1 and §B.2) after the temporal discretization of Domain F (shown in §4.3.1). The arithmetics for transient terms (introduced in §D) in Domains S and I are also explained (respectively in §B.3 and §B.4).

The supplemental information on the cost order is added in §B.5.

B.1 Domain S

The stress response of Domain S, T^S , is written as

$$T_i^S(t) = \sum_j \hat{K}_{i,j}^S \int_{t_j^{\beta+} + \Delta t_j^{\beta+}}^{\infty} d\tau D(t - \tau) \quad (\text{B.1})$$

After ART and H-matrices are applied and after Domain F is temporally discretized as in §4.3, T_i^S is discretized as that of Domain F;

$$T_i^S((n+1)\Delta t + \delta t_i^\beta) \quad (\text{B.2})$$

$$= f_i^S \sum_j g_j^S \sum_{m=-1}^{\infty} D_{j,n-m-\tilde{m}_j^{\beta+}} \int_{\max(\tilde{t}_j^{\beta+}, (m+\tilde{m}_j^{\beta+})\Delta t)}^{(m+1+\tilde{m}_j^{\beta+})\Delta t} d\tau \quad (\text{B.3})$$

$$= f_i^S \sum_j g_j^S \left[\Delta t \sum_{m=0}^{\infty} D_{j,n-m-\tilde{m}_j^{\beta+}} + (\tilde{m}_j^{\beta+} \Delta t - \tilde{t}_j^{\beta+}) D_{j,n-(\tilde{m}_j^{\beta+}-1)} \right]. \quad (\text{B.4})$$

We below detail the case of the interpolation of the left hand side $T_i^S((n+1)\Delta t + \delta t_i^\beta) \approx T_{i,n+\delta m_i^\beta}^S$, as in §4.3.2. See §4.3.2 for the higher order interpolation. The second term is treated as in that of Domain F, so that we focus on the first term (denoted by $T_{i,n}^{S,asy c}$); note that the computation of the second term can be made unnecessary by choosing Δt_j^\pm so as to satisfy $(\tilde{m}_j^{\beta+} \Delta t - \tilde{t}_j^{\beta+}) = 0$ (detailed in §E.3).

$T_{i,n}^{S,asy c}$ is computable incrementally. The increment $\Delta T_{i,n}^{S,asy c}$ of $T_{i,n}^{S,asy c}$, defined as

$$\Delta T_{i,n}^{S,asy c} := T_{i,n}^{S,asy c} - T_{i,n-1}^{S,asy c}, \quad (\text{B.5})$$

satisfies a relation:

$$\Delta T_{i,n}^{S,asy c} = f_i^S \sum_j g_j^S \Delta t D_{j,n-\tilde{m}_j^{\beta+}-\delta m_i^\beta}. \quad (\text{B.6})$$

This relation to express $\Delta T_{i,n}^{S,asy c}$ is the same as Eq. (35) for $T_{i,n}^F$ in Domain F explained in §5 (when \hat{D} in Eq. (35) is regarded as D). Therefore, $\Delta T_{i,n}^{S,asy c}$ is computable by the arithmetic of Domain F described in §5.

B.2 Domain I

After ART and H-matrices are applied as in §4, the stress response of Domain I, T^I , is written as

$$T_i^I(t) = f_i^I \sum_j g_j^I \int_{\delta t_i^\alpha + \tilde{t}_j^{\alpha-}}^{\delta t_i^\beta + \tilde{t}_j^{\beta+}} d\tau h^I(\tau) D_j(t - \tau - \tilde{t}_j). \quad (\text{B.7})$$

Note that the kernel of Domain I in continuous time is separated into two functions both of which are separated into the corresponding spatial parts and temporal parts [2]; the temporal part of one is time invariant as in the Domain S cases, and the other is proportional to the elapsed time. For notational simplicity, we abbreviate the summation of these two functions having different time-dependence. After Domain F is temporally discretized as in §4.3, this convolution is separated into the exactly discretized part and decimal part as

$$T_{i,n}^I = f_i^I \sum_j g_j^I \sum_{m=\delta m_i^\alpha + \tilde{m}_j^{\alpha+}}^{\delta m_i^\beta + \tilde{m}_j^{\beta-}-1} h_m^I D_{j,n-m} + \text{decimal part}, \quad (\text{B.8})$$

where h_m^I is the same as in the discretized temporal part of the kernel in Domain I of FDP, and the explicit form of the remainder (denoted by the decimal part hereafter in §B.2) is shown in §B.2.5. the duration

of the time definition range $(\delta t_i^\beta + \tilde{t}_j^{\beta+}) - (\delta t_i^\alpha + \tilde{t}_j^{\alpha-})$ minus the integer multiple of Δt , and the temporal dependence of the kernel is not h_m^I there.

Below, we first obtain the computation procedures for the first term in Eq. (B.8) step by step in §B.2.1, §B.2.2, §B.2.3 and §B.2.4. Second, we treat the decimal part in §B.2.5.

In this paper, we assume Domain I exists in all admissible leaves for simple implementation. Simple handling of this assumption is detailed in §C.

B.2.1 Decomposed Convolution over Domain I

To begin with, the first term in Eq. (B.8) is represented by the difference of an integral until the time step of the P wave passage from that until the time step of the S wave arrival time:

$$T_{i,n}^I = f_i^I \sum_j g_j^I \left[\sum_{m=m_0^I}^{\delta m_i^\beta + \tilde{m}_j^{\beta-}-1} - \sum_{m=m_0^I}^{\delta m_i^\alpha + \tilde{m}_j^{\alpha+}-1} \right] h_m^I D_{j,n-m} + \text{decimal part}, \quad (\text{B.9})$$

where m_0^I is an appropriate constant such that $m_0^I \leq \min[\delta m_i^\alpha + \tilde{m}_j^{\alpha+}]$. Both the first and second terms in Eq. (B.9) are computed in the same way. Their common computational procedure is explained below by using the following irreducible expression:

$$T_{i,n}^{Ii} = f_i \sum_j g_j \sum_{m=m_0}^{\delta m_i + \tilde{m}_j - 1} h_m D_{j,n-m}, \quad (\text{B.10})$$

where we omitted indices for notational simplicity.

The irreducible expression, Eq. (B.10), is first separated into two parts;

$$T_{i,n}^{Ii} = f_i \sum_j g_j \sum_{m=0}^{\tilde{m}_j^{Ii1} + \tilde{m}_i^{Ii2} - 1} h_{m+m_0} D_{j,n-m-m_0} \quad (\text{B.11})$$

$$= f_i \sum_j g_j \left[\sum_{m=0}^{\tilde{m}_j^{Ii1} - 1} h_{m+m_0} D_{j,n-m-m_0} + \sum_{m=0}^{\tilde{m}_i^{Ii2} - 1} h_{m+m_0+\tilde{m}_j^{Ii1}} D_{j,n-m-m_0-\tilde{m}_j^{Ii1}} \right], \quad (\text{B.12})$$

where \tilde{m}_j^{Ii1} and \tilde{m}_i^{Ii2} are supposed to be some (arbitrary) positive constants that satisfy $\tilde{m}_j^{Ii1} + \tilde{m}_i^{Ii2} + m_0 = \delta m_i + \tilde{m}_j$. Hereafter, \tilde{m}_j^{Ii1} and \tilde{m}_i^{Ii2} are respectively abbreviated to \tilde{m}_j and \tilde{m}_i .

The values \tilde{m}_i and \tilde{m}_j are introduced to make the integral lengths of the first and second terms in Eq. (B.12) nonnegative; δm_i frequently becomes negative. Hereafter we assume that \tilde{m}_i and \tilde{m}_j are adjusted so that their average values are the same value (except for the remainder) in each admissible leaf.

Those two terms of T^{Ii} in Eq. (B.12) are computed separately. The first term and second term in Eq. (B.12) are respectively called T^{Ii1} and T^{Ii2} . The computation procedure of T^{Ii1} is explained in §B.2.2 and §B.2.3. The computation procedure of T^{Ii2} is explained in §B.2.4.

B.2.2 T^{Ii1} Computation in Eq. (B.12) without Quantization

First, similarly to the case of Domain F, we separate the convolution evaluating T^{Ii1} into a computation converting the reference stress \tilde{T}

to the stress T and a computation converting the slip rate D to the reference stress \bar{T} ;

$$T_{i,n}^{Ii1} = f_i \bar{T}_n^{Ii1} \quad (\text{B.13})$$

$$\bar{T}_n^{Ii1} := \sum_j g_j \sum_{m=0}^{\tilde{m}_j-1} h_{m+m_0} D_{j,n-m-m_0}. \quad (\text{B.14})$$

Eq. (B.13) is computable at almost $O(N)$ costs as in H-matrices. On the other hand, Eq. (B.14) contains the time integration whose length is of $O(\text{dist})$ for each j .

We focus on reducing the computation costs of Eq. (B.14). While the number of the sources in an admissible leaf is of $O(\text{diam}^{D_b})$, the number of possible values of $\tilde{m}_j - 1$ is of $O(\text{diam})$, because \tilde{m}_j can be projected onto $\min_j \tilde{m}_j \leq p \leq \max_j \tilde{m}_j$;

$$\bar{T}_n^{Ii1} = \sum_j \left(\sum_{p=\min_j \tilde{m}_j}^{\max_j \tilde{m}_j} \delta_{p,\tilde{m}_j} \right) g_j \sum_{m=0}^{\tilde{m}_j-1} h_{m+m_0} D_{j,n-m-m_0}. \quad (\text{B.15})$$

$$= \sum_{p=\min_j \tilde{m}_j}^{\max_j \tilde{m}_j} \sum_{m=0}^{p-1} h_{m+m_0} \sum_{j|\tilde{m}_j=p} g_j D_{j,n-m-m_0} \quad (\text{B.16})$$

that is

$$\bar{T}_n^{Ii1} = \sum_{p=\min_j \tilde{m}_j}^{\max_j \tilde{m}_j} \sum_{m=0}^{p-1} h_{m+m_0} \Delta \bar{T}_{proj,n-m-m_0,p}^{Ii1} \quad (\text{B.17})$$

with

$$\Delta \bar{T}_{proj,m',p}^{Ii1} := \sum_{j|\tilde{m}_j=p} g_j D_{j,m'}, \quad (\text{B.18})$$

where $\min_j \tilde{m}_j$ and $\max_j \tilde{m}_j$ is the minimum and maximum values of \tilde{m}_j in an admissible leaf. $\Delta \bar{T}_{proj}$ is the partial summation of the inner product between g and D , gathering the contribution from j of the same $\tilde{m}_j = p$ in Eq. (B.14).

Since $\sum_{p=a}^b \sum_{m=0}^{p-1}$ is summed over $(\min \tilde{m}_j \leq p \leq \max \tilde{m}_j) \cap (0 \leq m < \max \tilde{m}_j) \cap (m < p)$, Eq. (B.17) is further reduced to

$$\bar{T}_n^{Ii1} = \sum_{p=\min \tilde{m}_j}^{\max \tilde{m}_j} \sum_{m=0}^{\max \tilde{m}_j-1} H(p-m-0) h_{m+m_0} \Delta \bar{T}_{proj,n-m-m_0,p}^{Ii1} \quad (\text{B.19})$$

$$= \sum_{m=0}^{\max \tilde{m}_j-1} h_{m+m_0} \sum_{p=\max(m+1, \min \tilde{m}_j)}^{\max \tilde{m}_j} \Delta \bar{T}_{proj,n-m-m_0,p}^{Ii1}. \quad (\text{B.20})$$

Equivalently,

$$\bar{T}_n^{Ii1} = \sum_{m=0}^{\max \tilde{m}_j-1} h_{m+m_0} \Delta \bar{T}_{sum,n,m+m_0,m}^{Ii1} \quad (\text{B.21})$$

with

$$\Delta \bar{T}_{sum,n,m',m}^{Ii1} := \sum_{p=\max(m+1, \min \tilde{m}_j)}^{\max \tilde{m}_j} \Delta \bar{T}_{proj,n-m',p}^{Ii1}. \quad (\text{B.22})$$

$\Delta \bar{T}_{proj,m',p}^{Ii1}$ is summed to $\Delta \bar{T}_{sum,m',m}^{Ii1}$ within the range of p larger than m . $\Delta \bar{T}_{sum,n-m-m_0,m}^{Ii1}$ is convolved with h_{m+m_0} to evaluate \bar{T}_n^{Ii1} .

The process of computing \bar{T}^{Ii1} without Quantization is then summarized as follows. After \mathbf{D}_n is determined, Eq. (B.18) is computed in each time step n to convert $D_{j,n}$ of all j to $\Delta \bar{T}_{proj,n,p}$ of all p in the following way;

$$\Delta \bar{T}_{proj,n}^{Ii1} = G^{Ii1} \mathbf{D}_n \quad (\text{B.23})$$

with

$$G_{p,j}^{Ii1} := \delta_{p,\tilde{m}_j} g_j, \quad (\text{B.24})$$

where $\Delta \bar{T}_{proj,n}^{Ii1} = (\Delta \bar{T}_{proj,n,\min \tilde{m}_j}, \dots, \Delta \bar{T}_{proj,n,\max \tilde{m}_j})^T$ containing $\Delta \bar{T}_{proj,n,p}^{Ii1}$ at the p component. It is a parallel way to the conversion of \bar{D} to \bar{T} in Domain F shown §5.2. $\bar{T}_{sum,n,m}^{Ii1}$ is then sequentially computed for all m in each time step n by using a recurrence formula,

$$\Delta \bar{T}_{sum,n,m}^{Ii1} = \Delta \bar{T}_{sum,n,m+1}^{Ii1} + \Delta \bar{T}_{proj,n,m+1}^{Ii1}. \quad (\text{B.25})$$

$\Delta \bar{T}_{sum,n,m',m}^{Ii1}$ is stored over $m_0 \leq m' < m_0 + \tilde{m}_j$ by using $\Delta \bar{T}_{sum,n,m}^{Ii1} = \mathcal{M} \Delta \bar{T}_{sum,n,m'}^{Ii1}$ for evaluating \bar{T}_n^{Ii1} by Eq. (B.21), where $\Delta \bar{T}_{sum,n,m}^{Ii1}$ is the reference stress of $\Delta \bar{T}_{sum,n,m',m}^{Ii1}$ containing $\Delta \bar{T}_{sum,n,m',m}^{Ii1}$ at the m' component. The computational complexity of the above is of almost $O(N)$. Dominant memory cost is to store $\bar{T}_{sum,n,m',m}^{Ii1}$ in $m_0 \leq m' < m_0 + \tilde{m}_j$ and $0 \leq m < \max \tilde{m}_j$ being of $O(\text{dist}^2)$ capable of amounting to almost $O(N^{2/D_b})$. The other memory cost is of almost $O(N)$.

B.2.3 T^{Ii1} Computation in Eq. (B.12) with Quantization

The computation of T^{Ii1} without Quantization, shown in §B.2.2, requires the memory cost of $O(\text{dist}^2)$ to store $\Delta \bar{T}_{sum,n,m',m}^{Ii1}$. Such a memory cost can be of $O(N^{2/D_b})$, which is of $O(N^2)$ when $D_b = 1$. Below, we quantize the temporal integral in Eq. (B.17) to make the $O(\text{dist}^2)$ history of $\Delta \bar{T}_{sum}^{Ii1}$ unnecessary.

First we quantize h . Quantization of the function h_{m+m_0} determines the positions b_1, \dots, b_Q in the maximum integration range of T^{Ii1} , $m \in [0, \max_j \tilde{m}_j)$. A quantized variable $\Delta \hat{T}_{n,q}^{Ii1}$ of the quantization number q is next defined at the current time step n by considering the p dependent integration range as

$$\Delta \hat{T}_{n,q}^{Ii1} := \sum_{p=\min_j \tilde{m}_j}^{\max_j \tilde{m}_j} \sum_{m|(b_q \leq m < b_{q+1}) \cap (0 \leq m < p)} \Delta \bar{T}_{proj,n-m-m_0,p}^{Ii1} \quad (\text{B.26})$$

$\Delta \hat{T}^{Ii1}$ reduces the \bar{T}_n^{Ii1} convolution in Eq. (B.17) to

$$\bar{T}_n^{Ii1} \approx \sum_q \hat{h}_q \Delta \hat{T}_{n,q}^{Ii1}, \quad (\text{B.27})$$

where \hat{h}_q is the quantized h_{m+m_0} at the q -th interval.

The quantized variable $\Delta \hat{T}_{n,q}$ is stored only at the current time step n , and the history of $\Delta \hat{T}_{n,q}$ is represented by the time increment of $\Delta \hat{T}_{n,q}$:

$$\delta \hat{T}_{n,q}^{Ii1} := \Delta \hat{T}_{n,q} - \Delta \hat{T}_{n-1,q}. \quad (\text{B.28})$$

To evaluate $\delta \hat{T}_n$ explicitly, the following another form of $\Delta \hat{T}_{n,q}^{Ii1}$ is useful;

$$\Delta \hat{T}_{n,q}^{Ii1} = \sum_{p=\min_j \tilde{m}_j}^{\max_j \tilde{m}_j} H(p-b_q-0) \sum_{m|b_q \leq m < \min(b_{q+1}, p)} \Delta \bar{T}_{proj,n-m-m_0,p}^{Ii1}. \quad (\text{B.29})$$

Eq.(B.29) expresses edges of integration on m for each p as Eq. (A.2) in the original Quantization. As in Eq. (A.4), $\delta \hat{T}_n$ is shown to be made of contributions from those edges as

$$\delta \hat{T}_{n,q}^{Ii1} = \sum_{p=\min_j \tilde{m}_j}^{\max_j \tilde{m}_j} H(p-b_q-0) (\delta m_{b_q} - \delta m_{\min(b_{q+1}, p)}) \Delta \bar{T}_{proj,n-m,p} \quad (\text{B.30})$$

$$= \sum_{p=\min_j \tilde{m}_j}^{\max_j \tilde{m}_j} [H(p-b_q-0) \delta m_{b_q} - H(p-b_{q+1}-0) \delta m_{b_{q+1}} + H(p-b_q-0) H(b_{q+1}-p+0) \delta m_p] \Delta \bar{T}_{proj,n-m,p} \quad (\text{B.31})$$

where $\min(b_{q+1}, p)$ is conditioned into two cases ($q > b_{q+1} \cup q \leq b_{q+1}$) in the transform to obtain the last line. By using $\bar{T}_{sum, m', m}^{Ii1}$, this becomes

$$\delta \hat{T}_{n, q}^{Ii1} = \Delta \bar{T}_{sum, n, b_q+m_0, b_q}^{Ii1} - \Delta \bar{T}_{sum, n, b_{q+1}+m_0, b_{q+1}}^{Ii1} + H(b_{q+1} - \min \tilde{m}_j + 0) \sum_{p=b_q+1}^{b_{q+1}} \Delta \bar{T}_{proj, n-p-m_0, p} \quad (B.32)$$

$\delta \hat{T}_{n, q}^{Ii1}$ is computed by using the sparse matrices as \bar{T} in Domain F. The explicit form of the sparse matrix computation is derived by comparing the following two tensorial expressions:

$$\delta \hat{T}_{n, q}^{Ii1} = \sum_{q'} \sum_m (\delta_{q, q'} - \delta_{q+1, q'}) \delta_{m, b_q+m_0} \Delta \bar{T}_{sum, n, m, b_q}^{Ii1} + H(b_{q+1} - \min \tilde{m}_j + 0) \sum_{p, m} \delta_{m, p+m_0} \times [H(p - b_q + 0) - H(p - b_{q+1} + 0)] \Delta \bar{T}_{proj, n-m, p}^{Ii1} \quad (B.33)$$

of $\delta \hat{T}_{n, q}^{Ii1}$, and $\bar{T}_n := \sum_{j, m} \delta_{m, \tilde{m}_j} g_j \hat{D}_{j, m}$ of Eq. (36) giving the sparse matrix computation Eq. (44). After we define

$$\Delta \bar{T}_{sumQ, n}^{Ii1} := (\Delta \bar{T}_{sum, n, 0, b_0}^{Ii1}, \dots, \Delta \bar{T}_{sum, n, 0, b_Q}^{Ii1})^T \quad (B.34)$$

containing $\Delta \bar{T}_{sum, n, 0, b_q}^{Ii1}$ at the q -th component, the computation of the (pseudo) reference vector $\delta \hat{T}_{n, q}^{Ii1}$ (in the way described in §5.2) at the time step n for the q -th quantization number is expressed as

$$\delta \hat{T}_{n+1, q}^{Ii1} = \mathcal{M}[\delta \hat{T}_{n, q}^{Ii1} + \mathcal{T}_q \Delta \bar{T}_{sumQ, n}^{Ii1} + \mathcal{P}_q \Delta \bar{T}_{proj, n}^{Ii1}] \quad (B.35)$$

with sparse matrices:

$$(\mathcal{T}_q)_{m, q'} := \delta_{-m', b_q'+m_0} (\delta_{q, q'} - \delta_{q+1, q'}) \quad (B.36)$$

$$(\mathcal{P}_q)_{m, p} := H(b_{q+1} - \min \tilde{m}_j + 0) \times \delta_{-m, p+m_0} [H(p - b_q + 0) - H(p - b_{q+1} + 0)]. \quad (B.37)$$

Note that the contribution from $\Delta \bar{T}_{proj, n}^{Ii1}$ to $\delta \hat{T}_{n+1, q}^{Ii1}$ of all q is computed with $O(dist)$ costs (not $O(Qdist)$ costs) at each time step n , because $\Delta \bar{T}_{proj, n, p}^{Ii1}$ of each p contributes to single q such that $b_q \leq p < b_{q+1}$; $\mathcal{M} \delta \hat{T}_{n, q}^{Ii1}$ is computable at $O(1)$ costs for each q and n , as detailed in B.5.

Last, we explain the arithmetic for T^{Ii1} computations with Quantization below. $\Delta \bar{T}_{proj, n, p}$ and $\bar{T}_{sum, n, m}^{Ii1}$ are computed for all p and m in each time step n , as in the computations without Quantization (explained in §B.2.3). Next, instead of storing $\bar{T}_{sum, n, m', m}^{Ii1}$, $\delta \hat{T}_n^{Ii1}$ is updated to $\delta \hat{T}_{n+1}^{Ii1}$ by using Eq. (B.35). $\Delta \bar{T}_{n, q}^{Ii1}$ of all q then evolves to $\Delta \bar{T}_{n+1, q}^{Ii1}$ by using $\Delta \bar{T}_{n+1, q}^{Ii1} = \Delta \bar{T}_{n, q}^{Ii1} + \delta \hat{T}_{n+1, q}^{Ii1}$. Eq. (B.27) converts $\hat{T}_{n+1, q}^{Ii1}$ to \bar{T}_{n+1}^{Ii1} at the time step $n+1$. Finally, Eq. (B.13) converts \bar{T}_{n+1}^{Ii1} to $T_{i, n+1}^{Ii1}$ for any i at the time step $n+1$. By using $T_{n+1, i}^{Ii1}$ for any i , we evaluate the slip rate \mathbf{D}_{n+1} at the time step $n+1$. Then the same procedure computing $T_{i, n+1}$ is repeated at the time step $n+1$.

B.2.4 T^{Ii2} Computation in Eq. (B.12)

The i, n component of T^{Ii2} is written as

$$T_{i, n}^{Ii2} = f_i \sum_{m=0}^{\tilde{m}_i-1} h_{m+m_0+\tilde{m}_j} \sum_j g_j D_{j, n-m-m_0-\tilde{m}_j}. \quad (B.38)$$

The functional forms of $h(t)$ ($h^I(t)$) in continuous time are the power functions of the time; the time invariant part is here regarded as the power function of zero power. In the time-dependent part, $h^I(t)$ is written as $h(t) = C_{h0} + 3C_{h1}t^2$ (or $h(t) = 1$) [1, 2], where C_{h0}, C_{h1} are constants and the superscript I is abbreviated. This makes m, j dependence of $h_{m+m_0+\tilde{m}_j} g_j$ separable. For example, in the time invariant

part, $h_{m+m_0+\tilde{m}_j} = \Delta t$. In the temporal discretization adopted in §4.3, $h(t)$ in the time-dependent part is discretized as $h_m = \int_{m\Delta t}^{(m+1)\Delta t} dt h(t)$, and $h_{m+m_0+\tilde{m}_j} g_j$ can be represented by $h_{m+m_0+\tilde{m}_j} g_j = h_{1, m} g_j + h_{2, m} g_j \tilde{m}_j + h_{3, m} g_j \tilde{m}_j^2$ with $h_{1, m} := C_{h0}\Delta t + C_{h1}(\Delta t)^3[3(m+m_0)^2 + 3(m+m_0)+1]$, $h_{2, m} := C_{h1}(\Delta t)^3[6(m+m_0)+3]$, and $h_{3, m} := 3C_{h1}(\Delta t)^3$. Because of this separable m, j dependence of $h_{m+m_0+\tilde{m}_j} g_j$, we can rewrite the computation of T^{Ii2} as

$$T_{i, n}^{Ii2} = f_i \sum_{m=0}^{\tilde{m}_i-1} \sum_d h_{d, m} \sum_j g_{d, j} D_{j, n-m-m_0-\tilde{m}_j} \quad (B.39)$$

with some coefficients of $h_{d, m}, g_{d, j}$ for $d = 1, \dots, d_{max}$, where d_{max} is a constant of $O(1)$. Eq. (B.39) is decomposed into three equations:

$$\Delta \bar{T}_{n, d, m} := \sum_j g_{d, j} D_{j, n-m-m_0-\tilde{m}_j} \quad (B.40)$$

$$\bar{T}_{n, \tilde{m}} := \sum_{m=0}^{\tilde{m}} \sum_d h_{d, m} \Delta \bar{T}_{n, d, m} \quad (B.41)$$

$$T_{i, n}^{Ii2} = f_i \bar{T}_{n, \tilde{m}_i}. \quad (B.42)$$

The decomposed T^{Ii2} computations are treated as follows. First, $\bar{T}_{n, m}$ is computed in each step n for all $0 < \tilde{m} \leq \max_i \tilde{m}_i$ incrementally by using $\bar{T}_{n, \tilde{m}} = \bar{T}_{n, \tilde{m}-1} + \sum_d h_{d, \tilde{m}+m_0} \Delta \bar{T}_{n, d, \tilde{m}}$, where $\max_i \tilde{m}_i$ represents the maximum \tilde{m}_i in the leaf; the history of $\bar{T}_{n, m}$ is not stored. Second, Eq. (B.42) computes $T_{i, n}^{Ii2}$ for all receivers i at time step n , and \mathbf{D}_n is determined. Third, $\Delta \bar{T}_{d, n}^{Ii2} = (\dots, \Delta \bar{T}_{n, d, 0}^{Ii2}, \Delta \bar{T}_{n, d, 1}^{Ii2}, \dots)^T$ is introduced for each d as the (pseudo) reference vector defined in §5.2, and Eq. (B.40) evolves $\Delta \bar{T}_{d, n}^{Ii2}$ to $\Delta \bar{T}_{d, n+1}^{Ii2}$ by using \mathbf{D}_n :

$$\Delta \bar{T}_{d, n+1}^{Ii2} = \mathcal{M}[\Delta \bar{T}_{d, n}^{Ii2} + G^{Ii2} \mathbf{D}_n] \quad (B.43)$$

with

$$G_{m, j}^{Ii2} := \delta_{-m, m_0+\tilde{m}_j} g_j \quad (B.44)$$

for all d in each step n .

B.2.5 Decimal Part Computation in Eq. (B.8)

The decimal part of the stress response of Domain I, T^I Eq. (B.8) is represented as

decimal part =

$$f_i \sum_j g_j^I \left[\int_{(\tilde{m}_j^{\beta-} + \delta m_i^{\beta}) \Delta t}^{\tilde{t}_j^{\beta-} + \delta t_i^{\beta}} - \int_{(\tilde{m}_j^{\alpha+} + \delta m_i^{\alpha}) \Delta t}^{\tilde{t}_j^{\alpha+} + \delta t_i^{\alpha}} \right] dsh^I(s) D_j(t-s). \quad (B.45)$$

Note that δm_i represents the integer part of $\delta t_i / \Delta t$ as in §4.3.2.

The decimal part of Domain I is neglected when the following rounding rule is satisfied;

$$\delta t_i = \delta m_i \Delta t \quad (B.46)$$

$$\tilde{t}_j^{\alpha} = \tilde{m}_j^{\alpha+} \Delta t - \Delta t_j^{\alpha+} \quad (B.47)$$

$$\tilde{t}_j^{\beta} = \tilde{m}_j^{\beta-} \Delta t + \Delta t_j^{\beta-} \quad (B.48)$$

Note that δm_i and \tilde{m}_j^{\pm} are defined in §4.3. $O(\Delta t)$ errors in the travel time caused by these roundings can be regarded as a small fraction of the travel time separation, as in §4.3.2. Such $O(\Delta t)$ errors are negligible in the constant η scheme (explained in §4.3.2). The constant $\eta^2 dist$ scheme can require to treat the decimal part more carefully.

For evaluating the decimal part if it is nonzero, we separate i, j dependence of the integrated h as done in §B.2.4;

$$\text{decimal part} = f_i^I \sum_j g_j^I \sum_d \times$$

$$[h_{d, i}^{I, \alpha, r} h_{d, j}^{I, \alpha, s} D_{j, n-\delta m_i^{\beta-}-\tilde{m}_j^{\beta-}} - h_{d, i}^{I, \beta, r} h_{d, j}^{I, \beta, s} D_{j, n-\delta m_i^{\alpha+}-\tilde{m}_j^{\alpha+}}] \quad (B.49)$$

where $h_{d, i}^{I, c, r}, h_{d, j}^{I, c, s}$ ($c = \alpha, \beta$) are respectively some d -th coefficients depending on the receiver i and the source j . Two terms in Eq. (B.49) are computed by the arithmetic in Domain F described in §B.5.

B.3 Transient Terms in Domain S

The stress caused by the transient term in Domain S is written in the following form:

$$T_{i,n}^{S,tr} := f_i^{S,tr} \sum_j g_j^{S,tr} \sum_{m=0}^{\Delta m_{S,tr}-1} h_m^{S,tr} D_{j,n-m-\tilde{m}_j^{\beta+}-\delta m_i^{\beta}}. \quad (\text{B.50})$$

The cutoff $\Delta m^{S,tr}$ is determined by the given error conditions explained in §D. When the $\Delta m^{S,tr}$ value given by the error conditions is larger than the number of the whole time step (M), $\Delta m^{S,tr}$ can be set at M . In this paper, such truncation is done in §6.3, §D to carefully check the parameter dependence of the cost.

$T^{S,tr}$ is decomposed by the similar procedure to that of Domain I (§B.2) as

$$T_{i,n}^{S,tr} = f_i^{S,tr} \bar{T}_{n,\delta m_i^{\beta}}^{S,tr} \quad (\text{B.51})$$

$$\Delta \bar{T}_{n,m}^{S,tr} := \sum_j g_j^{S,tr} D_{j,n-m-\tilde{m}_j^{\beta+}} \quad (\text{B.52})$$

$$\bar{T}_{n,m}^{S,tr} := \sum_{m'=0}^{\Delta m_{S,tr}-1} h_{m'}^{S,tr} \Delta \bar{T}_{n-m,m'}^{S,tr}. \quad (\text{B.53})$$

It is noticed that \bar{T} to T computation in Eq. (B.51) and D to $\Delta \bar{T}$ computation in Eq. (B.52) are respectively the same as the \bar{T} to T computation and \hat{D} to \bar{T} computation detailed in §B.5. We thus focus on the new computation, Eq. (B.53).

Eq. (B.53) is computable simply by the combination of the direct computation of Eq. (B.53) and the time marching. We first compute the temporal convolution of $\Delta \bar{T} \rightarrow \bar{T}$ in Eq. (B.53) at every time step only for particular m that is the latest time finishing the summation of $\Delta \bar{T}$; it is $m = \min_j \tilde{m}_j^-$ (or later) after the computation of Eq. (B.52) similar to $\hat{D} \rightarrow \bar{T}$ detailed in §B.5. This is to avoid using the incomplete-summation part of \bar{T} in the arithmetics. Later \bar{T} whose m satisfying $m > \min_j \tilde{m}_j^-$ are computed by the time marching rule: $\bar{T}_{m,n+1} = \bar{T}_{m-1,n} + \mathbf{M} \bar{T}_n$.

Quantization can be applied to $h^{S,tr}$ in Eq. (B.53). Although it does not change the cost order, the memory access becomes more efficient by Quantization. In §A.3, Quantization is applied to the transient term in Domain S to check the error property of Quantization applied to FDP=H-matrices.

B.4 Transient Terms in Domain I

In 2D problems, the kernel in Domain I has deviation from the asymptote at the finite elapsed time as in Domain S. Since the kernel is non-singular in Domain I (in-between P and S wavefronts), such transience in the kernel is well approximated by the LRA, such as the Tucker cross approximation (TCA) [39], applied to the tensor representing the spatiotemporal dependence of the kernel. When the LRA is applied to the transient terms (or the original kernel) in Domain I, the resultant reduced kernel are in the same form $f_i g_j h_m$ as that of the asymptote, and has the preferable time dependence for Quantization, as shown in §A.2. Considering these, we can treat the kernel in Domain I in the same way as the Domain I computation shown in §B.2, even if the transient terms are contaminated in 2D problems.

B.5 Summary Information on the Time Complexity and Memory Consumption

We now fully detailed the arithmetics of FDP=H-matrices in Domains I and S (and F). Below, we supplement the cost estimates to that in §4.2.2.

The memory and computation costs of the whole computations in FDP=H-matrices are estimated to be of $O(l_a(N_a + Q_a + Q_a \text{dist}'_a + \text{dist}'_a)) (= O(N_a))$ in an admissible leaf a , where l_a is the rank of \hat{K}^W summed over $W=\text{Fp}, \text{I}, \text{Fs}, \text{S}$, and Q_a is the number of the sampling for Quantization; $\text{dist}'_a := \text{dist}_a/(\beta \Delta t)$. $Q_a \text{dist}'_a$ dependent cost is caused only from Domain I.

Note that $O(\text{dist}'_a, Q_a \text{dist}'_a)$ included in the computation costs can be discarded. This factor is caused by the multiplication of the marching matrix \mathbf{M} (defined in §5, corresponding to the time marching) and the time integration in Domains I. Concerning the multiplication of \mathbf{M} , the multiplication of \mathbf{M} to \bar{T} can be represented simply by a memory increment of the start address of \bar{T} vector in numerics. Discarding $O(\sum_a \text{dist}'_a)$ may be useful when $L' \neq O(N^{1/D_b})$ such as the case handling excessively distant two objects, where the cost estimate becomes of almost $O(L')$.

Q_a is set of $O(\log \text{dist}'_a)$, l_a is of $O(1)$. Although Q_a is of $1/\epsilon_Q$, ϵ_Q can be set at large value by using the absolute error condition as done in this paper (supplemented in §7.1). $\sum_a \text{dist}'_a$ is of almost $O(N)$ as long as $L' = O(N^{1/D_b})$, the assumption thoroughly adopted in this paper, is satisfied.

By considering above, the costs become of $O(N \log N + L' \log N)$ in the constant η scheme, and $O(N^{3/2} + NL')$ in the constant $\eta^2 \text{dist}$ scheme, except for the case of in-plane problem of $D_b = 1$, where $L' := L/(\beta \Delta t)$. In the case of in-plane problem of $D_b = 1$, the memory costs become $O(N \log N + L' \log N \log L')$ in the constant η scheme, and others are unchanged from those of the other cases. Note that the Quantization in Domain I lowers the memory cost only in the case of in-plane problem of $D_b = 1$. In other cases (anti-plane or $D_b = 2, 3$) which is typical in 3D problems firstly intended, the cost is of $O(N \log N)$ in the constant η scheme and of $O(NL)$ in the constant $\eta^2 \text{dist}$ scheme, without Quantization.

C Clustering and Computations in Inadmissible Leaves

C.1 Additional Requirements When Selecting the Admissible Leaves for Domain I to exist

For simple implementation, we assumed Domain I exists in all the interaction of admissible leaves. This corresponds to separate Domains Fp and Fs in all the admissible leaves. Such a condition is represented by an additional requirement in the admissible leaves (as $t_{ij}^{\alpha} + \Delta t_{ij}^{\alpha+} + C_s \Delta t < t_{ij}^{\beta} - \Delta t_{ij}^{\beta-}$, where the factor C_s is a safe coefficient to deal with the temporal discretization (of $O(1)$ and ≥ 2 for the computation done in §B.2)).

One simple way of fulfilling this separation condition between Fp and Fs is to set a constraint on l_{\min} depending a given η value. The explicit condition is obtained by considering the most demanding condition where source and receiver elements are the closest, as below. In the way of clustering we adopted (defined in §4.2), the shortest distance between the collocation points of the source and receiver elements in an admissible leaf is given by $\max(\Delta x_i, \Delta x_j) + l_{\min}/\eta$ for the receiver i and the source j . The condition to separate Fp and Fs in such the worst case in admissible leaves is given by $l_{\min} > -\eta \Delta x' + \eta(\beta^{-1} - \alpha^{-1})^{-1}[\Delta t_j^{\alpha+} + \Delta t_j^{\alpha+} + C_s \Delta t]$, where $\Delta x'$ is the maximum of Δx_i for the receiver i and Δx_j for the source j . Since the most demanding condition is represented by the parameters initially imposed, as long as η and l_{\min} satisfy this relation, the Domain I exist in all admissible leaves even if we keep the ordinary admissibility condition. Note that η in this equation is changed to η_0 in the constant $\eta^2 \text{dist}$ scheme case explained in §4.2.2.

C.2 Arithmetics of FDP=H-matrices in Inadmissible Leaves

The partial kernels of inadmissible leaves are not spatially approximated as in H-matrices for static problems (mentioned in §2.3). Kernels of inadmissible leaves are approximated only temporally. In inadmissible leaves, the time region of the convolution is merely divided into Domain S and the others (regarded as Domain F hereafter). This is because Domains Fp, I, and Fs in continuous time are inevitably contaminated in one time step in some inadmissible leaves. After the kernel is separated into Domains S and F, the kernel is replaced to the time-independent static asymptote in Domain S by FDPM. The computation for the stress response of Domain S in an inadmissible leaf is the same as that in the Domain S of FDPM [2]. The computation of stress response of Domain F in an inadmissible leaf is the same as that in the original ST-BIEM.

D Handling of Errors Specific to 2D Problems

Only in 2D problems, as mentioned in §2.2, the error arises when FDPM spatiotemporally separates the kernel in Domains I and S [1]. This is because an infinitely long line source assumed in 2D problems produces the long temporal tail of the kernel.

It should be re-emphasized that the accuracy deterioration caused by the spatiotemporal separation of the kernel does not occur in 3D problems that simulate finite-sized sources. Therefore, FDP=H-matrices will work better in 3D problems, which will be demonstrated in other places.

To keep the accuracy of FDP=H-matrices in 2D problems, we introduced additional techniques explained in §D.1. There are two tuning parameters of such techniques: the width of Domain F and the upper bound of the absolute error, ϵ_{st} . Their influences to the accuracy and cost are also investigated. The effect of the width of Domain F is shown in §D.2, and that of ϵ_{st} is shown in §D.3.

D.1 Handling 2D Specific Errors Caused by Spatiotemporal Separation of the Kernel

We here explain the way to reduce the 2D specific error in FDP=H-matrices caused by the spatiotemporal separation of the kernel in FDPM.

In the original FDPM, the error caused by the spatiotemporal separation of the kernel is dealt by enlargement of the temporal distance ($\Delta t_{(j)}^+$, represented by Eq. (6)) between the travel time and the end of Domain F (corresponding to the substantial wave passage completion) [1]. The increment of the duration is called additional width in this paper. This enlargement in duration of Domain F allows FDPM to regulate the error below given small values with keeping the fast arithmetic of FDPM. However, such broadening of Domain F can deteriorate the approximation accuracy of the degenerating normalized waveform (Eq. (24)) in FDP=H-matrices. This is because the approximation of normalized waveforms by ART depends on the duration of Domain F (See Eq. (24)). Another way is thus required, in order to keep the accuracy of the degenerating normalized waveform.

We utilized a temporal property of the kernel that the kernel is described by powers of the time (elapsed from the wavefronts or the wave radiation) in Domains I and S, as seen in the analytic form of the kernel [28]. The kernel in these domains are thus well approximated by LRA temporally as well as in spatial directions; indeed, the spatiotemporal variable separation of FDPM is regarded as the (analytic) LRA where the number of vectors in the temporal direction (hereafter called the rank in the temporal direction) is one in Domain S and two in Domain I.

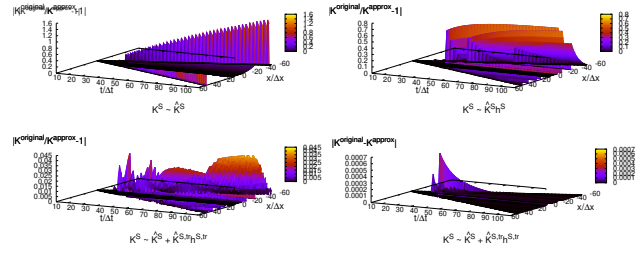


Fig. D.1 Error distributions in the approximate kernels of different temporal ranks, in a 2D planar fault case. The kernel K^{approx} approximated by TCA is compared with the original kernel $K^{original}$ in the figure. Used approximation parameters are $\epsilon_Q = \epsilon_{ACA} = \epsilon_{st} = 10^{-3}$, $l_{min}/\Delta x = 5$, and $\eta = 5.67$ and the temporal distance between the travel time and the end of Domain F is enlarged by $3\Delta x/\beta$. The accuracy is improved greatly when the temporal ranks of the kernel increases. (Top left) Relative error in the case of the asymptotic kernel, being a special case of the temporally first rank. (Top right) Relative error in the case of the temporally first rank, where the pivot time is set at the start of Domain S. (Bottom left) Relative error in the case of the temporally second rank. (Bottom right) Absolute error in the case of the temporally second rank, normalized by the radiation damping term.

In this paper, the 2D kernel in Domain S (and in Domain I in the arithmetic shown in §B) in admissible leaves are approximated by the Tucker cross approximation (TCA) [39], one of the fast approximate LRA technique. This approximates the third order tensor representing the receiver-source-time dependency to a low rank form, that is, the sum of vector products of the time-dependent one, source-dependent one, and the receiver-dependent one.

On the other hand in the inadmissible leaves, the start of the Domain S is elongated to dealing the error, in this paper; the kernel in Domain I is not spatiotemporally separated as in Domain F in inadmissible leaves (See §C). The start of Domain S in inadmissible leaves is set as a time step after which the relative and absolute errors are respectively smaller than ϵ_Q and ϵ_{st} , between the original kernel and the Domain S asymptote.

The numerical test of this error criteria is shown in Fig. D.1. It shows the error in the kernel after the above temporal approximations are imposed, in the case of a planar fault; the used parameters are listed in the caption. The static approximation the original FDPM adopted (denoted by $K^S \sim \hat{K}^S$) had almost 100% relative errors when $\Delta t^+ / (\beta \Delta x)$ is on the order of 1. The case of the temporally first rank (denoted by $K^S \sim \hat{K}^S h^{S, tr}$, and detailed in Fig. D.1) also had almost 100% relative errors. Such numerical errors was greatly reduced in the case of the temporally second rank (denoted by $K^S \sim \hat{K}^S + \hat{K}^{S, tr} h^{S, tr}$). The relative error became on the order of 1%, and the absolute error becomes further smaller and on the order of 10^{-5} .

The approximation accuracy can improve as the rank of the temporal direction increases as above. The great accuracy improvement of $K \sim \hat{K}^S + \hat{K}^{S, tr} h^{S, tr}$ in Fig. D.1 (bottom) may be consistent with the property of the 2D kernel in Domain S comprising the static term (\hat{K}^S) and the long temporal tails roughly decaying in proportion to the inverse root of the elapsed time.

By considering these results, we both used the TCA of the temporally second rank ($K^S \sim \hat{K}^S + \hat{K}^{S, tr} h^{S, tr}$) and the additional width of Domain F in this paper. In order to introduce the time-dependent kernel in Domain S with a finite cost, we determined the time step after which the time-dependent part of the kernel is discarded. Such a time step was set at a time step by the same condition as that for determining the start of Domain S in inadmissible leaves. Note that we did not introduce further higher orders of TCA, because the error was mostly caused by the spatially close block clusters corresponding to inadmissible leaves

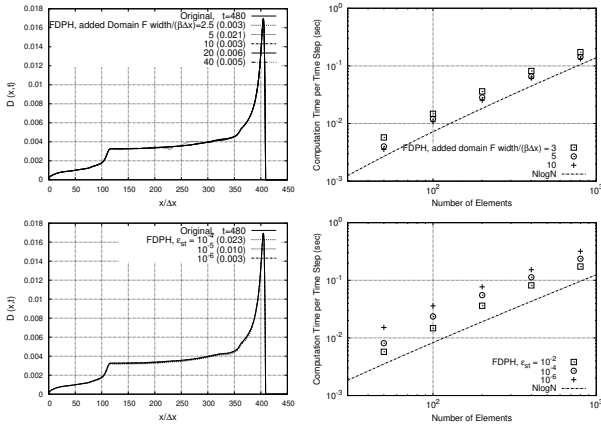


Fig. D.2 Dependence of the error and cost on the width of Domain F and ϵ_{st} . FDP=H-matrices are abbreviated as FDPH in the figure. (Top left) Snapshots of slip rates D over space x at $t = 480$ changing the width of Domain F. Problem and parameter settings are the same as in Fig. 15. The value at the end of the legend of FDP=H-matrices in left panels represents the relative error from the original solution defined in §6.2. (Bottom left) Snapshots of slip rates D over space x at $t = 480$ changing ϵ_{st} . Problem and parameter settings are the same as in Fig. 15. The value at the end of the legend of FDP=H-matrices in left panels represents the relative error from the original solution defined in §6.2. (Top right) The size dependence of the computation time per time step defined in §6.2.1 changing the width of Domain F. Problem and parameter settings are the same as in Fig. 13. The $N \log N$ cost scaling is maintained even when the width of Domain F is changed. (Bottom right) The size dependence of the computation time per time step defined in §6.2.1 changing ϵ_{st} . Problem and parameter settings are the same as in Fig. 13. The cost scaling of $N \log N$ is maintained even when ϵ_{st} is changed.

(Fig. D.1, bottom right panel) to which TCA is not applied. The tuning for further accuracy improvement in admissible leaves was mere enlargement of the width of Domain F (detailed in §D.2). Note that this enlargement of Domain F does not change the cost scaling of almost $O(N)$, because the duration of Domain F is independent of N .

Additionally, Quantization is used when treating the transient term in Domain S. Quantization applied to the transient term in Domain S gives a good estimate (possibly the upper bounds) of the error caused by Quantization applied to the Domain I kernel (explained in §3.2.3) in 3D cases. This is because the magnitude of the transient term in Domain S is comparable to that of the kernel in Domain F while the Domain I kernel is much smaller than Domain F in 3D. Although Quantization does not change the cost order of the transient term in Domain S, Quantization gives the more rapid computation of the transient term in Domain S. In our implementation of FDP=H-matrices, the absolute error condition is added to the quantization condition in addition to the relative error condition using ϵ_Q as in that determining the start of Domain S in inadmissible leaves by using the same ϵ_{st} .

D.2 Δt^+ Dependence

In our implementation, the temporally second rank is adopted as shown before. Below, we investigated the dependence of the accuracy and cost on the left tuning parameter Δt^+ affecting the accuracy of the spatiotemporal separation of the kernel.

Fig. D.2 (top left) showed the results where the accuracy was better when we add a relatively large value of $10\beta\Delta x$ (or as small as $\beta\Delta x$) to

Δt^+ . In this figure, the error was suppressed below 1% except for the case of adding $5\beta\Delta x$ to Δt^+ .

The error variation related to Δt^+ is caused by the approximation of the variable separation in Domain S and that of the normalized waveform. However, the approximated normalized waveform convolution error (Eq. (24)) seemed almost negligible in this case, since the observed error did not follow Eq. (24) proportional to the temporal definition range width of Domain F. This suggested that most errors were caused by the variable separation of the Domain S kernel. Consistently, we observed that the accuracy improved as the width increases when the adding width was of $5\beta\Delta x \sim 10\beta\Delta x$, although the opposite sense tended to be shown when the additional width Δt^+ is smaller than $5\beta\Delta x$, maybe due to the functional form of the kernel.

As examined in the computation cost, measured by the computation time per time step, the $O(N \log N / N_s)$ scaling of the cost was maintained when Δt^+ increased (Fig. D.2, top right panel). The influence of Δt^+ change appeared in a proportionality coefficient between the computation cost and the number of elements. The cost in the case adding $3\Delta x/\beta$ to Δt^+ is reduced to about half when adding $10\Delta x/\beta$ to Δt^+ .

As in Fig. D.2 (top right), we can rapidly compute the convolution in the time domain immediately after (original) Domain F by broadening the time range of Domain F, where the sampling intervals of Quantization (that vary according to the change rate in the kernel) are of Δt . This is because the computation to evolve \hat{D} (defined in §A.1) is two times slower than temporally convolving the kernel in the direct way only if the sampling interval is the smallest Δt . Consistently, the cost reduction slowed as Domain F became wider and the sampling intervals of the Quantization became wider, due to the decrease of the change rate in the kernel. Indeed, when Δt^+ was of $100 \Delta t$ or larger (excessive large values yet possibly required in the case of the temporally first rank, not plotted), the cost tended to increase as Δt^+ increase.

D.3 ϵ_{st} Dependence

In 2D problems, the replacement of the kernel to the static term (called the static approximation) is often used for the kernel after the (substantial) completion of the S-wave passage. This is for reducing the rounding error arisen from the numerical evaluation of the kernel [28]. The static approximation is also used in Domain S of FDPH in 2D problems [1]. Below, we investigated the dependence of the solution accuracy and cost on the static approximation in FDP=H-matrices by changing the absolute error condition ϵ_{st} determining the start of the Domain S in inadmissible leaves; note that ϵ_{st} is also used to the error criteria to quantize the transient term in Domain S. To appropriately evaluate the computation costs, we imposed a related acceleration technique of computing the transient term in Domain S (explained in §B.3).

The solution accuracy was found to be affected by ϵ_{st} predominantly even if the magnitude of ϵ_{st} was as small as 10^{-4} (Fig. D.2, bottom left panel). When ϵ_{st} was changed from 10^{-4} to 10^{-6} , the relative error roughly increased in proportion to the logarithm of ϵ_{st} . Slip rates tended to decrease almost everywhere due to the static approximation. It suggested that the static approximation works as a kind of damping. Such a behavior was also observed in the accuracy evaluation of Quantization alone (studied in §A.2).

The computation time per time step showed a quite small dependence on ϵ_{st} (Fig. D.2, bottom right panel). The cost was roughly inversely proportional to ϵ_{st} . Even if ϵ_{st} was changed by about 4 digits, the computation speed changed only about 3 times, and the effect of ϵ_{st} to the cost was small. This is natural because the absolute error condition is negligible in the situation where the source-receiver distance becomes sufficiently large as in admissible leaves. Since the $N \log N$ cost is made by the cost of admissible leaves, this means that the effect of ϵ_{st} on the $O(N \log N)$ factor is small.

The absolute error bound ϵ_{st} dominantly controled the accuracy while it does not change the cost largely. This tendency will be inherited to the FDP=H-matrices in 3D problems applying Quantization to Domain I.

E Derivation of Some Relations in the Paper

E.1 Degenerating Normalized Waveform

Here we show that the approximation error of the degenerating normalized waveform is proportional to $(1 + \eta^{-1})^{-1}$ in the convolution, Eq. (24).

The normalized waveform is the discretized kernel divided by its time integral over Domain F. The time dependence of the normalized waveform is thus expressed by the property of the un-discretized kernel and the effect of the discretization. By considering this, the error of the normalized waveform is found to be related to discretization, attenuation, and radiation pattern, since the original kernel represents the impulsive wave well characterized by the attenuation and radiation pattern. Concerning the radiation pattern of the kernel, the projection of the stress to the traction can contribute the error of using the degenerating normalized waveform (but it can be avoided, as shown below). Those three effects (the discretization, attenuation, and (the original) radiation pattern) are separately investigated below.

First, since the travel time for a receiver and each minute subelement contained in a source element is not that for the collocation points of source and receiver, the finite duration of the normalized waveform arises. This makes a radiation pattern (not original) caused by the spatial discretization of the elements, which can make the error of $O(1/(1 + 1/\eta))$ when using the degenerating normalized waveform. The error caused by this spatial discretization is estimated by using a 2D situation where the direction the fault j lies forms an acute angle θ_{ij} with the vector connecting the receiver i and the center of the source element j . We here set the wave speed unity, and focus on the distance of subelement to a receiver. In this situation, the distance $\tilde{r}_{ij}(d)$ between the receiver and a subelement approaching the receiver along the fault by d , is shown to be $\tilde{r}_{ij}(d) = \tilde{r}_{ij}(0) + d \times \cos \theta_{i,j} + O(1/(1 + 1/\eta)\Delta x)$, by using $\theta_{ij} = \theta_{i,j} + O(1/(1 + 1/\eta))$. It shows that the i -dependence of h_{ij} is of $O(1/(1 + 1/\eta)\Delta x)$, because the distribution $\tilde{r}_{ij}(\Delta) - \tilde{r}_{ij}(0)$ is exactly the shape of h_{ij} as long as we neglect the geometrical spreading. The error caused by the discretization is evaluated as above based on the smallness of the variation in θ_{ij} . This order estimate is also valid in 3D cases.

Second, since the wave arrival time is different in each subelement in one source element, the stress response of Domain F contains both the interactions purely caused by the wave and other contributions from the static term or near-field term [2]. Those have different degrees of the attenuation and radiation patterns [26], so that the magnitude relation in these terms can vary, depending on the locations of the source and receiver. The change in such a magnitude relation is on the order of relative changes in the angle and distance between a source and receiver, being of $O(1/(1 + 1/\eta))$ in a cluster, since the kernel is the function of the distance and the angle between the source and receiver. Indeed, while the travel time is exactly separated in 2D planar faults, normalized waveforms had errors even in 2D planar faults (Fig. 16).

Third, in this paper, as referred in §2.1, the stress is computed by FDP=H-matrices and the projection of the stress onto the traction does not include any approximation. We emphasize that this approach is different from merely approximating the normalized waveform of the kernel connecting the traction and slip rate. If a normalized waveform is defined for the kernel connecting the traction and slip rate, further error will arise. This is because the magnitude relation of the terms comprising the kernel is different in each component of the stress tensor. The caused error depends on the direction corresponding to the component

of the traction, and the error is no more of $O(1/(1 + 1/\eta))$, so that the error order of the normalized waveform becomes of $O(\partial_t D_j(\Delta t_j^- + \Delta t_j^+))$ in Eq. (24). Although the implementation is obviously easier when ignoring the component dependency of the normalized waveform, in this paper, in order to avoid such errors concerning the projection, we have defined the normalized waveform of each source to each stress component in the real coordinates. The error of the degenerating normalized waveform for the traction will be examined in other places.

E.2 Scale Analysis to Obtain the Cost Scaling of FDP=H-matrices

We here show a scale analysis to obtain the typical N dependence of the costs in FDP=H-matrices shown in Fig. 9 (bottom right). It is rather obvious that the cost of the constant η scheme is of $O(N \log N)$ by compared with the standard cost of H-matrices in spatial BIEM, which is of $O(N \log N)$ [19]; the reason is briefly considered in the text related to Fig. 9. Hence, we focus on the rather nontrivial cost scaling of the constant $\eta^2 dist$ scheme below. We here normalize the length scale by Δx_j and assume Δx_j is on the order of a constant Δx for any element number j .

First we introduce the standpoint of the following analysis. As shown in Fig. 9 (bottom right), most of the components of the kernel were covered by the largest (and the second largest) block clusters. This suggests that the costs are dominated by the large block clusters. Then we estimate the typical costs of the constant $\eta^2 dist$ scheme by assuming this numerically observation that the almost all the matrix components (and thus also the corresponding spatial regions) are covered by the largest-class block clusters.

Let us next estimate the number of leaves at the smallest level. Those leaves have the largest sides, which is of $O(L/\eta)$, independent of the dimension of the fault. In the constant $\eta^2 dist$ scheme, this length corresponds to $O(L/\eta) = O(\sqrt{L})$. Therefore, to occupy all the spatial regions by such largest clusters as assumed, the number of the largest-class block clusters are required to be of $O(L^{2D_b}/\sqrt{L}^{2D_b}) = O(L^{D_b}) = O(N)$.

Based on the above estimate of the number of the largest block clusters being of $O(N)$, we finally obtain the typical cost estimates of constant $\eta^2 dist$ scheme. Since the values of $N_f + N_r$ in the largest clusters are of $O(diam^{D_b}) = O((L/\eta)^{D_b}) = O(L^{D_b/2}) = O(N^{1/2})$, the spatial costs $\sum(N_f + N_r)$ (the sum of the number of elements in block clusters) are of $O(N) \times O(N^{1/2}) = O(N^{3/2})$. On the other hand, since the values of $dist$ are of $O(L)$ in the largest block clusters, the temporal costs $\sum dist (= O(\sum \bar{r}))$ (the sum of time integration length) are of $O(N) \times O(L) = O(NL)$. These estimates of the spatiotemporal costs successfully capture the leading orders of the typical costs in the constant $\eta^2 dist$ scheme, shown in Fig. 9 (bottom right).

E.3 Detail of Domain Partitioning after ART

E.3.1 Discretization Procedure

We here detail the discretization of the right hand side in Eq. (20), described in §4.3. The approximation of \hat{K} is not discussed below. After the approximations of ART are used, the following integral equation to evaluate the stress response of Domain F is discretized;

$$T_i^F(t) = \sum_j \int_{-\Delta t_j^-}^{\Delta t_j^+} d\tau' K_{i,j}(t_{ij} + \tau') D(t - t_{ij} - \tau') \quad (E.1)$$

$$= \sum_j \hat{K}_{ij}^F \int_{-\Delta t_j^-}^{\Delta t_j^+} d\tau' h_{i,j}(\tau') D(t - t_{ij} - \tau') \quad (E.2)$$

With ART, this becomes

$$T_i^F(t + \delta t_i) = \sum_j \hat{K}_{i,j} \int_{-\Delta t_j^-}^{\Delta t_j^+} d\tau' h_j^F(\tau') D(t - \bar{t}_j - \tau') \quad (\text{E.3})$$

as shown in §4.2.

The integral is discretized by the piecewise-constant slip rate

$$D_j(\tau) = \sum_m D_{j,n-m} [H(\tau - (n-m)\Delta t) - H(\tau - (n-m+1)\Delta t)] \quad (\text{E.4})$$

$$= \sum_m D_{j,n-m} [H((n-m+1)\Delta t - \tau) - H((n-m)\Delta t - \tau)] \quad (\text{E.5})$$

where $H(x) = 1 - H(-x)$ is used. The stress is collocated by using the time $t = (n+1)\Delta t(-0)$ (in Eq. (20)) for each time step n . After such D_j and t are substituted, the above integral equation becomes

$$T_i^F(t + \delta t_i) \quad (\text{E.6})$$

$$= \sum_{j,m} \hat{K}_{i,j}^F D_{j,n-m} \int_{-\Delta t_j^-}^{\Delta t_j^+} d\tau' h_j^F(\tau') [H(\tau' + \bar{t}_j - m\Delta t) - H(\tau' + \bar{t}_j - (m+1)\Delta t)] \quad (\text{E.7})$$

$$= \sum_{j,m} \hat{K}_{i,j}^F D_{j,n-m} [H(\bar{t}_j - \Delta t_j^- - m\Delta t) - H(\bar{t}_j + \Delta t_j^- - (m+1)\Delta t)] \int_{-\Delta t_j^-}^{\Delta t_j^+} d\tau' h_j^F(\tau') [H(\tau' + \bar{t}_j - m\Delta t) - H(\tau' + \bar{t}_j - (m+1)\Delta t)] \quad (\text{E.8})$$

$$= \sum_{j,m} \hat{K}_{i,j}^F D_{j,n-m} [H(\bar{t}_j^- - m\Delta t) - H(\bar{t}_j^+ - (m+1)\Delta t)] \int_{\max(-\Delta t_j^-, m\Delta t - \bar{t}_j)}^{\min(\Delta t_j^+, (m+1)\Delta t - \bar{t}_j)} d\tau' h_j^F(\tau'), \quad (\text{E.9})$$

where $\bar{t}_j^\pm := \bar{t}_j \pm \Delta t_j \pm$ is defined at the last line.

$[H(\bar{t}_j^- - m\Delta t(+0)) - H(\bar{t}_j^+ - (m+1)\Delta t(+0))]$ is nonzero only for $(\bar{t}_j^- \leq m\Delta t) \cap (\bar{t}_j^+ > m\Delta t)$. Such a range of m becomes $\lceil \bar{t}_j^- / \Delta t \rceil \leq m < \lceil \bar{t}_j^+ / \Delta t \rceil$. Note that when \bar{t}_j^\pm is near integer numbers, the rounding of the decimals can be numerically erroneous due to the rounding errors of \bar{t}_j^\pm ; to treat that, it is useful to change the minimum of Δt_j^\pm from $\Delta x_j / (2c)$ to $\Delta x_j / (2c) + C_s^F \Delta t$ with some safe coefficients $0 < C_s^F < 1$; C_s^F is set at 1 in the numerical experiments of this paper.

Then defining $\bar{m}_j^- := \lceil \bar{t}_j^- / \Delta t \rceil$ and $\Delta m_j := \lceil \bar{t}_j^+ / \Delta t \rceil - \bar{m}_j^-$, we finally reduce the integral equation to evaluate the stress response of Domain F to

$$T_i^F(t + \delta t_i) \quad (\text{E.10})$$

$$= \sum_j \hat{K}_{i,j}^F \sum_{m=\bar{m}_j^-}^{\bar{m}_j^- + \Delta m_j - 1} D_{j,n-m} \int_{\max(-\Delta t_j^-, m\Delta t - \bar{t}_j)}^{\min(\Delta t_j^+, (m+1)\Delta t - \bar{t}_j)} d\tau' h_j^F(\tau') \quad (\text{E.11})$$

$$= \sum_j \hat{K}_{i,j}^F \sum_{m=0}^{\Delta m_j - 1} D_{j,n-m-\bar{m}_j^-} \int_{\max(-\Delta t_j^-, (m+\bar{m}_j^-)\Delta t - \bar{t}_j)}^{\min(\Delta t_j^+, (m+\bar{m}_j^-+1)\Delta t - \bar{t}_j)} d\tau' h_j^F(\tau') \quad (\text{E.12})$$

$$= \sum_j \hat{K}_{i,j}^F \sum_{m=0}^{\Delta m_j - 1} h_{j,m}^F D_{j,n-m-\bar{m}_j^-} \quad (\text{E.13})$$

with

$$h_{j,m}^F = \int_{\max(-\Delta t_j^-, (m+\bar{m}_j^-)\Delta t - \bar{t}_j)}^{\min(\Delta t_j^+, (m+\bar{m}_j^-+1)\Delta t - \bar{t}_j)} d\tau' h_j^F(\tau') \quad (\text{E.14})$$

$$= \frac{1}{\hat{K}_{i,j}^F} \int_{\max(-\Delta t_j^-, (m+\bar{m}_j^-)\Delta t - \bar{t}_j)}^{\min(\Delta t_j^+, (m+\bar{m}_j^-+1)\Delta t - \bar{t}_j)} d\tau' K_{i,j}(\tau' + t_{i,j}) \quad (\text{E.15})$$

$$= \frac{1}{\hat{K}_{i,j}^F} \int_{\max(t_{i,j}^-, (m+\bar{m}_j^-)\Delta t + (t_{i,j} - \bar{t}_j))}^{\min(t_{i,j}^+, (m+\bar{m}_j^-+1)\Delta t + (t_{i,j} - \bar{t}_j))} d\tau K_{i,j}(\tau) \quad (\text{E.16})$$

E.3.2 Simplification of Time Integrals over Respective Domains

Further using the arbitrariness of $\Delta \bar{t}_j^\pm$, the integral region of the normalized waveform (Eq.(30)) can be simplified when $\bar{t}_j = t_{i,j}$ as set in Eq. (23). In the numerical experiments of the anti-plane problem treated in this paper, we set $\Delta \bar{t}_j^\pm$ as a minimum $\Delta \bar{t}_j^\pm \geq \Delta x / (2c)$ that satisfies $\Delta \bar{t}_j^- = \bar{m}_j^- \Delta t - \bar{t}_j$ and $\Delta \bar{t}_j^+ = (\bar{m}_j^- + \Delta m_j) \Delta t - \bar{t}_j$. These relations can be rewritten as

$$0 = \bar{t}_j - \Delta \bar{t}_j^+ - \lfloor (\bar{t}_j + \Delta \bar{t}_j^+) / \Delta t \rfloor \Delta t \quad (\text{E.17})$$

$$0 = \bar{t}_j - \Delta \bar{t}_j^- - \lceil (\bar{t}_j + \Delta \bar{t}_j^-) / \Delta t \rceil \Delta t \quad (\text{E.18})$$

When $\Delta \bar{t}_j^\pm$ (and \bar{t}_j) are chosen in such a manner, the integral range is reduced as

$$\min(t_{i,j}^+, (m + \bar{m}_j^- + 1)\Delta t + (t_{i,j} - \bar{t}_j)) \rightarrow (m + \bar{m}_j^- + 1)\Delta t \quad (\text{E.19})$$

$$\max(t_{i,j}^-, (m + \bar{m}_j^-)\Delta t + (t_{i,j} - \bar{t}_j)) \rightarrow (m + \bar{m}_j^-)\Delta t. \quad (\text{E.20})$$

Note that this use of special $\Delta \bar{t}_j^\pm$ also simplifies the integral to evaluate the stress response of the Domains I and S. For example in Domain S, the second term in the stress response of Domain S (Eq. (B.4)) becomes exactly zero as long as $(\bar{m}_j^{\beta+} \Delta t - \bar{t}_j^{\beta+}) = 0$ is satisfied.

E.4 Derivation of Eq. (44)

Here we derive a formula to compute \bar{T}' with G (Eq. (44)). An essential point to derive this relation is that the original reference stress (defined by Eq. (36)) is invariant to the time step evolution. This is represented by the following equation:

$$\bar{\mathbf{T}}_{n+1} - \mathcal{M} \bar{\mathbf{T}}_n = \mathbf{0}. \quad (\text{E.21})$$

When it is noticed, the relation, Eq. (44), is readily found by the similar difference of \bar{T}' .

Eq. (44) is obtained by the following procedure;

$$(\bar{\mathbf{T}}'_{n+1} - \mathcal{M} \bar{\mathbf{T}}'_n)_m = \bar{T}'_{n+1,m} - \bar{T}'_{n,m-1} \quad (\text{E.22})$$

$$= \sum_{j|m+\bar{m}_j^- > 0} g_j \hat{D}_{j,n+1-\bar{m}_j^- - m} - \sum_{j|(m-1)+\bar{m}_j^- > 0} g_j \hat{D}_{j,n-\bar{m}_j^- - (m-1)} \quad (\text{E.23})$$

$$= \sum_{j|m+\bar{m}_j^- = 1} g_j \hat{D}_{j,n+1-\bar{m}_j^- - m} \quad (\text{E.24})$$

$$= \sum_j \delta_{-m+1, \bar{m}_j^-} g_j \hat{D}_{j,n} \quad (\text{E.25})$$

$$= (\mathcal{M} \mathbf{G} \hat{\mathbf{D}}_n)_m. \quad (\text{E.26})$$

When transforming the fourth line to the fifth line, we used a relation, $(\mathcal{M} \mathbf{G})_{mj} = \delta_{-m+1, \bar{m}_j^-} g_j$.